CHAPTER I

FROM PARTICLES TO PATTERNS: THE BIOMIMETIC SYNTHEIS OF NANOMATERIALS

Introduction

For decades, researchers have been searching for alternative methods to ameliorate the rate of waste production and the cost of spending commonly associated with nanofabrication facilities across the world. Estimated to reach an outstanding $100 billion per facility by the year 2020, the mounting cost associated with supporting technicians and maintaining instrumentation, alone, has motivated researchers to develop alternative approaches, utilizing less expensive, water soluble biological materials, or biomaterials, for new types of devices. From manual stamping to computer-based printing, the availability of current materials processing techniques has offered unique approaches for immobilizing biomaterials that not only elucidate unique interfacial interactions inherent in 2D systems, but also aid in developing strategies to disrupt them. Such approaches will lead to the development of a range novel, sustainable materials with applications ranging from memory storage to therapeutic devices.

The underlying theme of this dissertation will emphasize the application of piezoelectric inkjet printing using the Dimatix Materials inkjet Printer (DMP) as a novel materials processing technique to pattern such sustainable materials. The DMP is a non-contact and non-destructive technique for patterning biomaterials ranging from DNA conjugated carbon nanotubes to proteins and polymers. In the following chapters, inkjet

technology will be discussed in the context of materials processing. In this chapter, a brief overview of biomaterials deposition will be discussed in the context of biomineralization and bio-inspired research.

Biomineralization

In its most basic form, a material synthesized on the nanoscale infers a smaller, more reactive particle. To exercise control over the design and presentation of a particle in this size regime, researchers have manufactured a number of nanostructured materials, or *nanomaterials*, with tightly controlled reaction environments. Traditionally, synthetic approaches for the production of nanomaterials have involved high-temperature reaction environments with energy intensive techniques such as laser ablation, ion implantation, chemical vapor deposition (CVD), photolithography, or thermal decomposition.[1] Incorporating rapid prototyping techniques, such as these, has provided a foundation for designing sustainable materials that was essential for the commercial development of current minimum-feature sized semiconducting integrated circuits. However, the production of these devices has come at a major price. Among other challenges currently faced by high-throughput nanofabrication laboratories, the high cost of laborers and instruments, high temperature reaction conditions, and a surplus in generated waste are primary disadvantages.[1] As previously mentioned, the cost of fabrication facilities are estimated to reach an close to $100 billion dollars per facility by the year 2020, as the demand for smaller, lighter, and faster materials continues to grow.[1] Moreover, because most nanoscale deposition techniques are top-down approaches, breaking down large precursor molecules to yield an active film, the amount of waste and chemical derivatives

associated with nanomaterial formation is growing. [2] For this reason, researchers have been searching for alternative methods to passivate the rate of waste production and the cost of spending in the semiconductor industry.

The most accessible resource for the synthesis of functional nanomaterials under ambient conditions is found in biology. From highly ordered nanostructures to genetically controlled reactive surfaces, systems in biology perpetually demonstrate their ability to find effective solutions to multifaceted, real world problems using a rigorous process of natural selection.[3-7] The versatility of biology's incredible portfolio encourages researchers to develop modified syntheses derived from nature, and their findings have been successfully organized into the field of *biomimetics*, or bio-inspired research, which encompasses alternative approaches towards developing nanomaterials with technologically relevant applications.[8] Based primarily on the designs, mechanisms, and processes found in nature, biomimetics encompasses the field of structural biology while interfacing engineering, materials science, physics, and chemistry.[4, 8]

Biomimetics infers manipulating and mimicking the natural architectures and processes of biologically produced minerals, or *biominerals,* to direct the synthesis of non-natural materials. For instance, the architecture of one of the most abundant biological species on the planet, the virus, has recently been manipulated to serve as molecular containers for the synthesis of a variety of functional bio-compatible cargoes.[9, 10] One virus in particular, the cowpea chlorotic mottle virus (CCMV), has been used as a container where its positively charged interior serves as a site for the nucleation of spatially confined metal oxide nanomaterials.[10] From a different perspective and a much larger scale, versatile strategies for substrate modification have been developed directly,

using the bio-inspired surface mediated mineralization of biological organisms.[3] The eggshell matrix proteins were isolated from the Chinese soft-shelled turtle (composed primarily of aragonite, $CaCO_3$) were isolated.[3] It was suggested that these matrix proteins contained pelovaterin peptides as their major unit. On the surface of the eggshell, these peptides self-assembled into micelles, altering the interfacial energy of the eggshell—an adaption that has proven necessary embryonic survival.[11] Applications of such controlled mineralization have been applied to the successful construction of functional two-dimensional (2D) reactive surfaces, with reduced nonspecific adsorption.[12-15]

Metal Oxides in Nature

There has been as many as 60 biominerals that have been identified as indispensable components for the proper function of organisms, and more than 60% of them are reported to be coordinated to either hydroxyl moieties or water molecules, enabling the rapid release of ions in solution.[7] In an oxidative environment, such as the atmosphere of the Earth, oxides are the lowest free energy states for most minerals in the periodic table.[16] As insulators, SiO_2 and Al_2O_3 are the two most commonly used supports for catalysis, as they are non reducible oxides.[16] Alternatively, semiconductors, such as ZnO and SnO_2, have high electrical resistivities that have been adapted to active materials, such as gas sensors of fuel cells.[16]

Through precisely tuned processes, Nature is able to synthesize a variety of metal oxide nanomaterials under ambient conditions. The magnetic navigation device found in magnetotactic bacteria (MTB) is one such example.[17] Magnetite (Fe_3O_4) nanocrystals are aligned with the Earth's geomagnetic field and are contained within specific organelles

known as magnetosomes.[17] Fresh water salmon, for example, utilize these magnetic nanoparticles in the nasal cavities of their forehead as a biomagnetic compass during migration.[18] Surprisingly, the properties associated with metal oxides in technology are not so far removed from what is observed in natural systems.

Components of Biomineralization

Nature dictates the basic structure and function of metal oxides in biology by a set of genetically controlled rules. From the supramolecular to the cellular level, assemblies of lipids, glycoproteins, or nucleotides in nature are necessary determinants, defining specific reaction sites along organelles, membranes, or cell walls.[19] Understanding the basic theory, process, and components behind the biomineralization of metal oxides is the first step in developing functional biomimetic materials. For example, organic ligands in the form of an amino acid side chain, lipids, or carbohydrates, which are all found in biological systems, direct the assembly of highly structured metal oxide nanomaterials.[20] Most metals in nature follow similar trends as laid out by the hard-soft acid-base (HSAB) theory.[19] Free metal ions act as Lewis acids in the hydrolysis of a precursor before they completely bind to a donor ligand (Lewis base).[19] For instance, the charge associated with the Lewis acid metal may facilitate an energetically favorable nucleophilic attack on a specific carbonyl of a ligand. Because of the effective charge of the metal-ligand coordination, there are two alternative ways that this attack can occur. *Soft* metals (Pt^{2+}, Au^{2+}, Cu^{2+}, Cd^{2+}) that are large and polarizable with low oxidation states bind with *soft* ligands (carbonyls, CN^-,RS^-) in order to balance their charge.[19] However, h*ard* metals (first row transition metals), are smaller and less polarizable and are balanced by

accepting lone pair electrons associated with *hard* ligands, such as H_2O, amines, phosphates, or alcohols.[19] The ligand donor type can affect the redox potential of the coordinated metal, its stereochemistry, and its subsequent reactivity within a biological system.

With that in mind, there are several examples in Nature where ligands are used to create metal oxide structures. In order to identify the components that adhere specifically to metal surfaces, researchers have developed methods to screen libraries of up to 10^7 protein or peptide sequences responsible for inducing specific metal oxide mineralization.[21, 22] Once the sequence is selected, optimal peptide or non-peptide based mimics can be synthesized and subsequently applied to a wide range of nanomaterial syntheses. Of the techniques developed to isolate specific metal bound peptides or proteins, phage display (PD) and cell surface display (CSD) are the most widely used.[20, 21] Combinatorial PD is used to specify the selectivity of the peptide-substrate interaction. In this method, a phage is created on an ensemble of bacterial particles, each displaying different combinations of amino acids that are fused to the surface protein of the metal particle.[23] Peptides bound specifically to the crystal surface are then eluted from the surface, amplified using the polymerase chain reaction (PCR), and re-reacted up to five separate times.[20] After the fourth and fifth cycles, the resultant phage is sequenced, and the peptide responsible for binding to the surface of the crystal is identified.[20]

An alternative approach to identifying surface ligands is CSD. The process of CSD involves an analytical approach for the quantification of binding constants and dissociation rates *in situ* of up to 10^4 protein molecules per cell.[24] CSD isolates proteins that display ligand-binding, catalytic, or electrochemical properties. Protein libraries on a

specific cell surface can be labeled with a soluble ligand and quantitively screened for reactivity using flow cytometry.[24] Although, the identification of biomolecules specific for a metal is crucial in developing a particular biomimetic synthesis, it must be understood that peptides and proteins, alone, are not responsible for metal oxide formation in biology. In fact, the properties of these biomolecules *in situ* are a direct result of their reaction environment.[25]

Biomineralization Optimization

As previously mentioned, the strategies and precursors incorporated by natural systems cannot be directly applied to engineered materials. For this reason, specific reaction conditions (length of reaction time, pH) are often tailored to a system, depending on the desired structure and reactivity of the material; typically, a bio-inspired synthesis often requires a developed precursor, in the form of a metal salt, suspended or dissolved in an aqueous media, and coordinated to a structure directing agent. Both natural (peptides, starches, proteins) and synthetic polymers (dendrimers, block copolymers) can be used as structure directing agents in inducing the biomineralization of metal oxides.[6] They assemble in an ionic solution to direct the size, shape, and mean distribution of the resultant product.

Incorporating alternate templates has been shown to affect the morphology of a synthesized material. In one study, a modified macromolecular template was anchored onto the surface of a polystyrene latex bead, to direct the control and morphology of ZnO nanomaterials (Figure 1).

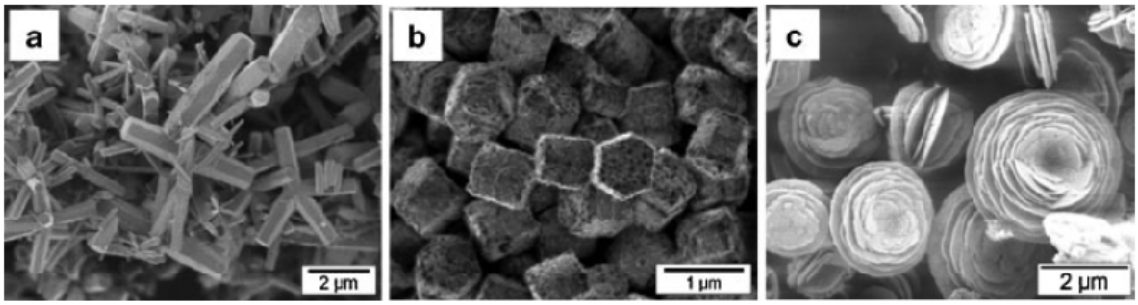

Figure 1. Zinc oxide materials synthesized with varying templates. (A) in the absence of latex beads, (B) in the presence latex beads functionalized with 9 g L^{-1} of poly(styrene-acrylic acid), and (C) latex beads (removed by calcinations at 600ºC) functionalized with 3 g L^{-1} poly(styrene-maleic acid). Latex beads can be easily synthesized using mini-emulsion polymerization, and their functional surfaces can be tuned for specific ZnO properties.[6]

In this experiment, diblock copolymers of ethylene oxide (EO), methacrylic (MAA), and double hydrophilic graft copolymers (PMAA or poly(vinyl sulfonate) backbones) were initially used without the latex beads to synthesize ZnO nanoparticles. After the synthesized particles were characterized, the electrostatic charge associated with copolymers of vinyl-sulfonate demonstrated a more active range of control over the subsequent structures, producing rod-like ZnO morphologies (Figure 1a).[6] To captilize on this activity, vinyl-sulfonate was then anchored onto a hierarchal, supramolecular network of latex beads, demonstrating an alternative approach to control the synthesis of ZnO. As the figure elucidates, ZnO precipitated in the presence of the beads, yielding pseudo-cubic morphology (Figure 1b).[6] After moderate annealing (600°C), the latex beads were removed, altering the structure, yet again (Figure 1c).

Alternating the templating agent will not only affect the product's morphology but will also impact its activity. The impact on the specific size of the material can determine the magnetic, electronic, and chemical properties of nanoparticles.[26, 27] Such size

dependency has been observed in γ-Fe_2O_3 nanoparticles. A 55 nm γ- Fe_2O_3 nanoparticle exhibits ferromagnetic behavior while a 12 nm particle produces superparamagnetic behavior, with no hysteresis.[18] The chemical reactivity of the smaller nanoparticle is enhanced due to its larger surface area per unit mass. The decreased particle size decreases the overall magnetic anisotropy of the particle, inducing the change to superparamagnetic.[28] Novel methods of creating metal oxide nanoparticles with a defined size are necessary for achieving not only desired magnetic properties, but also electronic, and chemical properties.

Bio-Inspired Research

Bio-inspired research is based on identifying and emulating the principles of biology instead of copying them directly. Because most strategies incorporated by natural systems cannot be directly applied to engineered materials, the need for alternative synthetic routes are necessary for the biomimetic synthesis of non-natural elements, such as barium, nickel, copper, or aluminum, with functional properties on the nanoscale.[1, 8] From a materials perspective, highly intact biological structures such as diatoms, bacteria, proteins, or butterfly wings provide an excellent source of inspiration for their synthesis. In the following section, a variety of mediated nanomaterial syntheses, their response to variable parameters, and their ability to have functionalized controlled stability over time will be discussed.

Generally, a biomineral can be induced, controlled, or mediated by its reaction environment.[3] Induced syntheses are most common in single-celled organisms, such as fungi or bacteria, and typically occur within a charged, open environment. The

mineralized product remains dynamic and typically does not have a specific function within the system.[19,7,18] Biologically controlled, or constrained, reactions yield minerals with a minimal size distribution that are localized to a confined area, defined by a cell wall, lipid bilayer, or vesicle.[7] The mineralized product has functional properties that are dependent on its origin of synthesis (extra-, inter-, or intracellularly).[3, 19] On the other hand, biologically mediated mineralization is often genetically controlled by the organism within unconstrained, open environments. Templates, such as peptides, proteins, nucleic acids, or polymers, can be incorporated during the synthesis.[3] For instance, the proteins in diatoms, radiolarian, and sponges produce SiO_2 that serve as their exoskeleton in the ocean, and biopolymers associated with echinoderms and nacreous layers mediate the production of single calcite crystals that serve as their protective coating.[29, 30] The valuable properties associated with constrained or unconstrained metal oxide synthesis in specific biological systems has inspired the development of functionalized nanomaterials and will be discussed in the following sections.

Constrained Biomineralization

Synthetic control over the physical and chemical properties of a nanoparticle can be tuned according to its biological micro- or nano-environment. Some of the most notable platforms that have been adapted for the controlled synthesis of metal oxide nanomaterials include the apoprotein ferritin, viral capsids, or bacterial cages; alternative biotemplates, such as self assembled peptide nanorings or porous butterfly wings have similarly been tailored as unique platforms yielding interesting structures. Regardless of

the platform used, these molecular architectures offer constrained micro- or nano-environments that yield a narrow size distribution of nanoparticles under ambient conditions and will be discussed in the context of viable alternatives for the synthesis of functional nanomaterials.

Bacterial Synthesis of Metal Oxide Nanomaterials

At least one-third of the elements in the periodic table have experienced changes in valence states induced by microbial activity. While some metals (iron, calcium, and potassium) serve as an essential source for nutrients in bacterial systems, others are introduced as contaminants (lead, nickel, cobalt, and cadmium).[2] This co-habitation with such heavy metal pollutants has forced organisms among marine bacteria to develop a high metal tolerance, making them an interesting source for templating the constrained synthesis of metal/metal oxide nanoparticles.

Magnetic metal oxides nanoparticles have aroused particular interest because their properties can be tuned according to their size and shape. Exchange coupling at the interface of ferri/ferromagnetic and antiferromagnetic phases of nanoscale materials can be applied as high density magnetic storage devices or components for enhanced sensor development. Current wet-chemistry approaches, demonstrating control over the magnetic exchange bias of a nanoparticle, require expensive organometallic precursors and high temperature reaction conditions. Alternatively, biologically produced microbes reduce metal ions in aqueous media to form stable suspensions of nanoparticles coated with biomolecules (proteins, peptides). This coating not only activates modified

properties of the nanoparticle, but it also prevents particle agglomeration by stimulating the growth of discrete nanoparticles within a solution.

Synthesis of protein-functionalized ferromagnetic Co_3O_4 nanocrystals

One particular marine bacterium culture (obtained from the Arabian seacoast) has been used as the host system for the constrained synthesis of cobalt oxide (Co_3O_4).[2] Bulk Co_3O_4 has been synthesized at room temperature within the bacterium, producing a cubic spinel, antiferromagnetic phase. On the nanoscale, however, Co_3O_4 adapts an overall ferromagnetic type behavior because the uncompensated spins at the nanoparticle surface become a large fraction of the total number of spins. In this synthesis, the precursor, cobalt acetate (Co^{2+}) was incubated with the bacteria in an aqueous solution, where the as-synthesized particles displayed average diameters of 6 nm. After mild calcination (200ºC for 2h), the particles grew larger (50 nm), inferring that its protein passivating layer had degraded, causing particle aggregation. Upon further investigation, bacterial strains were isolated from the surface of the bacterium; of the 15 identified strains, only one gave a visible indication of the formation of nanoparticles *in vitro*. Phylogenetic sequencing revealed that the isolated oligonucleotide strand could potentially be the source of hydrolysis and reduction of the precursor salt.[2]

Once the synthesis was complete, the crystalline nanostructures were characterized using X-ray diffraction (XRD). After heating above 930ºC (a reducing environment), the composite material was transformed into the CoO phase, confirming that at room temperature, Co_3O_4 is the thermodynamically preferable state.[2] Even though there was a dominant presence of Co^{3+} ions, X-ray photoelectron spectroscopy (XPS) identified trace

amounts of Co^{2+} within the Co_3O_4 composite. Of the 24 Co-ions in the Co_3O_4 unit cell, it was predicted that the 8 Co^{2+} ions were located in the tetrahedral sites and the 16 Co^{3+} ions were in the octahedral sites. This mixed valence state within the unit cell was understood as the cause of the nanoparticle's overall magnetic moment and was investigated accordingly (Figure 2).

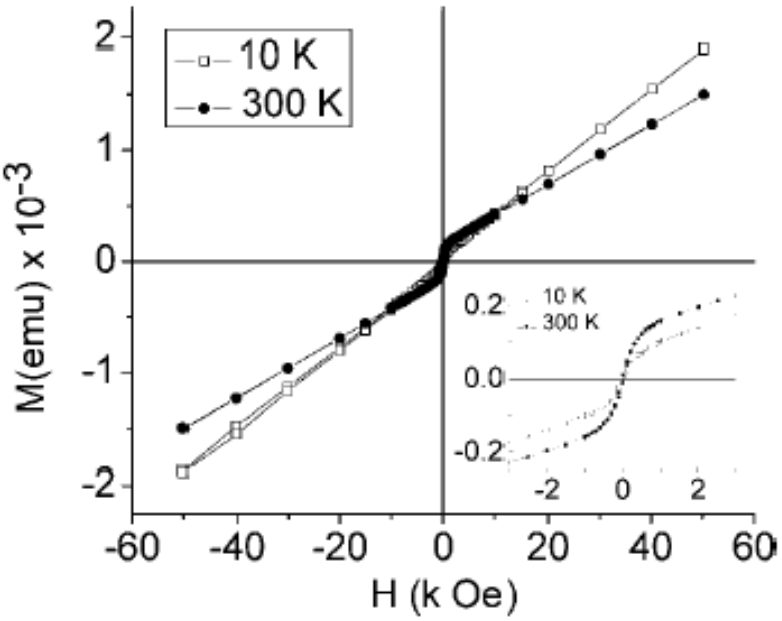

Figure 2. Magnetization versus magnetic field measurements of Co_3O_4. Results shows a nonlinear reversible behavior once calcined at 10 and 300 K. Plot did not show saturation until highest applied field (50 kOe), which is a result of nonzero net moment and ferromagnetic-type behavior of nanoparticles with Co^{3+} at octahedral sites. Inset shows view zoomed in.[2]

The mechanism behind the oxidation of the cobalt precursor and subsequent Co_3O_4 precipitation within the bacterium host (Co^{2+} to Co^{3+}) was examined. Nonspecific intake of the toxic Co ions within the host forced a spontaneous reaction that was balanced by the homeostasis of the system through developed resistance mechanisms. Through the

basics of biology, it was predicted that Co^{2+} enters and exits the cell through an efflux pump. While in the pump, Co^{2+} is predicted to either filter through a cation diffusion facilitator (CDF) or be exported by resistance nodulation cell division (RND) proteins. Either way, the bacterial capsule was understood to bind and concentrate the metal ions along its walls, forming a cooperative, self-organized colony to resist induced external stress. This possible interbacterial communication involved in oxidizing precursor ions has exposed valuable properties associated with constrained synthesis and can be applied to control the synthesis of a number of additional metal oxides.

Room Temperature synthesis of Barium Titanate

As a source for nonvolatile memory, microelectromechanical (MEMs) device, or thin-film capacitor, barium titantate (BT) is an important electroceramic material with ferroelectric properties.[31] Most reported room temperature syntheses have produced a cubic, paraelectric phased BT; however, sub-10 nm, tetragonal and ferroelectric phases are desirable for successful implementation within miniaturized devices. For this reason, a purely biological approach was used to synthesize BT nanoparticles with constrained sizes using the plant pathogenic fungus *Fusarium oxysporum* as the host system. Aqueous solutions of barium acetate ($(CH_3COO)_2Ba$) and potassium hexafluorotitante (K_2TiF_6) were reacted with *F. oxysporum*.[31] The fungal proteins were responsible for the hydrolysis and confinement of these precursor materials, inducing BT nanoparticles. The free Ba^{2+} and acetate ions released from barium acetate were understood to coordinate to the free TiF_6^{2-} ions using the extracellular proteins in the fungus. To approximate the percentage of biomaterial attached to the particle, the sample was heated to 400ºC, and

TGA determined that there was up to 50% weight loss from the starting material. TEM and XPS were used to identify the BT nanoparticles with 4 ± 1 nm size distribution, and SAED confirmed that the particles were in the tetragonal phase.

DSC and SPM were used to probe the ferroelectricity of the as-synthesized nanoparticles and at various percentages of calcinations. SPM was used to investigate the polarizability of the nanoparticles in the ferroelectric phase. The peak broadening in the maxima of the temperature-dependent dielectric response and the DSC maximum at ferroelectric transition suggested that the as-synthesized particles behave as a "ferroelectric relaxer" material. Studies indicated that BT nanoparticles could be successfully written and read on a substrate in response to an applied external electric field. Because of this confirmed reactivity coupled with the biologically constrained synthesis, the non-volatile and economically feasible synthesis of sub-10 nm BT particles is expected to revolutionize microelectronics industries.

Biomimetic synthesis of Magnetite

Iron oxides are another technologically relevant branch of metal oxides because, like cobalt oxide, they possess multi-valent oxidation states that can be tuned specifically for an application, from catalytic templates in sensor development to substrates for drug delivery. Magnetite (Fe_3O_4), which is naturally found in magnetosomes of magnetotactic bacteria (MTB) or other iron reducing bacteria, is a well recognized example of controlled biomineralization.[17, 18] Once crystallized intracellularly, magnetite nanoparticles align with the earth's magnetic field to serve as a navigational compass for a number of aquatic animals.[18] Salmon, for example, utilize the magnetite located in their

head for magnetic navigation that can last up to three years over tens of thousands of kilometers.[18]

The morphology of magnetite varies according to the different bacterial strains associated with lipid membrane of the magnetsome. The biochemical composition of the subsequent metal oxide is defined by the membrane of the magnetosome. A number of successful biomimetic approaches aimed to modify the biological synthesis of magnetite have been developed incorporating constrained biological environments. These mimics can be tuned by chemical or genetic modification to yield interesting properties that are technological significant.

The defined architecture of the metalloprotein ferritin, a natural complex of iron oxide, is found in almost all domains of life and has been used as a constrained reaction vessel for the synthesis of a number of non-natural metal oxides.[28, 32] The protein ferritin consists of 24 subunits that self-assemble into a cage, consisting of a three-fold hydrophilic channel coordinated to a four-fold hydrophobic channel.[19, 28] In biology, Fe (II) is introduced into the core of the apoprotien through its hydrophilic channels. Once inside the channels, the ferrous ion is catalytically oxidized to a less soluble ferric ion, Fe (III).[19] The ferric ion then undergoes a series of hydrolytic polymerizations to form the insoluble ferric oxyhydroxide mineral (ferrihydrite), which is physically constrained by the size of the protein cage (12 nm o.d., 8 nm i.d.).[33] The enzyme ferrous oxidase is coordinated within the protein cage, whose interior and exterior is electrostatically dissimilar, to produce spatially defined minerals.

Mineralization of non-natural Metal Oxides using Ferritin

The photoinduced mineralization of iron, titanium, and europium oxyhydroxide nanoparticles have been successfully synthesized using the protein cage, ferritin.[33] This photochemical reduction closely resembles the Fe (III) to Fe (II) reduction of marine siderophores with a citrate background.[33] In this synthesis, a known concentration of metal ion was loaded into a 12 mM solution of citrate and ferritin and was illuminated with a xenon arc lamp (320-750 nm) for over 2 h. The citrate solution induced an electrostatic environment that was essential for discrete nanoparticle synthesis in the reaction; without which, bulk precipitation was illuminated. After the 2h reaction time, the high oxidation state metal ions were photoreduced. In the presence of air, the lower state underwent reoxidation to the final, oxyhydroxide state. All products were characterized using DLS and were found to have similar sizes (12 ± 1 nm). Samples stained with uranyl acetate were analyzed using the TEM, and the intact protein cage was visible forming an outer diameter around the metal oxide cores (5.7 ± 1 nm).

Oxidation of the iron core in ferritin has also been used and applied for the mixed mineralization reactions of cobalt and iron. It is understood that if synthesized correctly, this composite material would have tailored magnetic properties, inducing the exchange coupling of ferro/anti-ferromagnetic properties; wherein, the exchange bias is self-manifested and defined by a unidirectional hysteresis loop. Control over the magnetic behavior of a nanoparticle could potentially lead to additional magnetic anisotropy effects for the use of magnetic storage and recording devices. Klem and coworkers have demonstrated the constrained synthesis of $Co_xFe_{3-x}O_4$ with an exchange bias by means of an enhanced magnetic response.[28]

For this synthesis, a deaerated solution of iron ($(NH_4)2Fe(SO_4)\ 6H_2O$),cobalt ($Co(NO_3)_2\ 6H_2O$), and H_2O_2 were added to apoferritin in NaCl (pH=8.5, 65ºC under nitrogen). The resultant solution proceeded until a homogenous dark brown solution was formed. Light scattering measurements showed no increase in the average diameter of ferritin after metal encapsulation. TEM images identified the core sizes to be consistent with the inner diameter of the ferritin (6.8-7.4 nm diameter). SAED indicated that with 33% Co doping, the *d*-spacings were consistent with the spinel phase of Co_3O_4 and the inverse spinel magnetite phase of Fe_3O_4. Under a fast (5 min) synthetic method, Co is likely incorporated into the rapidly forming Fe_3O_4 lattice, which has enhanced the blocking temperature, inducing a loss in exchange bias. Under slow synthesis conditions (30 min), it was suggested that Fe_3O_4 formation precedes the nucleation and growth of Co_3O_4 on the basis of standard reduction potentials (Fe^{3+} and Co^{3+} are 0.771 and 1.808, respectively). Regardless of the product, the mixed synthesis of complex nanoparticles can be tuned to a specific application by varying its mode of synthesis.

Viral Templates for Metal Oxide synthesis

Conceptually, viruses and the metalloprotein ferritin are similar in that they are both assembled protein cages that serve as a host system for mineralized *guest* materials.[9, 10] Ferritin functions to store and transport iron oxyhydroxide, and virus capsids function to store and transport organic polymers or nucleic acids.[9, 19, 34] Viruses are composed of repeating subunits that assemble into highly symmetric architectures that provide templates for nano-engineering biominerals. As molecular containers, viruses have three important interfaces: 1) exterior, 2) interior, and 3) interfacial region of protein subunits

(Figure 3).[9] Because the exterior surface of the viral capsid is highly symmetric, every functional group is spatially defined over the entire cage; therefore, reactive sites can be genetically engineered for multivalent ligand presentation.[34]

The capsid interior has been used to direct nanoparticle synthesis; for instance, the basic, positively charged interior of the cowpea cholotic mottle virus (CCMV) has been utilized for the mineralization of a range of polyoxometalate species.[9, 10] In this synthesis, empty virions were incubated with precursor ions (WO_4^{2-}, VO_3^-, MoO_4^{2-}) at neutral pH; whereupon, the virus exits in its open, or swollen, state providing a pathway for ions to flow into and out of the cavity.[10] At pH 5.0, the formation of large polyoxometalate crystal was induced because the pores along the capsid walls closed to induce oligomerization under these conditions. The mineralized particles were then isolated and purified by centrifugation on sucrose gradients, and their subsequent size distribution was documented using TEM.

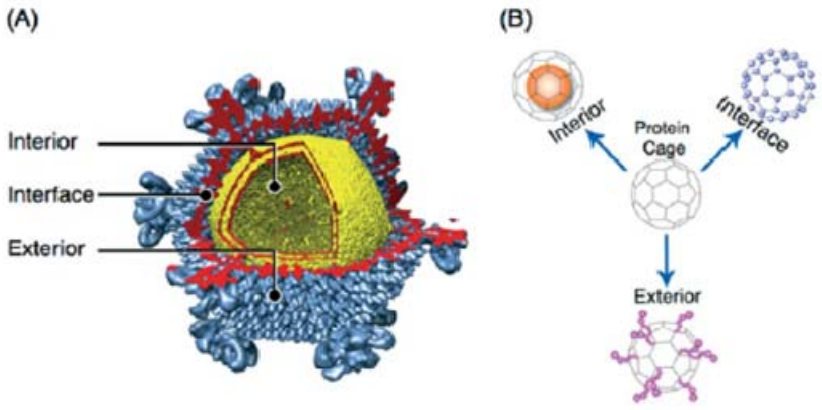

Figure 3. Reconstruction of icosahedral symmetry of Sulfolobus turreted virus. (A) Cryo-electron microscopy reconstruction and (B) Three interfaces within a protein cage available for modification.[9]

The interface between the capsid interior and exterior is defined by a series of non-convalently bound peptides. Within the icosahedral formation of the CCMV are 60, 2 nm pores that open and close, allowing ions and molecules to enter its interior as a method of communication between its interior and exterior. Because the virus capsid is a metastable, dynamic structure, manipulating its composition could introduce major structural changes from its original icosohedral formation to a sheet-like or tubular morphology. On the other hand, modifying the virus exterior with small molecules or biological ligands could have potential applications ranging from surface display or cell targeting to drug delivery.[9] Controlling the ligands associated with the virus can also be used to identify specific peptide or protein communications, similar to commonly practiced phage display methods.[9] Identifying such active peptides would enable additional, specific templates for biomineralization and a unique view into the architecture of specific viral capsids.

Hydrolysis of metal oxides using peptide nanorings as templates

The synthesis of biominerals within the confined volumes of vesicles, microemulsions, or reverse micelles elucidates yet another defined location for contained reactivity. Out of these three systems, the constrained, ionic environment within vesicles is most preferable microenvironment for the syntheses because it is not a dynamic system.[35] The biosynthesis of single-crystalline calcite within sea urchin larvae, for example, is grown inside a curved compartment with a constrained volume where the reaction is regulated by catalytically active biomolecules.[35] The high surface tensions in such confined cavities are suspected to have a considerable impact on the ensuing phase of the nanoparticle. Researchers have utilized such mirco- or nano- environments of the

sea urchin larvae as inspiration for the confined synthesis of non-natural metal oxides by incorporating similar concepts. In the following examples, self assembled reaction environments (peptide nanorings) were initiated by peptide monomers and metal precursor ions to yield uniform and specific phases of metal oxide nanomaterials.[36, 37]

As a wide band-gap material that provides light emission in a broad range, β-Ga_2O_3 has been studied to exploit its potential optoelectronic properties.[36] During its synthesis, assembled peptides were used as nanoreactors to grow the kinetically unfavored β-Ga_2O_3 (Figure 4). Once assembled, the peptide rings provided a porous microenvironment for an efficient dehydration and water-exclusion pathway during the crystal growth process. The reaction was completed in a two-step process where enzymatic peptides assembled to template crystal growth; then, ordered single crystals were aligned through aggregation-driven fusion. Nucleated particles were capped by assembled peptides in solution. Once the synthesis was concluded, the composite material was sintered at 900ºC, and the peptide templates were removed. During sintering, the particles transformed into an aggregated GaN phase.

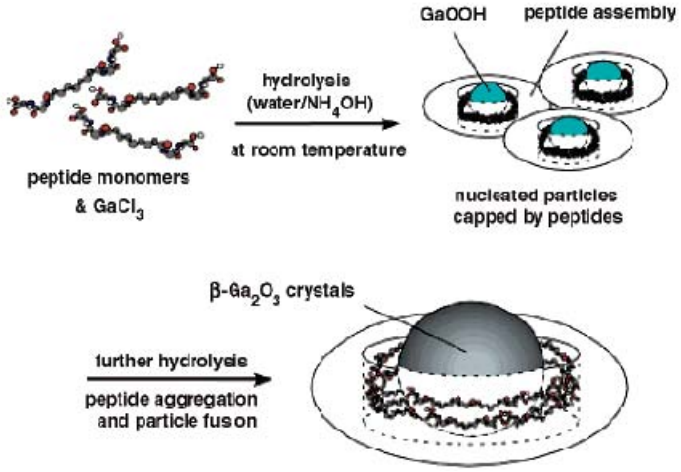

Figure 4. Illustration of catalytically grown β-Ga_2O_3 nanoparticles.[36]

Looking more closely at this synthesis, bolaamphiphile peptide monomers and (bis (N-α-amidoglycylglycine)-1,7-heptanecarboxylate) were used to cap and catalyze the growth of β-Ga_2O_3 nanoparticles. The particle capping was essential in this synthesis; without which, GOOH was synthesized (Figure 6). The bolamphiphile peptide monomers were reacted with the precursor, gallium (III) chloride, for 1 month at pH 10. After this time, TEM and SAED identified that the particles displayed 50 nm diameters, arranged in the monoclinic crystal structure. High resolution TEM images displayed layers of the peptide surrounding the core nanoparticle.

It is understood that the base solution hydrolyzes gallium precursors to form GaOOH, but it is not strong enough to carry out the reaction; for this reason, it is believed that these peptides have a catalytic function. Photoluminescence documented the emission of the nanoparticles (389 nm), which was in agreement with previously reported values for β-Ga_2O_3. FTIR spectra identified that gallium hydrolysis is completed adjacent to the carboxyl and amine moieties within the assembled peptide through a bridged metal bridged metal complex (COO—Ga-NH^{2+}). To investigate the importance of nucleophilicity of the carboxyl, the pH of the composite solution was adjusted to 7, and after 4 weeks of incubation with the gallium precursor, only GaOOH crystals were observed. At a neutral pH, the protonated carboxyl group was weakly bound to the amine group, affecting the degree of gallium hydrolysis.

Furthermore, the importance of bolaamphiphile template was also investigated. As a control, Nuraje and coworkers used the silicatein peptides that are associated with templating the hydrolysis and condensation of SiO_2 in sponge spicules. In this study, the

nucleophilic hydroxyl of the serine and the primary amine from the histidine and lysine of silicatein only catalyzed the hydrolysis of GaOOH and γ-Ga_2O_3 over a wide size range, which is not desirable for technological use.

Synthesis of ferroelectric BT nanoparticles using peptide nanorings

As previously mentioned, the ferroelectric and optoelectronic properties of ternary oxides like $BaTiO_3$ (BT) can be applied to the next generation of miniaturized capacitors or random access memories.[37] In the past, BT has been synthesized at room temperature in the cubic phase, which does not exhibit ferroelectric behavior. Nuraje and coworkers have recently reported the one-pot synthesis of ferroelectric BT in the tetragonal phase, as confirmed by electron diffraction.[37]

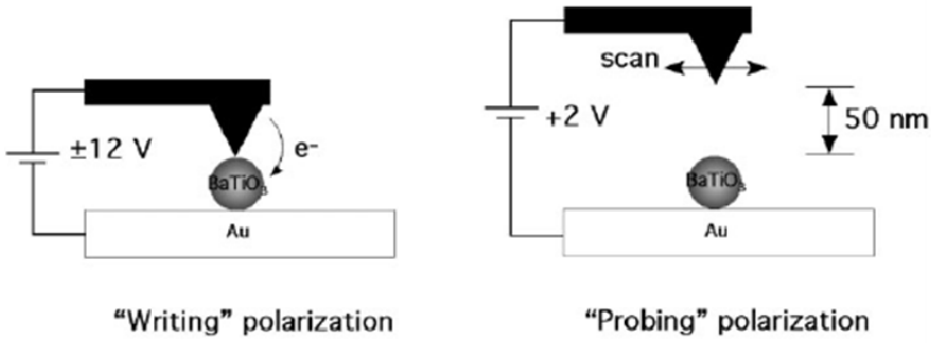

Figure 5. Schematic of EFM. Probing the electric polarization is one valuable technique used to identify the ferroelectric properties of BT nanoparticles. [37]

In this synthesis, the precursor, $BaTi(O_2CC_7H_{15})[OCH(CH_3)_2]_5$, was hydrolyzed by peptide templates (bolaamphiphile peptide and (bis (N-α-amidoglycylglycine)-1,7-heptanecarboxylate)) to produce $BaTiO_3$ nanoparticles at room temperature. When the

peptide template and the Ba-precursor were added together, after 1-4 days of incubation in the dark, the peptide monomers self assembled into nanorings. AFM was used to identify that the BT was synthesized exclusively within the nanoring cavity. The average diameter (49 ± 11 nm) of nanorings documented a monodispersed size distribution. Raman spectroscopy confirmed the formation of $BaTiO_3$ through a Ti-carboxylate ligation and a Ti-O-Ti stretch.[37] To validate this coordination, the composite solution of peptide shells was irradiated by UV light (355 nm) for 10 h. After this time, the peptide shells were displaced, inferring that the onset of irradiation rendered the Ti-carboxylate linkage ineffective. AFM identified the average diameter of the metal oxide nanoparticles, alone, as 12±1 nm after UV irradiation. Interestingly, as the pH of the peptide/precursor solution changes from 4.5 to 10, the average diameter of the system drops from 49 to 23 nm; this, in turn, affected the size of the resultant crystal (12 to 6 nm).

To test the nanoscale ferroelectric properties of BT, electrostatic force microscopy (EFM) was used to manipulate the polarization of the ferroelectric field (Figure 5). First a voltage was applied to the cantilever tip (V_{write}), which gently touches the nanoparticle surface. Once one polarization is written, the particle was probed with a lower voltage (V_{probe}) by measuring the shift in resonance of the AFM tip, using EFM. A positive applied V_{write} (+12 V) on a 12 nm particle produces a brighter contrast image with of V_{probe} +2 V. After -12 V is written onto the same particle, the V_{probe} was applied, inducing a darker contrast image.

Synthesis of ZnO from templated butterfly wings

The wonderful array of colors associated with different species of butterflies often attracts the eye for aesthetic purposes only. Used for sexual signaling or defense mechanisms (camouflage), the color of the butterfly wings is actually necessary for its survival. Designed for aerodynamics and protection, the microstructure of butterfly wing scales, or cuticular product of a cell, are composed of a light-weight, porous material with alternate layers of chitin and air.[38] Although the precise chemical composition of the scales is not known, chitin and the proteins resilin and scleretin have been identified within insect cuticle. The scales are composed of long, parallel ridges that are connected by cross ribs (1280 nm long, 380 nm wide). [39] The cross ribs do not contribute to the color of the butterfly; instead, they offer defined regions that can be manipulated for further functionalization (Figure 8).

Zhang and coworkers utilized the porous architecture and the terminal hydroxyl and amino moieties from surface proteins to direct the constrained synthesis of tubular ZnO nanowires.[38, 40] Tubular materials with high porosity are understood to have properties suitable for catalysis or device storage.[38] A zinc nitrate ($Zn(NO_3)_2$) solution in ethanol was coated on the surface of the wing after 12h incubation at room temperature.[38] The functionalized wing was washed extensively with deionized water to ensure that the Zn^{2+} ions were effectively adsorbed within the surface hydroxyl and amino groups of chitin and placed in the oven at 500 ºC for 2h. During this time, the flat scales of the wings break apart along their stress ridges and the chitin substrate is burned. The calcified product yields ZnO microtubes within the ceramic wings.

XRD confirmed that the resultant composites were a zincite hexagonal structure. FESEM was used to determine the dimensions of the resultant microtubes (3.0 μm diameter), and the shrink ratios were calculated. The distance between ridges and the length of the tubes were calculated to shrink approximately 45.7 % and 41.6 %, respectively from the original template, inferring that the microtubes grew directly from the wing scales. Cathodluminescence from the free exciton at 3.24 eV documented two emission bands (λ= 381 and 572 nm) of the as-synthesized ZnO. Although it is not definite, researchers believe that the origin of the emission is a result of center defects of oxygen, indicating that the tubes sustain a low oxygen content, which is consistent with previous ZnO syntheses using block copolymers or solid state conditions.[38]

The utility of metal oxide nanoparticles is dependent on their synthesis and subsequent magnetic or ceramic properties. Size homogeneity is necessary because the nanoparticle properties are directly related to size. Natural templates, such as butterfly scales, peptide nanorings, and bacteria or protein cages, can be tuned to induce narrow size distributions that have yet to be seen in industrial settings. These chemically engineered systems have proven to be viable nanoscale templates for the constrained biomimetic synthesis of higher ordered metal oxide nanoparticles with unique properties specific to their synthesis.

Mediated mineralization

The structure of certain biogenic organisms is understood to be mediated by the cooperative reactivity of self-assembled macromolecules within aqueous solutions. Such hierarchical, supramolecular assemblies have exposed interesting morphological

properties that can be directly applied to materials development. Diatoms and echinoderms are two independent examples that exhibit genetically controlled metal oxide structures with technologically relevant properties.[30, 41] Although progress has been made, identifying their structure directing precursors, researchers have yet to fully recapitulate their complex biomineral shapes. The following sections, however, are representative of the significant progress made in this area. By isolating the biomolecules responsible for cell wall mineralization and documenting their reactivity, researchers have begun to incorporate the specific, reactive moieties of peptide and non-peptide based analogs for the biomimetic synthesis of novel nanomaterials.

Three Tier Architecture of Nacreous Layers

Mother-of-pearl (nacreous layer) possesses interesting morphological properties that are dependent on its aragonite-biopolymer coordination. Evidence has suggested that these biopolymers are incorporated into the composite framework of the mineral and are responsible for inducing different morphological properties of the organism.[29] Electron microscopy has been used to characterize these hybrid composites and has shown that the macroscopic periodic orientation of the nacreous layer is assembled through a three tier process of repetitive growth, inhibition, and regrowth.[29] The layered aragonite composites (tier 1) have been predicted to be perfectly aligned through a series of mineral bridges (tier 2) (1-5 μm wide and 200-700 nm thick). These bridges are assembled by nano-building blocks (tier 3) that have aggregated into hexagonal plates (Figure 6).[29]

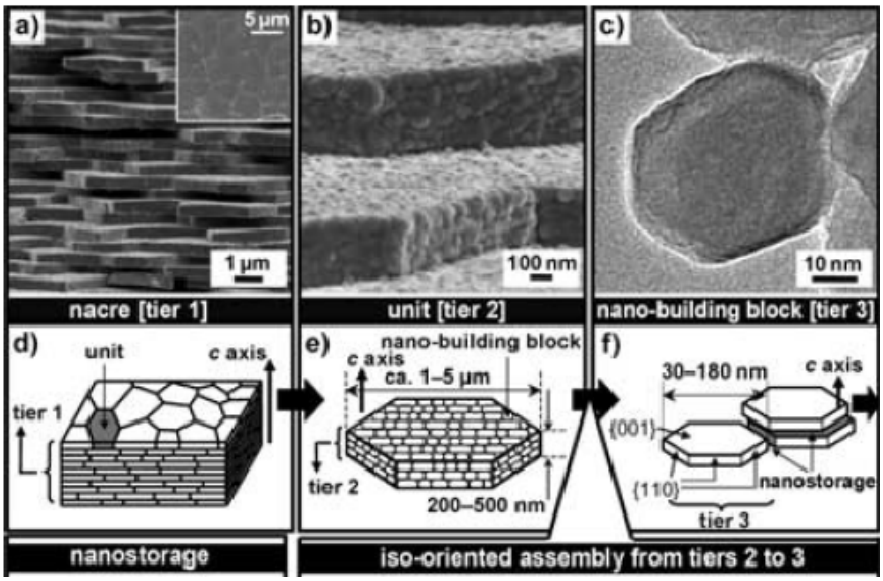

Figure 6. The three identified tiers of the nacreous layer. (A,B) FESEM images and (C) FETEM image. (D-F) schematic representations of tiers 1, 2, and 3, respectively.[29]

Non-natural mimics of the assembled nacreous layer have been synthesized, displaying similar nano-scale architectures under ambient conditions. In these studies, the biomimetic crystallization of host organic molecules, generated through of potassium sulfate (K_2SO_4) and poly(acrylic acid) (PAA) composite reaction, were shown to spontaneously form three tier assemblies. Electron microscopy revealed that tier one consisted of an assembly of plates composed of square units (tier 2), approximately 0.5-1.0 µm thick. Once magnified at a higher resolution, these squares were shown to originate at nanoscale defect sites that were bridged by 20 nm building blocks (tier 3) (Figure 7). The physical properties associated with these packed, nanoscale building blocks were probed using photoluminescence. Hydrophobic and hydrophilic organic dyes were encapsulated within the defect sites of the three tier matrices. After time,

photoluminescence documented that the stored dyes were still actively flourescing, providing an interesting source for molecular storage.

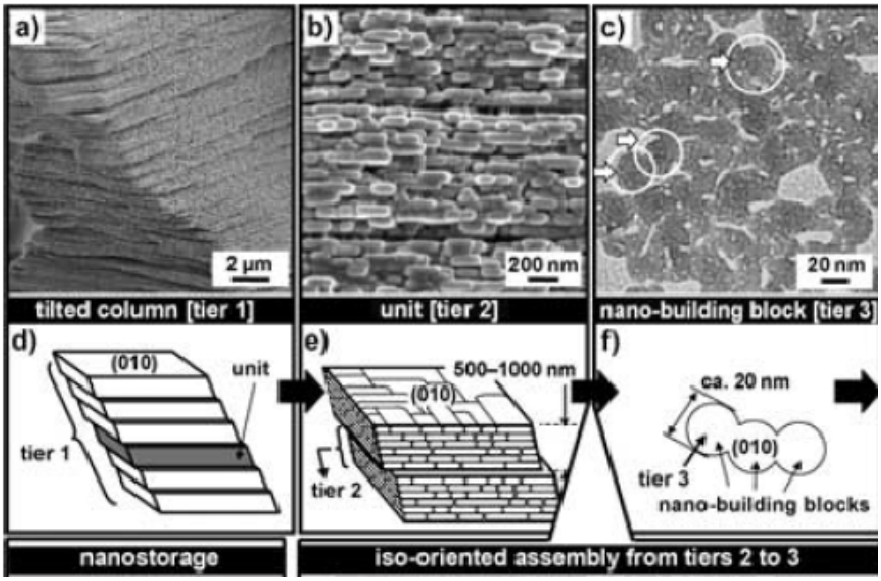

Figure 7. The three identified tiers of the K_2SO_4–PAA assembly. (A,B) FESEM images and (C) FETEM image. (D,F) schematic representations of tiers 1, 2, and 3, respectively.[29]

Echinoderms

The three tier assembly documented for mother-of-pearl can be extended to the nanoscale architectures of other mineralized organisms. The sponge skeletal organization of echinoderms, for example, is composed of calcitic nanobricks composed of one, single Mg-bearing calcite crystal. Three species of echinoderms and one shell of a sea urchin were analyzed using FESEM, FETEM, SAED, and XRD.[30] The organic composite membrane of the shells was extracted using an aqueous solution of sodium hypochlorite (5% NaClO), but the biopolymer remained associated specifically to the remaining rhombohedral calcite crystals. The nanobricks, or sub micron domains of occluded

biological macromolecules, exposed on the cell surface of echinoderms, were shown to be interconnected through a series of defined bridges at their nanoscale defect sites, similar to those found on nacreous layers.[30]

The crystalline, calcitic domains of echinoderms were studied on a molecular level and were shown to be electrostatically driven by assemblies of biomolecules with carboxy moieties. In fact, Addadi and coworkers have identified biological molecules associated with the sea urchin spine as water soluble proteins, rich in aspartic and glutamic acid.[42] These amino acids were proposed to occupy the boundary sites between the crystalline domains of the nanobricks, inducing a necessary electrostatic environment for further reactivity. Similar to nacreous layers, nanobrick growth of echinoderms is initiated along the defect sites of the biopolymer/nanobrick interface exposing potential molecular storage units (Figure 8). The reported literature on the biopolymer mediated synthesis of tightly packed nanobrick layers within species of echinoderms can be applied to the bio-inspired synthesis of non-natural metal oxides.

Utilizing the fundamental Lewis acid and base interaction, defined organic molecules were used in conjunction with appropriate precursors under variable conditions to rapidly precipitate nanoparticles with constrained sizes. Specifically, mosaic assemblies of nanowires of ZnO and nanocrystals of Mn_3O_4 and $Co(OH)_2$ were synthesized using different polymeric backbones.[43, 44] The mosaic assemblies within these metal oxides is initiated from the nanocrystals themselves. As seen in echinoderms and nacreous layers, these materials were grown, inhibited, and regrown at the defect sites of bridged nanocrystals. In these reactions, the incorporated polymeric backbone generated an electric dipole moment that induced internal self assembly of the primary crystals *in*

vitro; these assemblies then re-organized into a highly specific metal oxide crystal structure with functional properties.

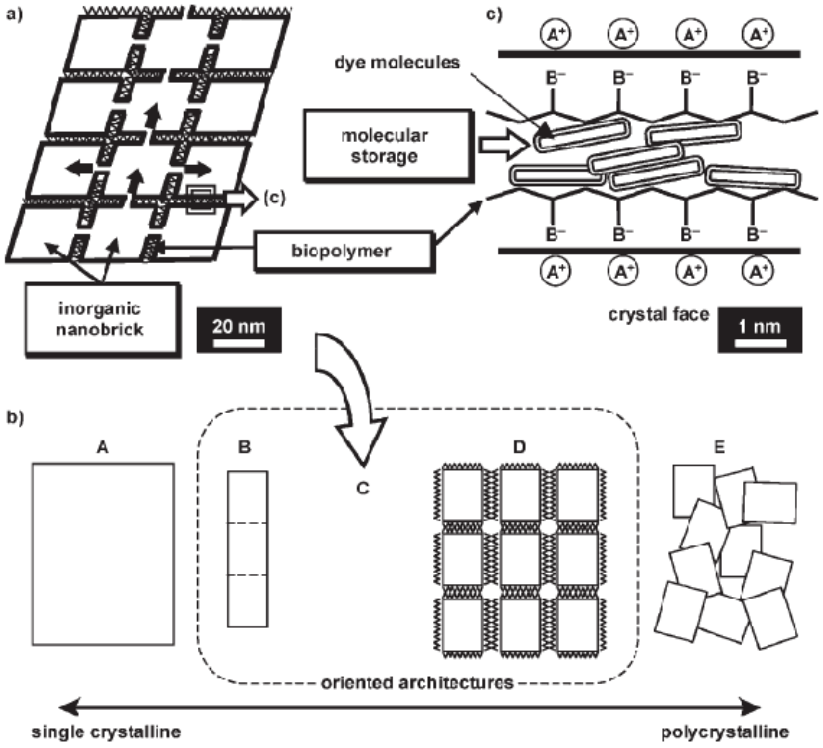

Figure 8. Schematic of nanoengineered nanobricks of nacreous layer and echinoderms. (A) Nanobricks oriented involving nanobridges, (B) schematic of oriented architectures from single crystalline (A) to oriented attachment (B-D), (C) Interaction between the nanobricks and biopolymers producing the emergence of molecular storage; and (E) polycrystalline arrangement.[30]

Diatoms

In nature, diatoms are one of the largest groups and perhaps one of the most studied single-celled eukaryotic micro algae found in almost every sea- and freshwater habitat. These microorganisms have silica-based cell walls, which range is size from ~50 to 500nm (Figure 9).[45] Although diatom silica is X-ray amorphous, they still exhibit highly

regular and rather exquisite patterns of pores, ridges, or tubular structures that are formed under genetically controlled processes. Studies using electron microscopy have revealed that the valves and girdle bands associated with silica formation are formed inside the cell within highly specialized membrane-bound compartments called silica deposition vesicles (SDVs).[46] After morphogenesis is completed, these silica species are deposited on the cell surface using SDV exocytosis.

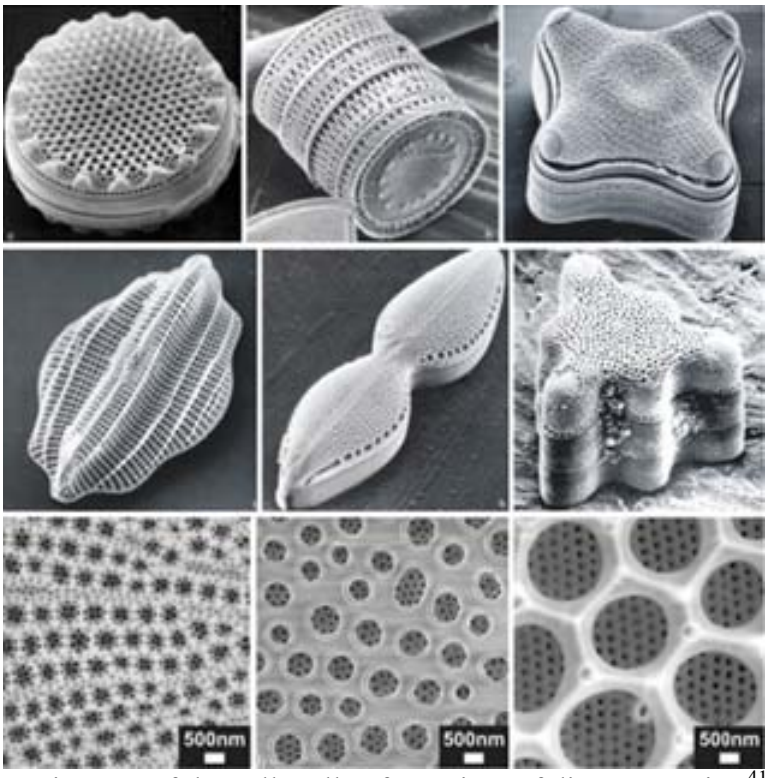

Figure 9. SEM images of the cell walls of a variety of diatom species.[41]

Currently, microelectronics relies on bulk silica as an important dielectric material that is often used as an insulating template for further reactivity. Nanoscale silica has been synthesized by polymerizing silicic acid in an aqueous system or through hydrolysis and condensation of silicon alkoxides using the Stöber synthesis.[47] The mechanism of these

two methods is unique. The first method is dominated by monomers and tetra-functionalized species. The resultant silicate sols are uniform, meaning that they are fully hydrolyzed and grow by monomer addition. On the other hand, di- and tri-functionalized species are dominant for alkoxides. Regardless of the synthesis used, these particles induce a fractal interior with minimal morphological control due to their common template, ammonium hydroxide.[47]

In nature, specific silicon transport proteins (SITs) produced by diatoms are responsible for the uptake and delivery of orthosilicic acid ($Si(OH)_4$, pK_a = 9.8) to the diatom. Within the cell, orthosilicic acid is then concentrated up to 1000-fold, resulting in the condensation of amorphous, hydrated silica.[41] Strikingly, poly-condensation of silica occurs in neutral to slightly acidic pH conditions under ambient temperatures and pressures. Although these conditions are considered mild, diatoms still have control over the product morphology. It is understood that the patterns created by diatoms are species specific, so their directed grown process must be regulated in a genomic manner.[47]

Significant effort has been devoted to determining the specific templates used by different species of diatoms in silica formation. Although diatom cell walls consist primarily of silica doped (~97%) with trace amounts of aluminum and iron, they also contain a wide variety of incorporated organic molecules and proteins.[48] In fact, solid-state nuclear magnetic resonance (NMR) spectroscopy revealed that some these molecules and coat proteins are encapsulated within the silica matrix.[49, 50] Two main templates for silica growth were identified after dissolution of the silica cell wall with hydrogen fluoride (HF) or ammonium fluoride. The following sections will demonstrate how researchers have optimized these templates and utilized them for further reactivity,

exposing interesting properties directly applicable to the synthesis of novel nanomaterials.

Biological synthesis of Silica nanoparticles

Extracted and purified from up to three species of diatoms (*C. fusiformis*, *T. pseudonana*, and *E. zoodiacus*), silaffins are polypeptides (4-17kDa) with a variety of posttranslational modifications, including proplylamino-functionalized lysine side chains (Figure 10).[45] Currently, there have been four silaffin genes identified (one from *C. fusiformis* (sil1) and three from *T. pseudonana* (tpSil1, tpSil2, and tpSil3)), which encode for eight known polypeptides. Of these four genes, only tpSil1 and tpSil2 have shown sequence similarities, likely from gene duplication; however, the overall lack of sequence similarity strongly suggests that the posttranslational modifications of silaffins are critical to their function. These posttranslational modifications include mono-hydroxylation of lysine and proline, di-hydroxylation of proline, *o*-phosphorylation of serine, threonine, hydroxyproline and hydroxylysine, glycosilation, sulfation of carbohydrate moieties, and alkylation of ε-amino groups of lysine.[48,51] These modifications are charged and stabilized through electrostatic interactions between the phosphate groups on one silaffin to the charged amines of another, inducing a self-assembled template available for further reactivity.

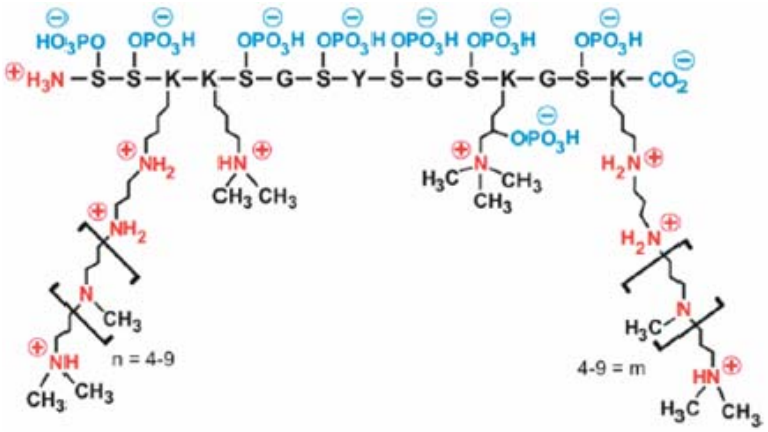

Figure 10. Chemical structure of silaffin-1 A_1 from *C. fusiformis*.[51]

The different structures associated with different species of diatoms are directly related to the silaffin being studied. For instance, spheres (silaffin-1/2L mixture from *T. pseudonana*[52]), dense plates (silaffin-3 from *T. pseudonan* [52]), or porous sheets (silaffin-1/2 H mixture from *T. pseudonana*[52] or natSil-2 from *C. fusiformis*[53]) are all a function of a precursor template. While silaffins are responsible for controlling which shapes formed in the SDV, positively charged long-chain polyamines (LCPAs) are an integral part of silica condensation.[41] The silaffins that are negatively charged must be stabilized by the LCPAs, or the recently discovered silacidins[54] (in *T. pseudonana*), to complete silica condensation.

LCPAs are non-protein components (>3.5kDa) that were found encapsulated in the silica matrix of the diatom and were isolated through a series of HF extractions.[55] Unlike silaffins, which utilize a peptide backbone, these polyamines consist of linear chains of C-N linked propyleneimine units that are bonded to a putrescine or putrescine derivative backbone. The chemical composition of these long-chain polyamines is unique for each diatom species, with variable repetitions and degrees of methylation.

Similar to reactivity of silaffins, silica production in the presence of LCPA and silicic acid requires an addition of counter anion in the form of phosphate, sulfate, or citrate ions. This electrostatic matrix is projected to induce the formation of silica by microscopic aggregation of LCPAs and subsequent phase separation into a LCPA-anion-rich microdroplet.[46] In his 2002 theory of cell wall morphogenesis, Manfred Sumper suggested that the formation of secondary patterns, as seen on the diatom cell wall, is related to the wall-to-wall distance of the areolae, hexagonally packed polyamine monolayers and the polyanion concentration, on the surface of the SDV.[14] For example, a size-control experiment using LCPAs from *S. turris* has shown that the size of nanoparticles was dependant not only on the phosphate concentration, but also whether orthophosphate or a more highly charged pyrophosphate was used.[56]

The biological mechanism of diatom silica formation has been demonstrated as a valuable source for bioinspired templates for non-natural metal oxide synthesis at ambient temperatures and near-neutral pH. Moreover, silica nanostructures can be tuned according to a specific template, providing functional properties that can be directly applied in designing nanomaterials. These syntheses have integrated moieties that are tuned for a specific function, such as encapsulation of functional enzymes[57, 58] and controlled construction of nanomaterials through nanoscale building blocks.[59-61] Therefore, this section will focus only how these synthetic strategies control and optimize silica formation, and how these materials can potentially be utilized in a variety of applications.

Biomimetic Synthesis of Silica Nanoparticles

Mimicking the nanopatterns of the diatom cell wall still remains a great challenge for materials scientists because the natural reaction mechanism still unknown, and many essential components to silica precipitation have yet to be discovered. However, it is well known that the terminal amine templates interact with monosilicic acid to induce the specific morphology of the resultant silica. A variety of non-natural silica pre-cursors and templates have been used, including tetramethyl orthosilicate (TMOS),[58, 62-69] tetraethyl orthosilicate (TEOS),[59, 70, 71] tetrakis(2-hydroxyethyl) orthosilicate (THEOS),[70] sodium silicate,[61] a silicon-catecholate complex,[60, 72] and dipotassium Tris(1,2-benzenediolato-O,O') silicate.[73] In addition, a variety of bio-inspired templates have been used, including synthetic and natural polypeptides,[59, 62, 71] polyamines,[64, 69, 72] and even modified organic materials, including cellulose[70] and chitosan.[74]

Recently, synthetic or natural polypeptides have been created or modified to serve as silica condensation templates. Many examples of these polypeptides include the poly(amino acids),[75] the diatom-derived R5-peptide,[62] chimeric polypeptides,[60, 63] block co-polypeptides,[67, 68, 71, 76] lanreotide,[59] and even the naturally occurring protamine.[61] These polypeptides have been used to produce a variety of silica shapes and sizes, which can be tuned to perform a variety of applications, including transport and separation of encapsulated materials,[58] or potentially for drug delivery.[69]

Lessons learned from the biomimetic, *in vitro* syntheses of metal oxides have presented efficient, low-temperature approaches towards developing nanoengineered materials. In fact, these approaches are being harnessed in the next-generation of biomimetic materials: 2D patterned metal oxides. For instance, a number of different

deposition techniques for biomimetic patterning have been incorporated to mimic the microstructure of the diatom cell wall. Specifically, techniques, including solenoid jet printing, lithographic patterning, and direct ink write (DIW), have been used to deposit a variety of silica precipitating precursors.[77-79] Coffman and coworkers have used both solenoid jet printing and photolithography to pattern poly-L-lysine and (3-aminopropyl)-trimethoxysilane, respectively. Although these methods provided unique approaches towards developing a controllable template for silica precipitation, they were limited by large, non-uniform spots (solenoid jet printing), or smaller, unresolved spots (lithography).[77]

Rapid prototyping techniques using computer aided deposition have been developed to eradicate these setbacks. For instance, Xu and coworkers have integratedDIW to directly deposit (40 μm s^{-1}) polyamine rich inks.[78] In these experiments, polyelectrolyte inks were loaded into a syringe and robo-casted onto a substrate using computer animated design. The patterned surfaces were then hydrolyzed with silicic acid to condense micropatterned silica. Auger electron microscopy was used to map the distribution of silica along the patterns, and it was shown that both silicon and oxygen are distributed uniformly about the pattern.[78]

From a different approach, Kisailus and coworkers integrated soft-lithograpy stamping to micropattern γ-Ga_2O_3 using a selection of catalytic enzymes associated with silicatein peptides.[79] Here, thiolyated ligands composed of nucleophilic hydroxyl and hydrogen-bonded amine moieties derived from silicatein were assembled onto poly(dimethylsiloxane) (PDMS) stamps. The PDMS stamps were then applied to gold substrates and reacted with precursor solution. The strong binding affinity between the –

SH group and gold substrates induced the formation of hydroxyl self assembled monolayers (SAMs) available for further reactivity.[79] In fact, once immersed in a precursor solution of gallium nitrate, these hydroxyl groups served as a site for the condensation of γ-Ga_2O_3. The surface energy of the ordered monolayers provided a defined area for hydrolysis of gallium nitrate and subsequent ripening, dissolution, and precipitation of γ-Ga_2O_3. This control could be used for the surface-catalyzed systems at low temperatures for novel electronic or optical applications. Additional rapid prototyping techniques, such as piezoelectric inkjet printing, are beginning to receive interest in biomaterials deposition because it is a non-contact instrument that utilizes a user-controlled waveform to deposit known amounts of material onto a variety of substrates.[80]

Processing Biomaterials

Recent advances in tissue engineering, biological sensing, and biotechnology have resulted from two complimentary forces. First, there is a natural evolution towards microscale patterning and rapid prototyping of materials as novel technologies become available. Second, patterned materials provide the capability for specific interactions with cells, proteins, DNA, viruses, and other biological structures. Processing biomaterials is not only essential for medicine and biology, they are also increasing interest in microelectronics, MEMs, sensors, display units, and optoelectronic devices. In the remaining sections, a brief overview of both contact and non-contact printing techniques, used to deposit biomaterials, will be discussed.

Microcontact Printing

Microcontact printing (μCP) is one direct contact technique that has been optimized to print biomaterials. Some patterned materials include printed lipids or polymers into tissue culture flasks or printing long-chain alkanethiols for organic based sensors onto gold substrates.[81, 82] Prior to each printing process, an elastomeric polydimethylsiloxane (PDMS) stamp is molded against a preformed master with defined patterns for a specific application; the master is often generated using photolithography.[81] Once the PDMS stamp is ready for use, it is traditionally immersed in a composite solution, or *ink*, allowed to dry over a period of time, and stamped onto a substrate, often leaving a patterned monolayer with nanoscale resolution.[81] The degree, or amount, of stamping is relative to the pressure applied to the stamp and its contact time (10-1000s) on a substrate.[82]

Recently, Zhoa and coworkers have utilized a modified version of this technique to pattern lipid tubules onto gold substrates.[83] In these experiments, a PDMS stamp was created having parallel, recessed channel walls (4-7μm apart, 0.8 μm high, and 1.0 μm, wide). The stamp was placed directly onto a glass substrate, where a solution of 1,2-bis (tricosa-10,12-diynoyl)-*sn*-glycero-3-phosphocholine (DC $_{8,9}$PC) lipid tubules was drop-casted along its open ends (Figure 11). The solution, then, aligned into highly ordered two-dimensional (2D) arrays, where they settled into the microfluidic channel walls of the PDMS stamp. The lipids were later re-patterned though a secondary stamping process (2hr contact time onto gold coated mica substrates), producing a stable, three-dimensional (3D) lipid pattern that was roughly 360 nm tall. Integrating such 2D ordered

patterns into 3D junctions is believed to potentially redefine new types of biomaterial microdevices.[83]

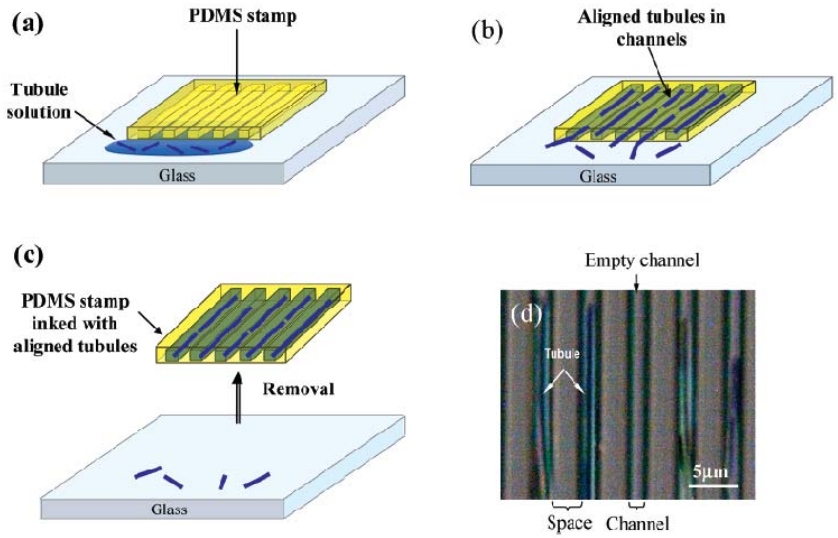

Figure 11. Illustration of microcapillary capabilities of PDMS stamp. A composite suspension of lipid tubules was dropcasted onto a glass substrate (A-C). Once the lipid tubules were assembled into the PDMS channels, their confinement was confirmed (D) through transmission mode optical microscopy.[83]

Electron beam radiation

Electron beam (e-beam) irradiation of polymeric materials into specific micropatterns has been used to investigate the adhesive nature of a variety cells. E-beam radiation is a soft-lithography technique incorporating a metal mask that can withstand the irradiation often using an Area Beam Processing System. Successful cell micropatterning could not be used to document the binding properties of a specific cell on a substrate, but it could also be used to identify its primary binding sites.[84] Furthermore, seeding cells onto controllable, dynamic substrates can also expose a number of interesting properties necessary for important applications, such as cell based biosensors or even defining basic

cellular mechanisms.[84] In order to realize these applications, a number of parameters have been tested.[84] Factors used to control cell adhesion at the molecular level, such as the effect of external stimuli, the polarity of the patterned substrate, or the effect of surface selective adhesion, can be varied to produce a number of outstanding properties.[84]

Both cell adhesive and non-cell adhesive materials can be patterned onto a surface to eliminate the effects of non-specific cell binding. Common biological components that do not bind to cells, such as poly-ethylene glycol (PEG), bovine serum albumin (BSA), or amphiphilic phospholipids, can be patterned to resist the non-specific protein adsorption that is associated with cell media or protein byproducts secreted from cells. On the other hand, extracellular matrix (ECM) glycoproteins, such as collagen and fibronectin, contain a specific, linear peptide sequence, containing arginine, glycine, and aspartate (RGD) that have been shown to interact with cell membrane proteins for specific cell binding.[84] During these printing cycles, a pre-defined mask is irradiated on the surface of a substrate immersed in a solution containing one of these materials, dried in air, and removed, leaving a specific micropattern.

Okano and coworkers have patterned poly (*N*-isopropylacrylamide) (PNIPAAm), a material similar to BSA and PEG in that it does not adhere to cells at room temperature.[85, 86] In this experiment, a composite solution of PNIPAAm dissolved in propanol (55 wt %) was uniformly coated inside a commercial cell culture dish. The polymer was then patterned, using standard e-beam lithography, onto the surface of a cell culture dish to test the dynamic behavior of cells for potential clinical applications. A metal mask (60 mm o.d. with 1mm circular holes) was then placed into the dishes and subjected to e-beam irradiation (0.25 MGy).[86] The PNIPAAm-grafted cell culture dishes

were washed extensively, and their properties were studied. Interestingly, PNIPAAm alters its solubility and subsequent hydrophilicity at 32°C, its lower critical solution temperature (LCST), making it a viable template for controlling the reactivity of cell patterns.[85] When cells were seeded below the LCST, they adhered only to the regions that were not patterned with PNIPAAm. Once the temperature was raised above the LCST, the cells adhered to all surfaces, providing an interesting example of region-selectivity of cells.[86]

Non-contact Printing

Although contact printing techniques have been used to create intricate patterns at relatively low costs, the arrays are often plagued by constant stamp fatigue and unstable patterns; in fact, some nanopatterned surfaces have been reported to experience post-deposition degradation.[87, 88] More importantly, because contact printing requires manual deposition, it is not suitable for depositing production scale quantities necessary to compete with current high-throughput facilities. Techniques that incorporate robotic deposition, such as DIW, syringe solenoid jet printing (SSP), or inkjet printing (IJP), are some examples of alternative, non-contact deposition techniques that have been developed to alleviate the element of user-error for printing biomaterials.[77, 79, 89]

In contrast to other prototyping techniques, non-contact printing is a relatively straightforward fabrication process due to its computer graphical interface. In general, many formats of two-dimensional drawings, pictures and structures can be converted to a bit map image, which can then be interpolated into X- and Y-coordinates to deposit materials in a printed pattern. Most non-contact printers also rely on the chemical

properties, specifically the surface tension and viscosity, of the material being printed. A composite solution, or *ink,* is tailored specifically to the printing device that is employed, and the pattern resolution (drops per inch (dpi)) is affected by the method and properties of a print cycle. The thickness and dimensions of a patterned film are not only related to the properties of the *ink* but are also dependent on a number of controllable parameters that include but are not limited to, nozzle diameter, solvent, and substrate.[80] Once released from a syringe or nozzle, the droplet maintains a spherical shape, with dimensions of πr^3; however, once it hits the surface of a substrate, it will adjust its geometry over post-impact time to form one of three primary geometries: a dome, a cylinder or a torus. Such high resolution patterning techniques have many potential biological and medical applications that will be discussed below.

DIW and a SSP rely on the *direct writing* of continuous flow ink filaments through a cylindrical nozzle (DIW) or syringe (SSP). DIW has been used to deposit a number of composite inks, including organic ligands, polyelectrolyte composites, or colloidal solutions, and the resultant patterns are developed through layer-by layer deposition.[90] Xu and coworkers have used DIW, for instance, to pattern (40 $\mu m\ s^{-1}$) polyamine rich inks that were mineralized to yield microscale feature sizes.[89, 90] In these experiments, the polyelectrolyte ink is loaded into a syringe and robo-casted onto a substrate using computer animated design. The patterned surfaces were then mineralized through hydrolysis with silicic acid to condense micropatterned silica, similar to micropatterns found on the cell walls for marine diatoms.[89] Auger electron microscopy was used to map the distribution of silica along the patterns, and it was confirmed that both silicon and oxygen were distributed uniformly about the pattern.

SSP has the capability for rapid actuation, making the solenoid type of dispenser ideal for non-stop reagent dispensing, as they have become integral components to high-throughput laboratory applications in pharmaceutical industries. These printers incorporate a microsolenoid valve and a syringe pump, similar to the nozzle used in DIW that is used to compress the fluid in the reservoir. When opened, the solenoid valve creates a pressure wave that forces fluid through the orifice.[91] Currently, there are three methods of solenoid dispensing: aspirate-dispense, flow-through, and isolated. Once expelled from a syringe, droplets are released in a continuous flow, which yield large, non-uniform patterns. Although these patterns do not possess the resolution necessary for developing 3D biomaterial devices, they can be used for liquid dispensing on larger scales.[77,91]

The pressing need for smaller drop sizes, faster printing speeds, higher accuracy in drop-placement, and higher resolution patterns with biological applications has inspired the immergence of drop-on-demand printing under ambient reaction conditions. Drop-on-demand techniques, such as electrohydrodynamic jet (e-jet) printing, solid free-form fabrication (SFF), or piezoelectric inkjet printing, are among a few notable examples of rapid prototyping techniques that pattern materials into 3D constructs on a moving platform.[80, 92, 93] The design of such constructs with minimal feature sizes in the microliter to picoliter resolution has been demonstrated and will be discussed below.

E-Jet Printing

One drop-on-demand technique, electrohydrodynamic jet (e-jet) printing, utilizes an internal electric field to pattern submicrometer-range droplets onto a known surface.[93] In

this process, a syringe pump or a pneumatic pressure controller is connected to a glass capillary (i.d. = 0.3-30 μm, o.d.= 0.5-45 μm), which serves as a single printing nozzle. To minimize the probability of particle clogging, the capillary is coated with a thin layer of gold and is supported by a fixture, which is connected to the pump as the print head. A d.c. voltage is applied between the nozzle and the conducting substrate inducing electrohydrodynamic flow. Once a critical electric field is reached, the electrostatic (Maxwell) stress of the fluid ink overcomes its capillary

tension, and a droplet is released onto the grounded substrate.

This process has been utilized to deposit a range of electronic devices of printable organic and inorganic inks onto a variety of substrates with ~10 μm feature sizes.[93] Park and coworkers have printed thin-film transistors (TFTs) onto plastic substrates. In these experiments, single-wall carbon nanotubes (SWNTs) were printed and characterized as the semiconducting material. The SWNTs were suspended in a solution of octyl-phenoxy-polyethoxyethanol (6.9 mg ml^{-1}) and were printed onto glass and quartz substrates. The arrays were shown to consist of 2.5 SWNTs/10 μm spot sizes. The current outputs increased linearly with $1/L$, where the *on* to *off* ratio currents ranged from ~1.5 and 4.5. Although this method produced high resolution patterns, the printed droplets are still inundated by their substantial charge due to the printing process.

SFF Printing

Solid free-form (SFF) printing has been used to design complex scaffolds for organ printing or tissue engineering.[89] This technique builds 3D structures using layer-by-layer deposition. Some SFF systems are commercially available and have been shown to

process inks using either a chemically or thermally powered nozzle. In this process, the liquid monomer or sintered powder is photopolymerized for printing. Organ printing, has recently gained attention,[94] partially due to organ transplant shortages. An organ can be described as an anatomical description of a group of cells that function together in eukaryotic organisms; they are maintained by the organism's nutrient supply and can be described as multicellular *devices* that appear as simple looking as a leaf on a pea plant or as complex as a multifaceted mammalian heart. While essential parameters required for successful organ printing are still unknown, inkjet printing using SFF can still be utilized as a viable method with controllable parameters for depositing single components of organs.

To begin the printing process, 3D image files of the living organs are transposed into 3D computer-aided design (CAD) file that produces a 3D computer aided manufacturing (CAM) file. The printer's software then registers the CAM file and accurately deposits eukaryotic cells appropriate to that organ type in a layer by layer construction method. The final product is a 3D structure that resembles the starting imaged organ in both size and cellular componentry. Applying the theory behind developmental biology to novel technologies has exposed a number of interesting applications including organ printing. It is understood that the vasculature density of primary organs is the one of the most important components for adequate organ function; without which, essential processes such as cell apoptosis or necrosis will be inhibited.[94] Moreover, the embryonic organ tissues can be compared to viscoelastic fluids with specific flow and fusion kinetics. For this reason, an ink must be synthesized for printing, so that most deposited, the cells would fuse together to form a disc for tubular tissue. Once synthesized, patterns are

created using a computer graphical image and layer-by-layer deposition of a thermo-reversible gel for cell fusion (Figure 2). Mironov and coworkers have printed a multicellular spheroids composed of Chinese Hamster Ovary cells into a collagen hydrogel (1 mg ml^{-1}).[94] Hydrogels were incorporate as a mimic of the cells' natural habitat, the ECM, which provides an environment for the cells to attach and grow, permitting fusion of cell aggregates. For proper organ printing to be realized, basic theories of developmental biology must hold true post-processing, as well.

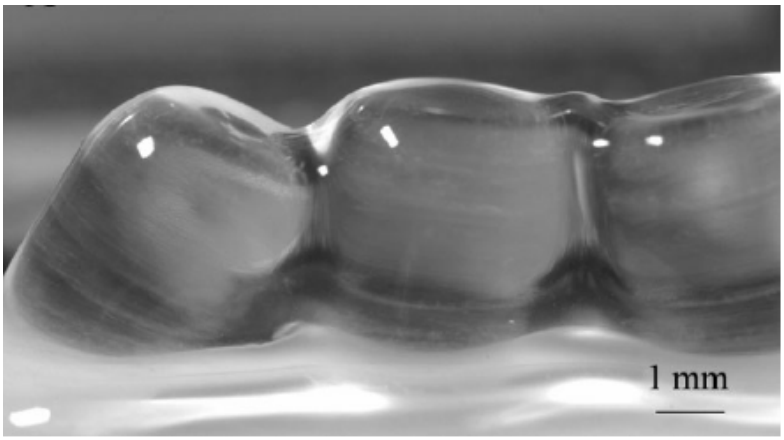

Figure 12. Printed alginic acid (2% in 0.25M $CaCl_2$ buffer) tubes. $CaCl_2$ is known to promote cross-linking of alginate, producing a resultant 3D construct. Picture was taken immediately after printing.[89]

Piezoelectric Inkjet Printing

Piezoelectric inkjet deposition is an alternative to e-jet and SFF printing, as it is another non-contact, non-destructive technique for patterning biomaterials ranging from multi-cellular components to electronic devices. The DMP, specifically, uses a piezoelectric printhead that consists of a piezoelectric transducer, 16 nozzles (21.5 μm diameter, spaced 256 μm apart), a manifold, an ink pumping chamber, and a fluid inlet passage. A user-controlled voltage is applied to the printhead that induces a deformation

of the lead zirconate titanate (PZT) piezoelectric transducer.[80] This deformation creates mechanical vibrations that generate acoustic waves, releasing a droplet from the chamber through the nozzle. Other piezoelectric print heads are categorized based on the deformation mode of the transducer (e.g., squeeze mode, bend mode, push mode, or shear mode) powered by voltage to a thin piezoelectric ceramic structure, which is constructed in the plane of the wafer.

Although it is still a relatively new deposition technique, the DMP has already been recognized as a highly reproducible rapid prototyping technique with nanoscale resolution.[80] Materials such as monofunctional acrylate esters for the advancement for medical prostheses, sinapinic acid for more sensitive MALDI-TOF matrices, and hybrid composite multi-walled carbon nanotubes (mwCNT) for direct electrochemical oxidation, have already been printed, demonstrating the versatility of the printer.[95] In the case of mwCNT prining, a mwCNT composite solution (1 mg ml^{-1}) was synthesized in the presence of propylene glycol, salmon sperm DNA (1 mg ml^{-1}), and 1 μg ml^{-1} of a DNA probe (DAPI). Once synthesized, the solution was inserted into a standard print cartridge (1.5 mL), and printed onto gold, glass, and sapphire substrates at variable voltages. The average spot size of the mwCNT averaged to be 98.4 ± 5.4 μm, where fluorescence was localized uniformly across the surface area of each spot.

Conclusion

With the advent of such readily available deposition techniques, even more metal oxides can be printed on the 2D scale.[80, 95] The constrained and unconstrained syntheses of metal oxides that have been established in literature can now be incorporated in

conjunction with these technologies to bridge the *in vitro* and macromolecular worlds of biology and materials science together expanding the new frontier in nanomaterial design.

Regardless of the system, the techniques available for printing biomaterials have expanded to produce highly functional materials. Contact printing techniques, such as μCP or e-beam lithography, produce patterned monolayers or grafted polymers with nanoscale resolution. Non-contact deposition, such as piezoelectric, E-jet, or SFF printing, are rapid prototyping techniques that pattern a range of materials onto moving platforms. By controlling the composition of the printed material, the specific pattern, and the number of print cycles, these highly reactive 2D and 3D constructs could serve as the basis for future functionalized surfaces.

Dissertation Aims

In the remaining chapters, the subject of this thesis will be shifted, focusing exclusively on piezoelectric inkjet printing for patterning multicomposite biomaterials. The focus of **Chapter II** will include designing biomaterial inks, tuning their operating parameters, and characterizing the output analysis of the materials printer. **Chapter III** will spotlight printing biomimetic inks for reactive, functional surfaces; wherein, the development and utility of a bio-inspired ink is discussed. Finally, **Chapter IV** will focus on a specific application of inkjet printed materials using SECM to map the current output associated with printed metal particle films.

CHAPTER II

OPERATING PARAMETERS AND OUTPUT ANALYSIS OF MATERIALS INKJET PRINTER

Introduction

As the controlled deposition of functional materials such as proteins, cells, polymers, and antibodies required for cell-based biosensors,[96-99] bone tissue engineering supports,[100] or antimicrobial devices[101] has recently gained attention, the demand for immobilized, hybrid biological devices has increased.[87, 102] As described in Chapter I, deposition instruments, such as CVD and STL, have successfully reproduced the nanometer scale deposition of semiconducting materials required for the rapid prototyping in industrial device manufacturing. However, their high temperature reaction environments and time consuming protocols are unsuitable for biomaterial deposition.[87] In this chapter, the viability of piezoelectric inkjet printing as a rapid prototyping technique has been explored as a function of fluid characterization, operating parameters, and the output analysis of the DMP.

Just Push Print—a command specific to operating inkjet printers in almost every home or office has recently been translated to research laboratories across the world as a common method to direct immobilization of functional, three-dimensional (3D) devices. In contrast to other materials prototyping techniques, inkjet printing is a relatively straightforward fabrication process due to its user-friendly computer graphical interface. Derived from standard desktop printers, materials inkjet printers generally are

characterized as a drop-on-demand technique that has been adapted for processing a number of multiplexed, biomaterial constructs under ambient reaction conditions.[80, 89, 93] However, developing jettable fluids and optimizing proper printing parameters still remains a challenge for functional material adaptation. In this chapter, both of these challenges will be addressed in the context of piezoelectric inkjet printing using the DMP.

In contrast to other multi-step production methods, piezoelectric inkjet printing is an additive process that precisely deposits metered quantities (μL- pL) of fluid onto a variety of substrates including glass, silicon, plastics, organic thin films, and metals based on a user generated pattern.[103-105] The resolution of the printed pattern is determined by a number of factors, including substrate/fluid contact angle, nozzle size, lateral resolution of the printhead, and the chemical properties of the fluid, including density, surface tension, and viscosity.[104,106] During drop formation, energy is distributed between the fluid's viscous flow, surface tension, and kinetic energy, where the volume of jettable fluid is directly proportional to the nozzle size.[80, 107] This flexibility enables development of microscopic patterned thin films using a wide range of functional, jettable materials at a variety of resolutions.

In general, 2D drawings, pictures, or structures, formatted as a bitmap image, can be translated into X and Y print coordinates for drop-on-demand deposition.[89, 92]
Each individual nozzle ejects a drop with a tail or ligament that coalesces with the drop during flight to make a volumetric sphere; upon contact with the substrate, the sphere alters its 3D structure to become columnar or hemi-spherical.[80] Once immobilized, the resulting printed image becomes a compilation of drops where the third dimension is

equal to film thickness, a physical property that is dependent on particle loading, drop spacing, and drop spread. Once this critical but iterative R&D phase of material evaluation is complete, then the fluid inks are ready for production-level use.

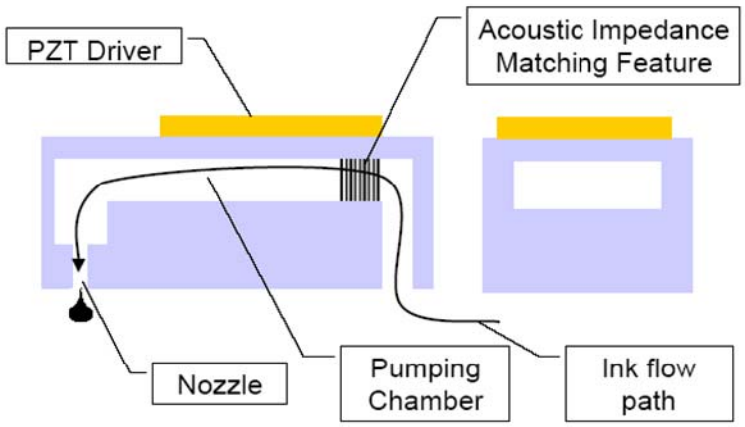

Figure 13. The jetting schematic diagram of the DMP.[4]

Because of the very nature of the instrument, proper DMP function is dependent on its piezoelectric printhead. The DMP uses a MEMs printhead with a patterned PZT ($Pb(Zr_{0.53}Ti_{0.47})O_3$) piezoelectric transducer bonded to a silicon diaphragm.[95, 96, 99, 101, 108] This powered piezoelectric unimorph is constructed in the plane of the printhead, where the silicon chip is bonded to a molded liquid crystal polymer frame at an electrical interface.[109] Once an electronic pulse is initiated using the FUJIFILM Dimatix software, then an internal acoustic wave is generated within the nozzles of the printhead, driving drop formation.[80] The printhead, itself, consists of 16 nozzles (spaced 254 µm apart, effective diameter 21.5 µm), and the number of firing nozzles can be adjusted according to the desired deposition rate (Figure 13).[99, 102, 110] During a printing cycle, the electronic

pulse to the printhead is maintained for each fluid and optimized for printing sustainability.

The fluid module, also referred to as the DMP ink cartridge, is fabricated with a flexible polypropylene reservoir and protective rigid polypropylene casing. The volume of the reservoir is small (1.5 mL) to conserve expensive fluids. Once a voltage is applied to the printhead, fluid flows directly from the reservoir through a small column into the device, through a silicon acoustic terminator, and then into a pumping chamber. After this point, the fluid flows down a descender perpendicular to the wafer plane and out of the nozzles.[99] The silicon nozzle/air interface is coated with a proprietary non-wetting material to reduce wetting of low surface tension fluids and to facilitate printhead maintenance, and the flight of the ink droplet from the nozzle to the substrate is captured using a stroboscopic broad band, white-light emitting diode and a CCD camera with 4x magnification.[80, 95] The camera's field view is approximately 1.2 x 1.6 mm with a resolution of 2.5 μm per pixel.[95] During a typical printing cycle, the average velocity of a drop from the nozzle to the substrate was experimentally calculated to be 9.25 m sec^{-1}, which is 10 x faster than standard desktop printers.[111] This construct is the jetting module portion of the printhead that snaps to the fluid module to complete the FUJIFILM Dimatix disposable cartridge.

Successful printing requires ink optimization. Previous research has focused on controlling solvent effects on the material to be printed.[112, 113] Optimizing inks by understanding their rheology and their intermolecular interactions will help produce uniform thin films with sustainable materials applications.[95, 112-114] Typically, deformations on the macroscopic level are due to the viscoelastic properties, or the onset

of molecular motion, of a material. In order to avoid said deformations in spot formations, proper DMP printing requires viscosities ranging from 8-15 mPas and surface tensions around 28 dynes cm^{-1}; once these chemical properties are met, a specific, pulsed voltage is applied to each nozzle through a requisite user-controlled waveform, producing spherical volumes regardless of ink composition.[95, 102, 115]

Low viscosities, low boiling points, high surface tensions, and non-Newtonian behaviors are hallmarks of printed thin films but are all generally unfavorable chemical characteristics for inkjet inks. For this reason, the Dimatix Drop Manager software was created to tune jetting parameters, specific for each jettable ink. Using this software, a waveform can be optimized, so that parameters, such as the frequency, wave shape, wave duration, and applied voltage, may be manipulated to produce the optimal electronic signal. This signal is then tuned to drive PZT movement within the printhead nozzles.[95] Directing these parameters has advanced array printing and has played a significant role in developing inkjet technologies.[95]

In our analysis of the DMP, five composite inks were studied: two commercially available silver inks and three inks synthesized in the laboratory. As previously mentioned, for proper DMP printing, each ink must have viscosities ranging from 8-15 mPa s and surface tensions around 28 dynes cm^{-1}; once these chemical properties are met, a specific, pulsed voltage is applied to each nozzle through a requisite user-controlled waveform, producing spherical volumes regardless of ink composition.[95, 102, 110] For this reason, the chapter will be divided into two sections. First, a commercial, conducting silver ink and a synthesized, conducting polymer ink were prepared for printing. In this study, the initial ink formulation, processing, and post-processing parameters were

investigated. Proper jetting parameters required for high performance printing are a necessary prerequisite for reproducible deposition, for even the smallest amount of discontinuity will alter the functional properties of the patterns. [116]

In the second section, the output analysis of three biomaterial inks—all with similar viscosities and surface tensions—was studied using a quantitative approach. Real-time fluid analysis was developed using a modified version of the QCM; subsequent analysis involved microscopy and contact angle measurements. The QCM is a versatile instrument that has been used as either a label-free immunosensor, a bacteria detector, or even a mass balance in metal vapor deposition.[117] Regardless of its application, QCM reproducibly provides the high sensitivity measurements required for quantitating mass on a nanogram scale, so it is well suited for our study.

The QCM is a piezoelectric instrument where an applied electric potential produces a corresponding internal, mechanical stress. Oscillation of the electric field induces an acoustic wave, which proliferates across the crystal surface. Once a monolayer of material is deposited onto the crystal, the frequency of oscillation decreases proportionally with the mass of the film, as seen in the Saurebrey Equation (Eq. 1).[117, 118]

$$\Delta f = -C_f \Delta m \tag{1}$$

Here, C_f is a sensitivity factor that is dependent on the crystal thickness, which correlates to an oscillation typically at 5 MHz or 9 MHz; Δm is the change in the mass of material added, assuming a rigid, tightly coupled layer is deposited, and Δf is the change in frequency. C_f for a 5MHz crystal, used in these experiments, has been previously

determined to be 0.0566 Hz/ng/cm^2 at 20°C. While this approximation held true for gas phase metal deposition, it did not hold true when the QCM was used in liquid systems. When an experiment is run in liquid, several additional factors, such as viscosity, density, and viscoelastic effects from solvent loading must be accounted for, as they could cause overestimations of mass loading, also affecting Δf.[119]

$$\Delta f = -C_f \Delta m - C_f (\Delta \rho \eta / 4\pi f_o)^{1/2} \quad (2)$$

In this equation, the second term is related to the liquid loading effects, which is incidentally not discernable from mass loading (Eqn 2). In order to get solely mass loading changes, the liquid must be de-coupled from this equation, which is done by measuring the loading resistance, ΔR_L. R_L is the resistive liquid loading that is directly affected by the density and viscosity of the contact solution only. An experimental calibration ensures accurate mass measurements by incorporating a sensitivity correction factor for pure resistive loading for a 5MHz quartz crystal (Eqn 3).[118]

$$\Delta m = (-\Delta f (2.095 \times \Delta R)) / 165.54 \quad (3)$$

Incorporating the sensitivity and capability of the QCM to detect nanoscale mass changes associated with real-time fluid deposition, the viability and reproducibility of inkjet printing will be determined.

Experimental

Printer

The DMP-2831 (FUJIFILM Dimatix, Santa Clara, CA) was used according to packaging instructions. The DMC-11610 (10 pL) cartridges were removed from their storage bags and after degassing, 1.5 mL of fluid was injected into the cartridge. The cartridge was manually placed into the DMP carriage. The Drop Watcher camera system was activated utilizing the Drop Manager software. The default spit purge spit cycle was repeated until pulsating fluid could be seen at the nozzle plate. The time of flight (TOF) of the ~10 pL drops was recorded using a built-in stroboscopic broad band white light emitting diode and a charge coupled device camera with a high resolution 4x magnification lens that has a spectral response of greater than 60% between 400 and 700 nm. The camera's field of view is approximately 1.2 x 1.6 mm. The strobe frequency was matched to the firing pulse frequency (1 kHz for this application), and the motion control software's built-in variable delay and drop refresh rates were employed for visualization.

Conductive Inks

Two percent (2%) glycerol (Sigma Aldrich, St. Louis, MO) was added to a poly (3,4-ethylenedioxythiophene) poly(styrenesulfonate) (PEDOT/PSS) aqueous dispersion (H.C. Stark, Goslar, Germany). ANP Silverjet nanopaste (Advanced Nanoproducts, Chungcheonguk-do, Korea) and Cabot Inkjet Silver Conductor (Ag-Ij-G-100-S1, Albuquerque, NM) were used as packaged. Fluids were sonicated in a water bath in a

Branson 1510 sonicator at room temperature using highest sonic level for 30 minutes. Fluids were degassed for 2 hours at 5 mbar pressure in a degassing chamber.

Biomaterial Inks

The mwCNTs (1 mg ml-1, outer diameter 20-30 nm, wall thickness 1-2 nm, length 0.5-2 μm; Sigma Aldrich) were mixed in a polypropylene glycol solution containing Surfynol 104PA (Air Products), salmon sperm DNA (Invitrogen), and 4,6-diaminidino-2-phenyl indole (DAPI; Sigma Aldrich). The surface tension was measured as 33 dynes cm-1. During the mwCNT printing cycles, the voltage of the nozzle was maintained at 28 V, and the maximum frequency of the pulses was 1.0 KHz. A nanosphere solution (0.21 μm diameter, FITC surface labeled polystyrene beads, Bang's Beads) was diluted in a glycol composite solution (1:1000).

Substrates

Clean glass wafers were purchased from VWR (VWR Scientific, West Chester, PA). Both Kapton® (Dupont, Wilmington, DE) and Teslin® synthetic thin films (PPG Industries, Pittsburg, PA) were kept clean after purchasing and cut into 8 x 11 inch sheets using laboratory scissors that had been cleaned with 70% ethanol (Sigma-Aldrich, St. Louis, MO). Single-side polished 150 mm silicon 100 wafers were obtained from Silicon Quest International (Santa Clara, CA) and sputtered with 300 nm gold layer using an Au target and a converted TES sputter machine.

Contact Angle Measurements

Contact angle measurements were carried out using a VCA Optima XE (AST, Billerica, MA). 2 μL samples were manually pipetted for the measurements. The sample position between the LED backlight and the computer-interfaced camera was adjusted for optimal height and focus and then video captured. The associated software fit the silhouette and calculated the contact angle.

Annealing

After printing both ANP Silverjet nanopaste and Cabot Inkjet Silver Conductor, samples were placed in a clean Yamato DX400 gravity convection oven (Santa Clara, CA) and baked for 1 hour at 200°C.

Scanning Electron Microscopy

Scanning electron micrographs were obtained using a Philips XL30 ESEM. Resolution was obtained based on operating voltage. Operating voltage employed was 5 kV under variable magnifications.

Resistance Measurements

Resistance measurements were obtained using a Fluke 110 True RM multimeter. Anode was put at one end of silver contact on glass wafer and cathode was placed on top of other end of silver contact. Electrodes were manually held during measurements.

QCM

The QCM (Maxtek Inc.) was used as an independent physical method to quantitate the printer's reproducibility during deposition. In these experiments the QCM was used with 1 in. diameter 5 MHz quartz crystals with Cr/Au electrodes (1.28 cm^2 electrode, and 34.2 mm^2 sensitive area). The original design[118] was altered by attaching two copper wires to the gold electrodes of the quartz crystal by silver epoxy (Figure 14). The crystal was stabilized on a glass slide with an O-ring and was then connected to the RQCM box and placed onto the platen of the DMP. Frequency measurements were adjusted to compensate for density and viscosity effects of the printed solution in order to achieve an accurate mass measurement, and mass measurements were derived from known sensitivity factors.[119,117] QCM sensitivity is specifically known to have a Gaussian distribution across the electrode overlap area,[120] exhibiting increased sensitivity at the center and decreased sensitivity at the fringes. Confining array printing to a 4 mm^2 region at the center of the crystal ensured a relatively constant sensitivity of 0.260 Hz/ng and provided the quantification of the average mass for one spot of printed material.[117, 118]

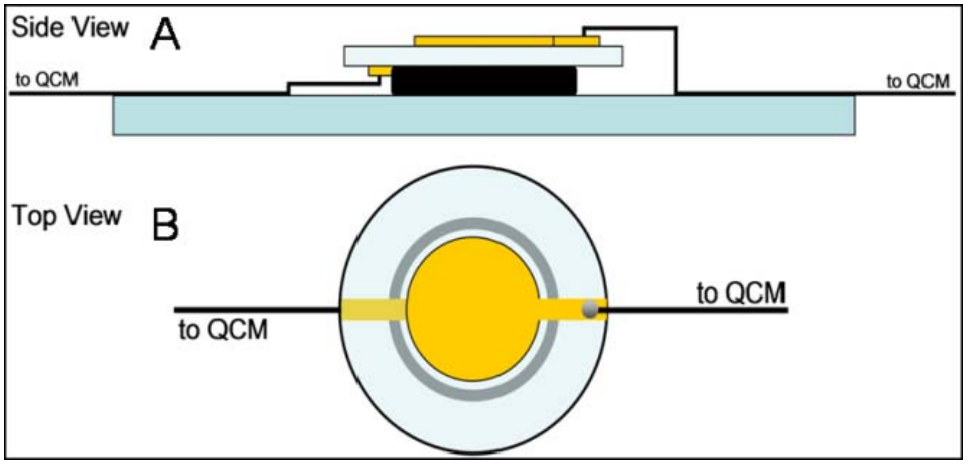

Figure 14. Side and top views of QCM crystal adapted as mass balance. **A**. The side view of the apparatus shows the crystal was stabilized onto a glass slide with an O-ring. **B**. The marked square shows the 4 mm^2 printing area as seen from the top view of the crystal.

Results and Discussion

Part I: Optimizing Jetting Parameters for PEDOT/PSS and Silver Metallo-Organic Inks

Reliable printing procedures for the two conductive precursor inks were examined. In these experiments, the ANP silverjet ink was studied as a control to the laboratory synthesized PEDOT/PSS ink. The voltage required for uniform jetting was tuned specifically to each ink, ensuring reproducible drop volumes. Images of the jetting fluids were captured using the camera and software system of the DMP software.

In developing the PEDOT/PSS ink, glycerol was added to the stock solution to increase its overall viscosity to 11 cps, which corresponds to a surface tension of 32 dynes cm^{-1}. The PEDOT/PSS waveform included a maximum jetting frequency of 1.0 kHz for a pulse width of 17.0 ms. The pulse peaked at maximum voltage 2.2 ms for 4.8

ms and recovered with a 5.1 ms slope to 20% maximum voltage that was held for 1.5 ms. After which point, the voltage was increased to 40% maximum voltage in 1.2 ms, held for 1.2 ms, dropped to 0V in 0.3 ms, and held for 2.0 ms. This waveform is a critical parameter for jetting this particular fluid.

The viscosity and surface tension values of the commercial ANP ink were similarly calculated (9 cps and 26.5 dynes cm^{-1}, respectively). This fluid jetted at a maximum frequency of 5.0 kHz with a pulse width of 13.2 ms. The pulse peaked at a maximum voltage after 4.9 ms and remained there for 4.3 ms. It then recovers to 25% of the maximum voltage over 0.3 ms; wherein, the voltage is maintained for only 0.3 ms and is followed by an increase 65% maximum voltage over 0.3 ms for 3.2 ms. The wavelength was then set to sharply decreases to 0V over 0.9 ms and held for 3.7 ms.

In comparing the ANP jetting waveform to the synthetic PEDOT/PSS waveform, the overall voltage pulse width of the ANP waveform is shorter with a longer recovery stroke. Furthermore, the differences in these waveforms confirm that the chemical composition of each fluid ink dictates its ability to print. Amending parameters, such as the rate of voltage and frequency, are necessary for proper fluid printing, and we have found that these adjustable parameters directly affect the rate and indirectly affect the subsequent patterns.

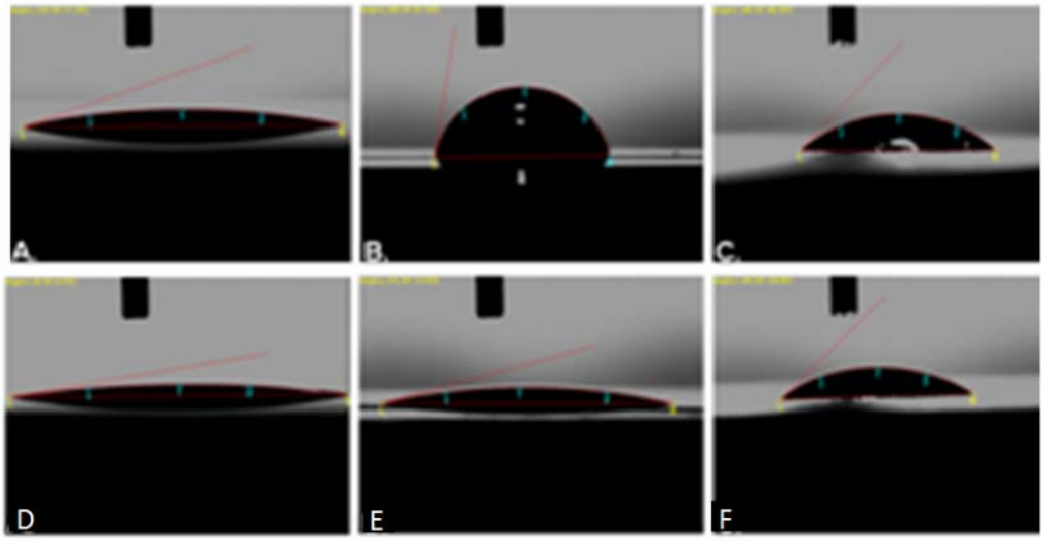

Figure 15. Contact angle measurements of PEDOT/PSS and ANP ink. Angles were measured on (A,D) Glass wafer, (B, E) Kapton® and (C, F) Teslin®, respectively.

Substrate/fluid contact angle

Physical measurements, such as contact angle, demonstrate the interplay between fluid development, printing, and substrate interactions.[121] In these studies, the contact angles of a drop of PEDOT/PSS ink and the ANP ink were measured independently, as an effect of varying substrates. The PEDOT/PSS ink was shown to spread on an untreated glass wafer with a contact angle of 18° (Figure 15a) but exhibited minimal spreading when the PEDOT/PSS was printed on Kapton® (81°, Figure 15b). Moderate spreading was observed when the PEDOT/PSS was sampled on Teslin®, (46.2°, Figure 15c). The contact angles were similarly determined for the ANP ink. inks. Despite having fluid properties similar to the PEDOT ink, ANP nanopaste spreads on the Kapton® substrate (14.9°), while PEDOT did not (80.95°). Furthermore, the ANP ink exhibited more spreading on the glass (9.5°) and Teslin® (40.2°) substrates (Figure 15 d-f).

Determining the contact angles for different substrates provides valuable information on the surface energy of a liquid. The obvious differences in the contact angles of the two inks is affected by the interplay between their relative composition.[121] From a materials perspective, a substrate can be characterized as a wettable surface, inducing low contact angles, or a non-wettable surface, inducing high contact angles. On the same token, if the surface energy of a substrate is high enough to overcome the surface tension of the ink, then wetting will occur. Using this rationale, the minimal spreading associated with the PEDOT/PSS ink can be directly related to its higher surface tension when compared to the ANP ink. An optimal substrate induces the highest contact angle because the available area for reactivity is highest.

Part II: Output Analysis of Materials Inkjet Printer

A key component for improved microarray utility is the reproducible delivery of material to an addressable spot location. In this section, the production of a number of different microarrays was investigated for three different functional composite inks. To quantify the average mass of one spot of printed material, a QCM was modified as a nanoscale balance. Results from these mass loading measurements clearly demonstrated the reproducibility of the DMP over time, ensuring this printer is highly reproducible for the rapid, small-scale fabrication of a variety of patterned microarrays.

The three inks employed in this output analysis included a multi-walled carbon nanotube (mwCNT) composite solution, a commercially available colloidal silver ink, and a monodispersed nanosphere solution. The surface tension of the mwCNT ink was measured as 33 dynes cm^{-1}. During the mwCNT printing cycles, the voltage of the nozzle

was maintained at 28 V, and the maximum frequency of the pulses was 1.0 KHz. The conjugated nanosphere solution was diluted in a glycol composite solution (1:1000), yielding a final surface tension was 36 dynes cm^{-1}. During the printing cycle, the voltage was maintained at 20 V, and the maximum frequency of the pulses was 2.0 KHz. The colloidal inkjet silver conductor was printed as received, with a measured surface tension of 31 dynes cm^{-1}. The voltage was maintained at 27 V. The maximum frequency used was 3.0 KHz. The pulse width was sustained at 3.6 µsec for each ink during these printing cycles.

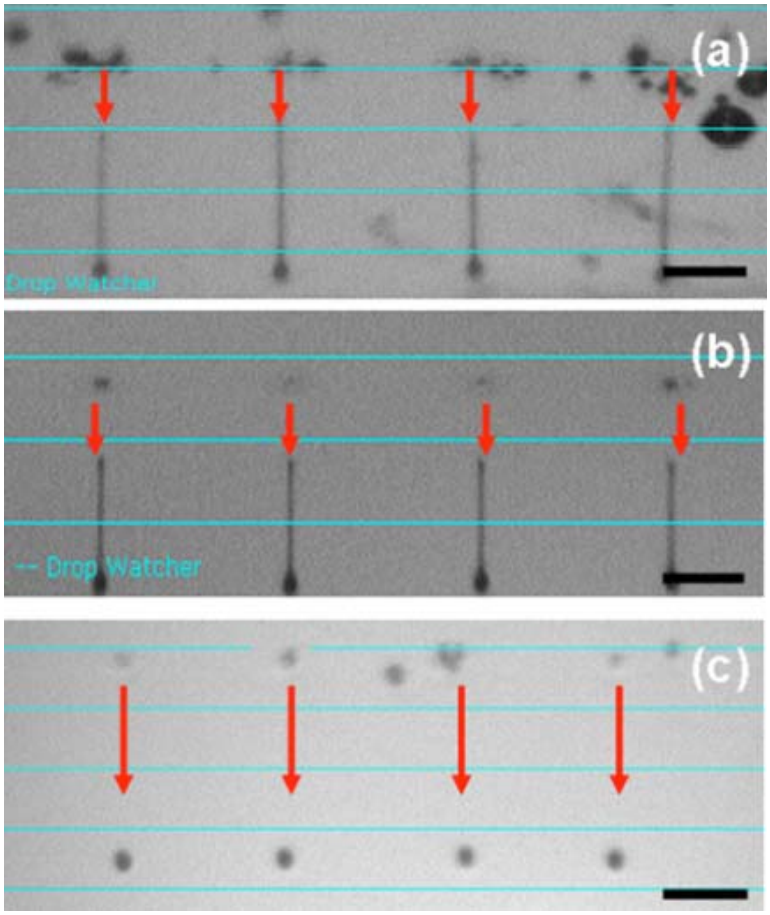

Figure 16. The TOF of printed spots. (A) mwCNT ink, (B) silver ink, and (C) microsphere inks using the 4 x stroboscopic view of 4 nozzles jetting at variable voltages. Scale bar represents 100 µm.

Time of flight (TOF) images were recorded, where the arrow highlights the path of the droplet from the nozzle to a substrate for each fluid (Figure 16). Once ejected, the drop assumes different physical characteristics, corresponding to the properties of the ink. However in all cases, when a droplet is released from a nozzle, a meniscus quickly extends until a spherical, bulbous edge is formed, until a new surface with a new surface energy is developed. [102, 114] Dong and coworkers have previously shown that these characteristics, recognized as a "tailing" effect, was related to an increased ink viscosity. The higher viscosity causes an increase in the intermolecular forces within a drop, producing a dampened velocity.[102, 114] In our study, all inks printed had similar viscosities (11.8, 14.4, and 14.3 mPa s for the mwCNT, silver nanoparticle, and nanosphere inks, respectively). The only variable factor was the constituent materials composing each ink. The more components in an ink yields a higher observed associated tailing effect, suggesting particle load mediated viscous effects.[114, 122] Thus, the mwCNT (0.989 g mL-1) and colloidal silver (1.38 g mL-1) multicomponent inks exhibit tailing due to the increase in the amount of material per unit volume, while the polystyrene nanosphere ink (0.297 g mL-1) does not (Figure 17c).

Despite the documented tailing phenomena, it has been shown that the increasing pressure from the tail causes the liquid to recoil into a sphere, reducing the surface energy prior to immobilization.[102] Consequently, it is predicted that the final spot architecture is independent of the tailing effect and dependent on the contact angle of the substrate fluid interaction and particle mobility upon surface interaction.[112] In an attempt to model the fluid flow dynamics of each ink, Z values for the individual inks were calculated using the equation specified by Reis and Derby (Eqn 4).

$$Z = (d\rho\gamma)^{1/2} / \eta = Oh^{-1} \quad (4)$$

In this equation, drop formation was modeled as a dimensionless parameter, *Z*, an equivalent to the inverse Ohnesorge number (Oh), where d represents the diameter of the printhead nozzle, and η, ρ, and γ represent the viscosity, density, and surface tension of the liquid, respectively.[110] Z values were calculated as 1.1, 2.4, and 2.1 for the nanospheres, mwCNTs, and Ag inks, respectively. Typically Z values less than two indicate *jettable* inks, and Z values greater than two infer a more complex ink. In our studies, the nansophere ink ($Z < 2$), exhibits no tailing; whereas, the more complex mwCNT and Ag inks ($Z > 2$), exhibit tailing. For this reason, it is believed that modeling the properties of the ink prior to printing using the Z-analysis will specify whether the ink will demonstrate tailing during printing. Typically, an increased Z value is also related to an increased drop volume; however, the complexities of each ink, including the variations in densities, solvents, and particle load, precluded any meaningful correlation.

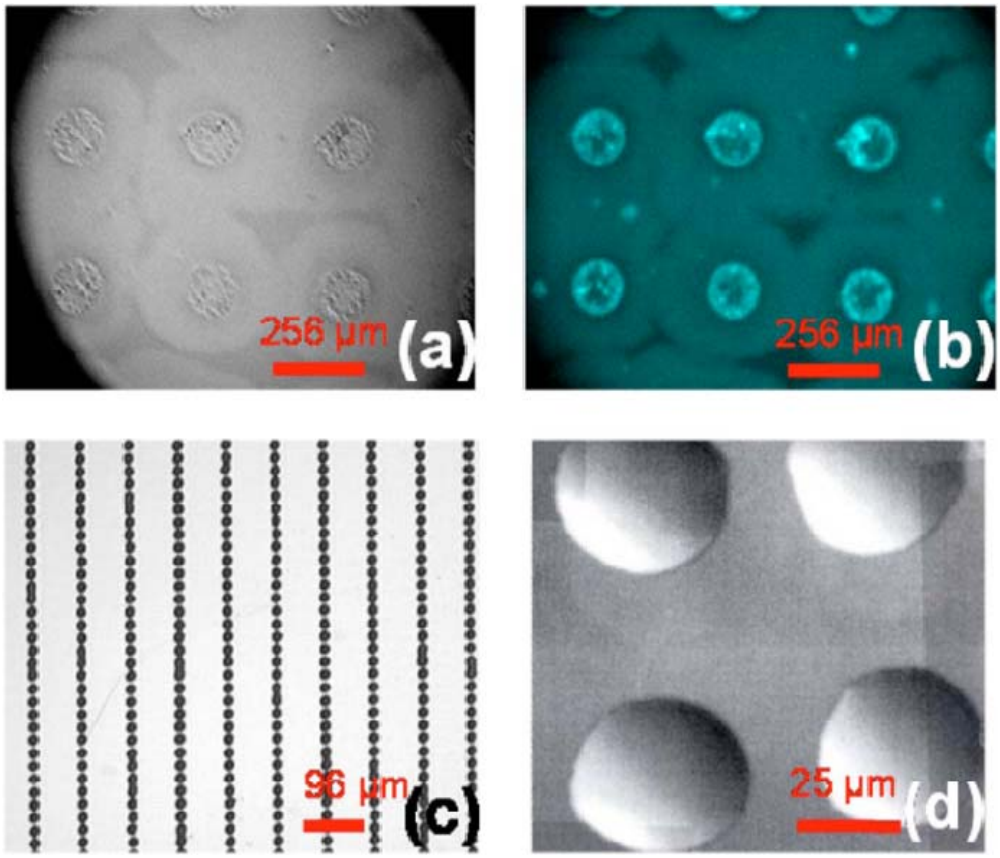

Figure 17. 10 x magnification of patterns. (A) DIC image, (B) DAPI image of mwCNT arrays, spaced 256 µm. (C) Bright field silver spot arrays, pre-curing, spaced 56 µm. 20 x magnification (D) DIC image of microsphere array, spaced 96 µm.

To further investigate the properties of the printed inks, a series of microscopy analyses were investigated. Ideally, the drop sizes of each material should correspond directly with their contact angles. Contact angles of 13.1°, 41.8°, and 11.8° were recorded for the nanosphere, silver, and mwCNT inks, respectively. The angle between the drop and substrate was determined by VCA Optima XE software. Bright field and fluorescing images were subsequently used to document the average spot size of five consecutive spots on non-functionalized glass substrates. The spot diameters for nanosphere, silver, and mwCNT composite inks were 51 ± 4 µm, (Figure 17d), 40 ± 2 µm, (Figure 17c), and

98 ± 5 μm, (Figure 17a-b), respectively. The larger contact angle reported for the silver ink corresponds with its smaller spot diameter. The smaller angles associated with the nanospheres and mwCNTs, however, showed no correlation to their respective spot diameters. Consequently, the reproducibility of composite ink delivery during a print cycle was examined on the nanoscale using the QCM to directly determine the relative mass of each spot, a property independent of the inks' composition.

Six arrays (spaced 256 μm apart) were printed and analyzed in triplicate for each ink. It was shown that the QCM provided reproducible mass measurements on the nanoscale, despite the ink printed (Figure 18a-c). The mwCNT ink was printed at an average mass of 2.9 ± 0.6 ng/spot (Figure 18a). The theoretical mass delivered to the QCM crystal, approximated using the diameter of the drop from the TOF, was 3.08 ± 0.01 ng/spot. The difference between the approximated mass at the point of jetting compared to that on a surface was due to either liquid evaporation during the time of flight or the resolution limits of the TOF image. The average volume (2.9 ± 0.6 pL) of one drop was extrapolated from the average mass and the known density of the solution (0.989 g ml-1).

The colloidal silver ink, composed of silver nanoparticles in a nonaqueous liquid, was printed and studied as received. The average mass of one spot (1.8 ± 0.5 ng) (Figure 18b) was similarly calculated and used in conjunction with its density (1.28 g mL-1), to determine the average volume of one drop (1.4 ± 0.4 pL). Again, the actual mass of the deposited silver was compared to the approximated jetted mass (1.07 ± 0.02 ng/spot) with good agreement.

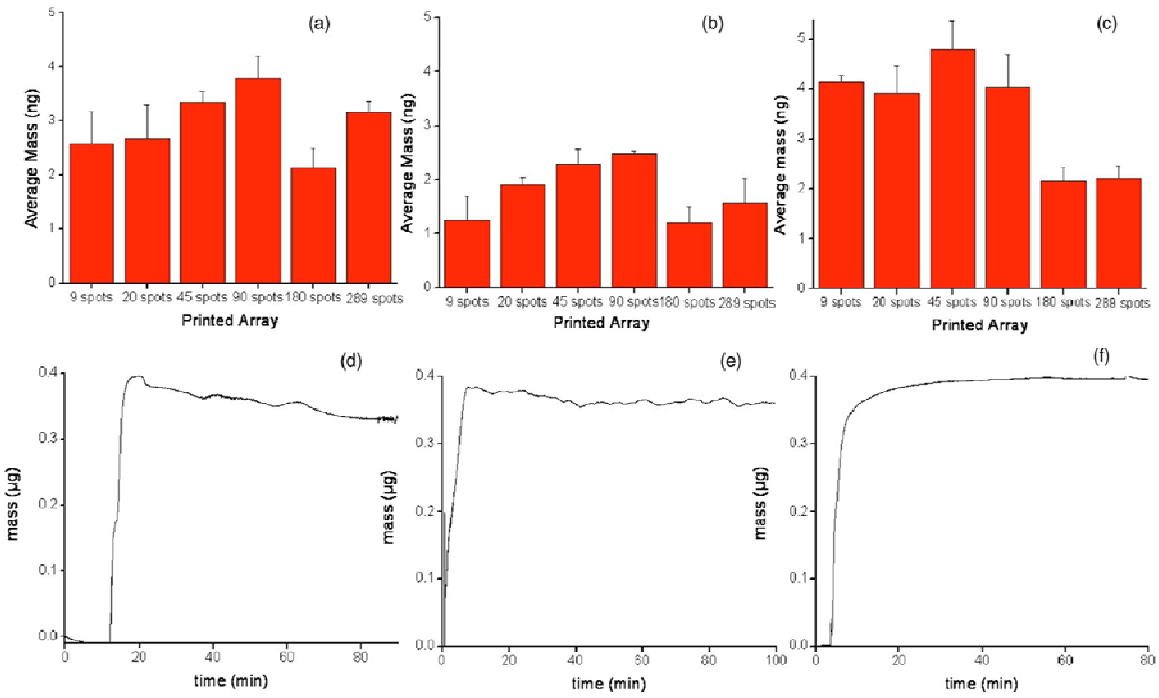

Figure 18. The average weight of one detectable drop. (A) 0.989 g mL-1 mwCNT composite ink, (B) 1.285 g mL-1 silver collodial solution, and (C) 0.297 g mL-1 microsphere solution. The mass loading of (D) 180 drops of the mwCNT solution over 90 min (E) 180 drops of the silver ink over 100 min, and (F) 180 drops of microspheres over 80 min.

The third solution studied was a composite ink solution of concentrated fluorescing nanospheres (Figure 18c). The average mass of one spot was calculated as 3.5 ± 0.9 ng, and the corresponding volume was extrapolated from the density (0.297 g mL-1) to be 12 ± 3 pL. By comparison, the mass released from the printhead was approximated to be 4.19 ± 0.01 ng/spot.

The volume of the nanosphere droplets, which is nearly 6x larger than the other two inks, may be related to its decreased density, which is approximately one fifth of the other two inks studied. To investigate the physical behavior of the increased drop volumes on a surface, a time-resolved, mass loading study was performed using the

QCM. This study aimed to document the drying behavior of the printed film over a period of time under ambient conditions. In each trial, 180 spot arrays of each ink were deposited, and the mass loading was recorded over time (Figure 18d-f). The variability in experimental noise between the three runs is associated directly to the electrical variability of the instrument and is considered statistically insignificant in the context of our experiments. At room temperature, minimal to no evaporation was observed for the silver and the nanosphere inks (Figure 18e-f), while moderate evaporation (5.13 pg min-1) was detected for the mwCNT ink (Figure 18d). This suggests a more complex solvation behavior in the multicomponent mwCNT ink resulting in its higher volatility. Future experiments will be aimed at a more in depth approach towards fluid analysis, focusing specifically on identifying the sources responsible for pattern variability.

Electrical properties

Once printed, the films were annealed to convert the nanoparticles to a bulk silver thin film, so that the resistance values of the final feature sizes can closely mimic bulk silver. At high annealing temperatures, the porosity of the final material is altered because the organic additives in the ink begin to decompose into the gas phase, affecting the continuity of the film.[116] Low-temperature annealing (200°C for 1 h), however, has produced traceable conductivities within the printed film on an insulating glass substrate. The resistance of the ANP ink was measured as 1.1Ω (Figure 19a), and the resistance of the Cabot Inkjet Silver Conductor was 0.3 Ω (Figure 19b). The low resistance measurements in both cases were taken on equally-sized patterns on identical glass

wafers. These values are in the same range as resistance values reported elsewhere, confirming that the activity of the printed patterns are comparable to the bulk.[123]

Figure19. Resistance values for silver inks. (A) ANP silverjet nanopaste and (B) Cabot silver paste.

Conclusion

The DMP possesses the necessary features to make inkjet printing of materials a cost-effective manufacturing process. The software interface and waveform tuning features associated with the DMP make it an ideal R&D tool. The printing parameters and the output analysis of the DMP were demonstrated using single spot microarrays of five composite inks printed onto Au-coated quartz crystals or SiN_3 substrates in air. First, the operating parameters for two conducting inks were demonstrated, where the interplay between the chemical properties of the fluid, the cartridge assembly, the machine operating procedure, the substrate, and the post-inkjet processing were studied. Then, the printing parameters of three biomaterial inks were investigated, where the average weight of one spot of each material was determined directly using a QCM. The calculated weight was used in conjunction with density to estimate the average volume of a single spot of each deposited material. It was shown that inkjet printing reproducibly formed sub-15 pL

spots, suggesting this deposition method to be highly reproducible for rapid, small-scale fabrication of microarrays.

CHAPTER III

PIEZOELECTRIC INKJET PRINTING OF BIOMIMETIC INKS FOR FUNCTIONAL REACTIVE SURFACES

Introduction

The intricacies involved in the formation of nanostructured cell walls of marine diatoms have been a source of inspiration for a generation of developmental biologists, chemists, and material scientists. It is understood that the biomineralization of the cell wall is initiated on the surface of an internal valve known as the silica deposition vesicle (SDV).[14, 53, 124, 125] The SDV provides a localized environment where cell wall biogenesis is completed as silica condensation is catalyzed by long-chain polyamine moieties or cationic polyeptides.[14, 53, 124, 125]A number of biomimetic analogs to the silica precipitating peptides have been developed and characterized *in vitro*.[69, 71, 126-129] Although they are recognized as excellent examples of bio-inspired templates for metal oxide synthesis, these mimics have yet to successfully recapitulate spatial and supramolecular control on a two-dimensional surface.

Recent materials deposition techniques including solenoid jet printing, lithography and liftoff patterning, and direct ink write (DIW), have been used to immobilize a variety of silica precipitating precursors.[77, 126, 130] All methods provided a unique approach towards the advancement of controllable templating for patterned metal oxides; however, each was beset by their own limitations. These included large, non-uniform spots (solenoid jet printing), high temperature reaction conditions (lithography and liftoff), or

inherently slow (40 μm s^{-1}) patterning conditions (DIW), rendering them unfavorable for the rapid production of functional material patterns under ambient conditions.[77, 126, 130] For these reasons, we have employed piezoelectric inkjet printing with the Dimatix Materials Printer (DMP) as an alternative, rapid prototyping (8 m s^{-1}) method of deposition for the two-dimensional (2-D) patterning of templated micro-structured silica. The flexibility associated with DMP deposition provided reproducible spot sizes and enabled tunable surface control, specific for each reaction environment.

Design and development of reactive functional surfaces

One essential characteristic of bioanalytical systems is their ability to rapidly detect a panel of drugs, pathogens, or biomolecules from selectively functionalized surfaces. From point of care (POC) diagnostics to electrochemical sensing, localized areas of biologically active films serve to support and to protect the functional material, while offering higher sensitivity and increased resolution during analysis.[131-134] With the advent of recent, low temperature microscale deposition techniques such as direct ink writing (DIW), screen-printing, or ink-jet printing (IJP), there has been considerable interest in modifying solid surfaces with and biologically active functional materials. Because of the unpredictable nature of chemically responsive surfaces, balancing the interplay between the spatio-temporal relationship associated with patterned materials still remains an obstacle for sustainable adaption.[135] Moreover, real-time analyses of reaction products have yet to be adapted to films or coatings.[136]

While the structure and property relationships of 2D-active surfaces are not well understood, solution phase bio-compatible systems have been studied extensively.[62, 136,

[137] Previously, biomimetic enzyme-containing silica nanoparticles have been synthesized, yielding localized nano-environments for the soluble enzyme. When compared to non-encapsulated systems, enzyme activity was not significantly hindered during the silica encapsulation phase; instead, these hybrid systems introduce multi-use capabilities and enhanced enzymatic life spans, as well as simpler and cheaper product separation and purification strategies.[62, 136-138] For these biomaterial systems, the lifespan of the catalyst and consequently its overall product turnover outweighs any loss in activity caused by immobilization.

Previously, glucose oxidase (GO_x) has been encased within a silica matrix through either sol-gel or biomimetic encapsulation strategies.[134, 139-144] When compared to traditional sol-gel methods, the biomimetic encapsulation of GO_x was reported to be much faster under milder reaction conditions (30 min compared to 32 h for sol-gel formation).[140, 143, 144] In particular, a bio-inspired, amine-terminated PAMAM dendrimer template has been shown to direct the encapsulation of enzymes within silica nanospheres with high loading efficiency and excellent long term stability.[137] When placed in a low ionic strength environment, GO_x's acidic p*I* has a complimentary charge to the amine terminated PAMAM dendrimer, encouraging the formation of a supramolecular complex necessary for silica polymerization and subsequent condensation. These particles also maintained activity within one-fold of the soluble enzyme when tested under similar conditions. Due to its robustness, GO_x is an excellent model enzyme for use in a functionalized biocompatible surface.

Experimental

Dendrimer Printing

A solution of 8.6 wt% dendrimer with 25 % w/v polyethylene glycol (PEG, Aldrich Chemical Co.) was printed, and the voltage was maintained at 18.4 V. PAMAM dendrimer (G4) (Dendritech, Inc.) and tetramethyl orthosilicate (TMOS) (Aldrich Chemical Co.) were both used in this study.

Silica Precipitation Assay

The silica precipitation assay was based on a variety of literature procedures.[80, 95, 145] The dendrimer ink was printed onto an R-plane sapphire (Al_2O_3) substrate, purchased from Materials Tech. Intl. (Richmond, CA). The printed samples were glued to a standard glass pipette and left to dry overnight. After this time, the sample was inverted and submerged in a 113 mM solution of silicic acid diluted in phosphate buffer (pH 7.5) for 20 min. The condensed silica was quantitated using the β-silica molybdate method.[146] Reacted substrates were purified using a 5000 molecular weight cutoff device (Amicon Centricon filtration devices). Once filtered, 0.5 mL of the remaining supernatant was added to the molybdate reagent in a 1:4 ratio (silicic acid/ molybdate), which initiated the formation of a bright yellow product monitored by UV-vis spectrophotometry (Agilent Technologies model 8453 UV-vis) at 410 nm and quantitated using a previously determined silicate standard curve. [147]

Fluorescence Imaging

All images were captured using an Axiovert 200 inverted microscope. The ink was printed onto a functionalized, spin-coated glass slide (100 μL of hexadimethylsiloxane, Acros Organics) was also exposed to an amine specific dye, AlexaFlour 488 (Tetrafluorophenyl ester, Molecular Probes). All functionalized samples were washed with excess deionized water and dried with N_2 gas to limit any nonspecific binding. The resultant green fluorescence (ex. 350 nm/ em. 525 nm) was collected using a HQ 535/50 filter set (Chroma Tech. Corp.). Samples were further functionalized with the fluorophore 2-(4-pyridyl)-5-((4-(2-dimethylaminoethylaminocarbamoyl)-methoxy)-phenyl)oxazole (PDMPO) (338nm ex./510 nm em, Lysosensor DND-160 yellow/blue, Molecular Probes) collected using a long pass 450 filter set (Chroma Tech.Corp.) Again, reacted samples were washed deionized water and dried with N_2 gas prior to imaging.

Glucose Oxidase (GO_x) Silica Encapsulation on Gold

Method I: A gold substrate containing the printed dendrimer ink was inverted and lowered into a solution containing 500 mL of 0.1 mg/mL GOx (in 0.25 mM phosphate buffer pH 7.0) and incubated for 10 minutes. Next, 50 mL of 1 M silicic acid was added and the reaction was allowed to react for varied times (5-20 min). The reaction was terminated by removing the substrate from the reaction solution and washing it copiously with water. The substrates were then dried under a gentile stream of N2. Controls were also prepared with the same method, except the reaction solution didn't contain any GOx.

Method II: Instead of allowing for interaction between the printed spot and GOx, the printed substrate was inverted and lowered into a solution containing 500 mL of 0.1 mg/mL GOX (in 0.25 mM phosphate buffer pH 7.0) and 50 mL of 1 M silicic acid. Upon

addition, the reaction was allowed to proceed for 20 min. The reaction was similarly terminated by removing the substrate, washed with water, and dried with N2. Controls without GOx were also prepared using the same method.

Glucose Oxidase (GO_x) Encapsulation in 96-well Plates

Method I: A 200 mL solution of GOx in 0.25 mM phosphate buffer pH 7.0 was added to each printed well and allowed to incubate for 10 minutes. Next, 20 mL of 1 M silicic acid was added and the reaction was allowed to proceed for 20 minutes. The reaction was terminated upon centrifugation at 3000k for five minutes and the supernatant was removed. The wells were then washed three-fold with 200 mL of 0.1 M phosphate buffer pH 6.0 to remove any unused reactants.

Method II: A solution containing 200 mL of GOx in 0.25 mM phosphate buffer pH 7.0 and 20 mL of 1 M silicic acid was added to each printed well and allowed to react for 20 minutes. The reaction was terminated upon centrifugation at 3000k for five minutes and the supernatant was removed. The wells were then washed three-fold with 200 mL of 0.1 M phosphate buffer pH 6.0 to remove any unused reactants.

Glucose Oxidase Activity

Activity of the encapsulated enzyme was determined by the glucose oxidase activity assay (Worthington Biochemical Corporation) with slight modifications. First, an O-dianisidine dye reagent was prepared by adding 100 mL of 1% O-dianisidine solution to 12 mL of 0.1M potassium buffer at pH 6. After purging this solution with oxygen for at least 10 minutes, an aliquot of 192 μL was added to a solution containing 25 μL of β-D-

glucose (concentrations of glucose reflect consideration of mutarotation in solution) and 8.35 μL of a 0.2 mg/mL solution of horseradish peroxidase (HRP). Next, this solution was added to a 25 mL solution of appropriately diluted GOx in H2O or added to the printed wells containing 25 mL of water, and the change in color was observed for 5 min at 460 nm. Reusability of the wells was assayed by reacting for 5 min and then washing 3 times with buffer before reuse. The reaction was repeated a total of 10 times. Storage stability of the printed wells was assayed after storage in 0.1 M phosphate buffer for multiple days.

Profilometry

Height profiles of the printed composite for each reaction condition were analyzed using a VEECO profilometer with a 12.5 μm stylus. The scan rate was 10 mm/sec and the stylus was maintained at 3.00 mg during each scan.

Scanning Electron Microscopy

Scanning electron microscopy (SEM) was conducted using a Hitachi S4200 microscope operating at variable voltages. Samples were prepared by sputter-coating them with a thin layer of gold using a Pelco Model 3 Sputter Instrument (Ted Pella Inc.) to prevent substrate charging during analysis.

Results and Discussion

Ink Development and Characterization

A composite ink was developed with a viscosity of 18.5 mPa and was printed onto gold, glass, or sapphire substrates. The components of this ink included 8.6 wt % generation 4 (G4) PAMAM dendrimer in polyethylene glycol (PEG) (25% w/v), and phosphate buffer (100mM, pH 7.5). The PAMAM dendrimer was used as the defined silica condensing template as its primary amine moieties are effective mimics of the propyleneamine units found in silica precipitating peptides.[124] These dendrimer templates have been shown to rapidly precipitate aggregated nanospheres of silica *in vitro* at neutral pH.[147-149] To investigate the interfacial properties of the composite ink on a gold substrate, the contact angle of a 2 μL sample was determined to be 33.10°. This low contact angle (< 90°) indicates that the localized stability and confined rheological properties of the immobilized ink are loosely packed on the high energy, hydrophobic substrate.[112] The addition of PEG in the ionic ink produces an aqueous composite system that complements its intrinsic self aggregation.[150] This enhanced aggregation is necessary to keep the printed spots discrete on the surface as evidenced by both the viscosity and the contact angle of the ink without PEG (9.7 mPa and 16.46°, respectively).

Once the customized ink has been developed, it was loaded into the print cartridge, where a specific voltage is applied to each nozzle of the printhead, releasing a droplet on the order of 10 pL.[80] Because the DMP is a piezoelectric instrument, a user-controlled, pulsed voltage induces an internal stress in the form of a pressure wave inside the nozzle of the printhead (16 nozzles total, spaced 256 μm apart).[80, 95] In these studies, the

maximum voltage pulse was 24 V, and the frequency of the pulses was maintained at 1.0 kHz, ensuring that the same amount of material was deposited during each print cycle. The printed spot sizes were constant and independent of the substrate at 36 ± 2 μm. Additional properties of the patterned dendrimer were characterized using UV-vis spectrophotometry, scanning electron microscopy (SEM), and fluorescence microscopy. Varying the spot spacing, the number of print cycles, and the reaction time with monosilicic acid resulted in silicified structures reminiscent of patterned silica on the cell wall of diatoms.

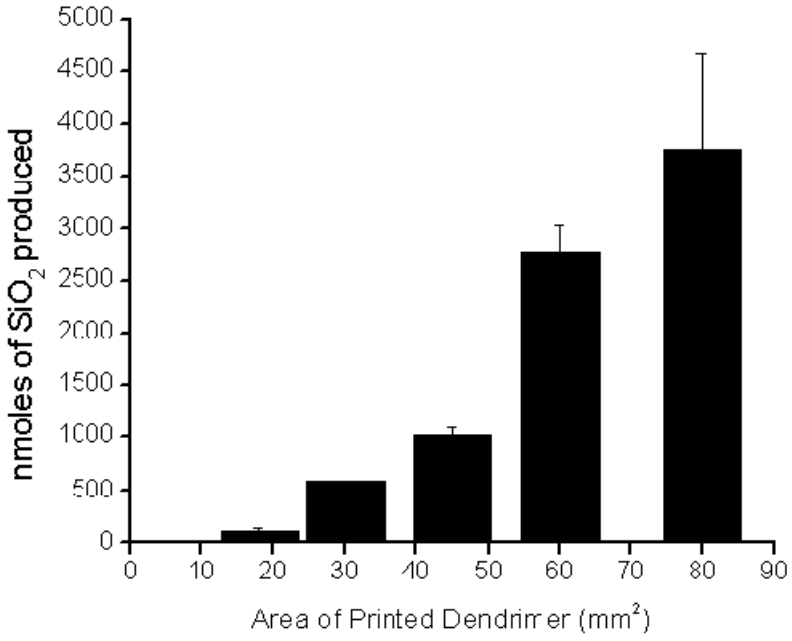

Figure 20. SiO_2 quantification as a function of the area of printed dendrimer. All reactions were done in triplicate. Patterns were printed eight consecutive times (spaced at 46 μm) onto sapphire substrates, reacted with monosilicic acid for 15 min, and assayed for SiO_2 production. The amount (nmoles) of SiO_2 produced was quantitated using a modified silicomolybdate assay.

The reactivity of the dendrimer ink was studied with the specific aim of controlling the formation of patterned silica on a solid surface. For this reason, initial experiments were aimed at characterizing the silica precipitating reactivity of the dendrimer patterns (Figure 20). Samples were prepared varying only the area of patterned dendrimer (printed eight times with a 46 μm spot spacing) on an R-plane sapphire substrate. Each pattern was then reacted with a monosilicic acid solution (113 mM in phosphate buffer, pH 7.5) for 15 min. The multiple print cycles over larger areas were necessary to produce highly reactive multilayer films, increasing the quantity of accessible surface amines. Arrington and coworkers have used micro-contact printing in conjunction with atomic force microscopy to show that repetitive dendrimer stamping increases the amount of deposited dendrimer in the form of 3-D frameworks of cross-linked amines in air.[151, 152] This cross-linking enables the amines to act as an adhesive layer on a substrate while providing a highly functionalized surface essential for silica precipitation. As the area of printed dendrimer is increased, the corresponding amount of precipitated silica increases (Figure 1). Silica was quantitated using a modified *β*-silicomolybdate assay against a previously determined silicate standard curve.[125, 147, 153] Under these reaction conditions, the area of detectable silica ranged from an 18 mm^2 printed area (110 ± 20 nmole silica) to 80 mm^2 (3700 ± 900 nmole silica) (Figure 20).

Fluorescence labeling of the dendrimer ink was used to identify the specificity and selectivity of silica along the printed dendrimer patterns. In these studies, the dendrimer ink was reacted with an amine specific dye (AlexaFlour 488-TFP. 1:1000) for 3 hours prior to use. The resulting construct allowed for the effective imaging of the spatial placement of the reactive ink (Figure 21). During each print cycle, only the spacing from

the center of one spot to the center of another was varied. At 64μm spacing, the spots remain discrete on the substrate (Figure 21a-b). A decreased spot spacing (56 μm, Figure 2c-d) induced coalescence as the onset of electrostatic interactions between the spots increased. If the spacing is varied during the same print cycle (from 64 μm to 96 μm), the dendrimer spots respond accordingly, minimizing the available surface area of the spots,[154] while assembling into secondary patterns of triangles, lines, and circles that remain symmetric over a 16 mm^2 printed area (Figure 21e-f). Control experiments without the PEG component of the ink yield similar patterns that were less discrete and uniform, inferring yet again that PEG is necessary but not an essential component in the packing behavior of the dendrimer patterns.

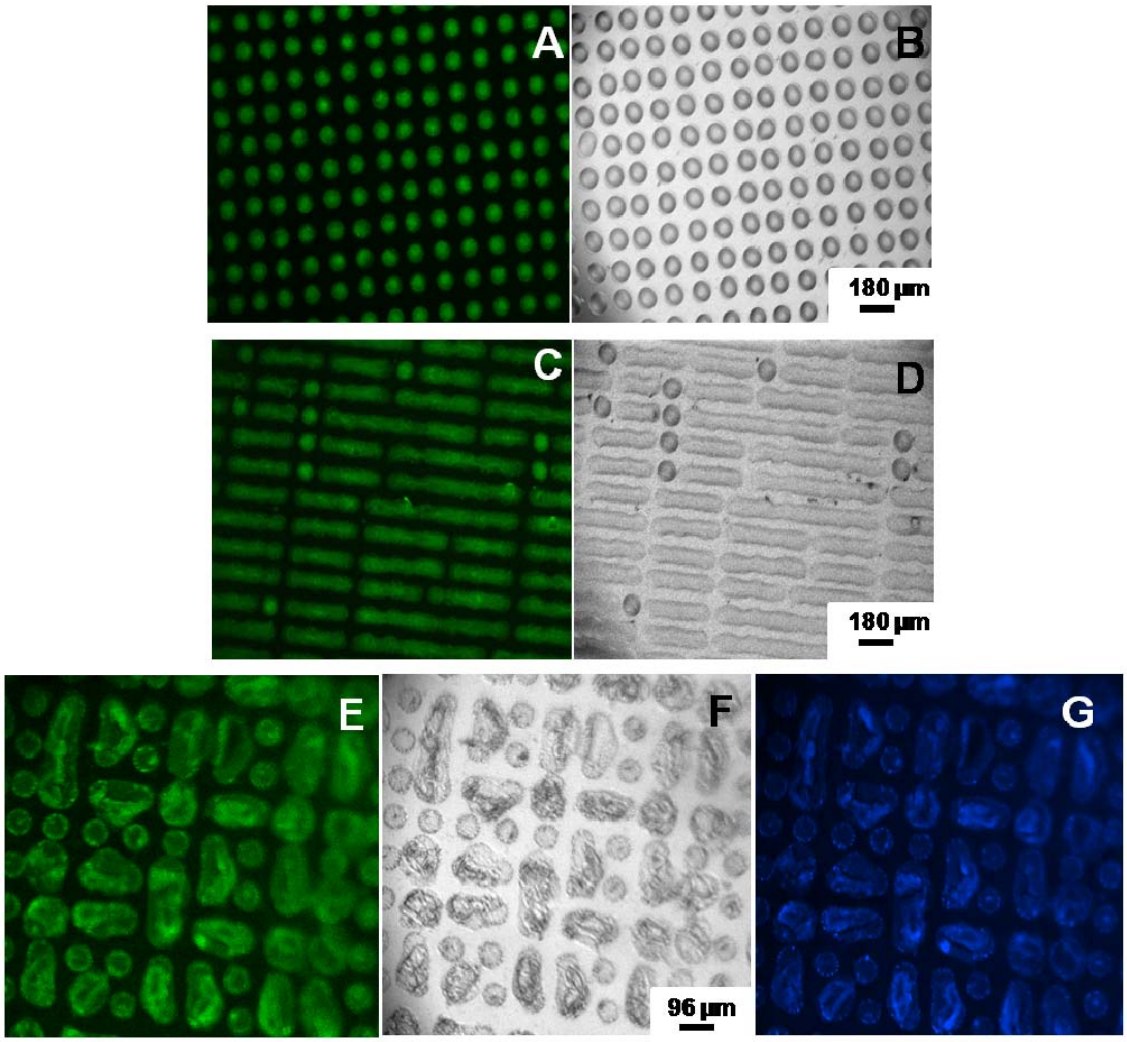

Figure 21. Fluorescence labeled dendrimer ink printed on glass with variable spot spacings. Fluorescence was captured using appropriate filter sets (A, C, E, G). Bright field images were captured using DIC mode (B, D, F). All samples were washed with de-ionized water and dried with N_2 gas prior to imaging. (A-B) 2 print cycles, 64µm spot spacing, (C-D) 2 print cycles, 56 µm spot spacing, (E-G) 64µm spot spacing during first print cycle followed by 96 µm spot spacing for the second print cycle.

In his theory of cell wall morphogenesis, Sumper suggested that the formation of secondary patterns, as seen on the diatom cell wall, is related to the wall-to-wall distance of the areolae, hexagonally packed polyamine monolayers, on the surface of the SDV.[14] Once placed in close proximity to each other on the heterogeneous surface, the packed

monolayers assemble into lowest energy conformations that remain stable, regardless of its ultimate silicic acid uptake.[14] Incorporating these ideas to obtain more realistic control over the reactive surface, the developing patterns were incubated with monosilicic acid and 20 μM of 2-(4-pyridyl)-5-((4-(2-dimethylaminoethyl-aminocarbamoyl)methoxy) phenyl)oxazole (PDMPO), a silica specific dye, for 20 min.[24] PDMPO is an acidotropic probe that produces a bright blue fluorescence, indicating its incorporation and accumulation within the acidic silica condensate (338 nm ex/510 nm em).[155] The reacted patterns were washed with DI-water, dried under a steady stream of N_2 gas, and examined under the microscope. The corresponding image verified the specific correlation between the localized silica fluorescence and the dendrimer patterns, indicating that the spot spacing is directly responsible for the outcome of a particular micropattern (Figure 21c-d).

The nanoscale reactivity of a printed spot of dendrimer (printed four times, 96 μm spacing) was probed using electron microscopy as a function of the temporal development of silica (Figure 22). Unlike its *in vitro* counterpart that occurs within seconds,[147] the *in vivo* reaction between the patterned dendrimer and monosilicic acid did not form spontaneous nanospheres, suggesting that the 2D activity of the printed dendrimer is retarded by its heterogeneous composition. As it reacted with monosilicic acid at early time points, the thermodynamically stable spot became disrupted, indicating a pseudo dewetting phenomena (Figure 22, 1 and 3 min).[156] True dewetting and pseudo dewetting are both a direct result of localized instability of a heterogeneous film under an induced density fluctuation.[156] The former results in a dry spot, and the latter produces a metastable adsorbed film, which is observed in our developing patterns (Figure 3, 1-3

min).[156, 157] This metastable environment, also understood as the contact-line pinning effect, can be likened to the glossy liquid precipitate, or *coarcervate,* described in documented *in vitro* silica condensation reactions.[56, 122, 156, 158] The *coarcervate* is described as a stabilized sol wherein the polyamine template and silicic acid have interacted preventing the formation of nanospheres and has also been predicted to be the source of the hardened framework of the silica shell of the diatom.[56] The pinned-contact line forms as the evaporated liquid at the edge of a spot is replenished by the dispersed liquid from the spot's interior;[158] furthermore, it appears that the onset of contact-line pinning was essential to expose free surface amines for silica production, as nanospherical silica is seen for the first time along the periphery of the spot at 5 min (Figure 22).

As the reaction time is increased, silica precipitation begins to expand, originating at the pinned contact line (Figure 22, 10 min). Amorphous silica nanospheres grow inward, loosely aggregating to form a heterogenous, top plate encasing the dendrimer spot (Figure 22, 15-20 min). Subsequently, the reactive dendrimer film undergoes a third transition, resulting in the collapse of the silica film between 20-25 minutes. The nanoparticles form colonies of silica along the pinned contact lines (Figure 22, 25 min). Eventually, the continued accumulation of aggregated, localized silica around the spot, yields the final structures (30 min). Examinations of time points beyond 30 min were not possible due to non-specific gelation of the aqueous monosilicic acid under these reaction conditions.

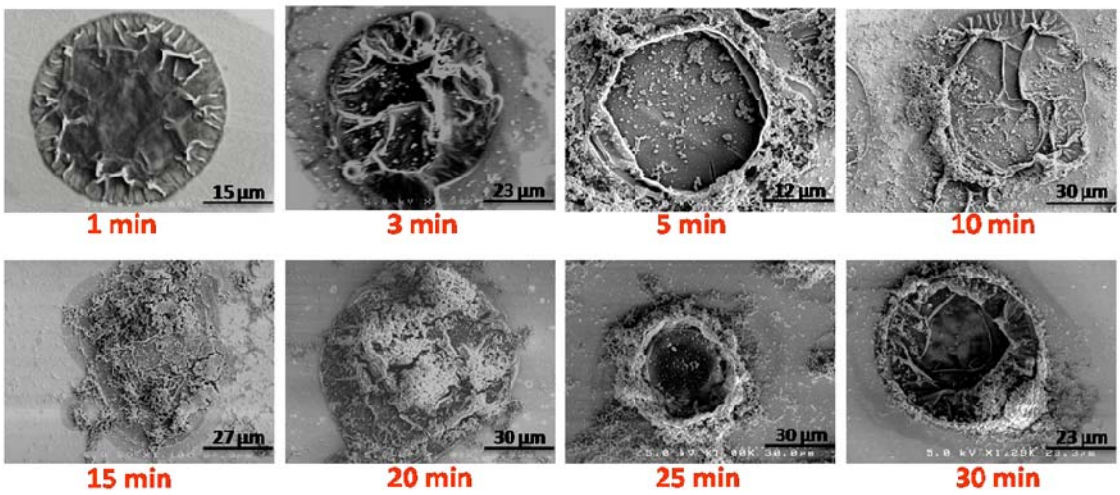

Figure 22. SEM images of dendrimer patterns. Printed four consequetive times (96 µm spot spacing on Au coated SiN_3 substrates) and reacted with monosilicic acid as a function of time. Samples were washed five times with de-ionized water to remove any unreacted monosilic, dried under a stream of N_2 gas, and sputter coated with a thin layer of gold for 25 sec (Pelco model 3 sputtering instrument) prior to imaging.

Similar to its *in vitro* counterpart, the *in vivo* dendrimer mediated silica condensation reaction suggests three distinct phases over defined time-points: nucleation, which initiates the phase change on the spot (1-3 min); nanospherical precipitation, which is seen only after the onset of contact pin line effect (5-20 min); and aggregation of the nanoparticles around the exterior of the spot (25-30 min). The physical interpretation of the evolving dendrimer patterns offers a unique perspective for the development of biologically relevant, reactive mesoporous materials. By controlling the length of reaction time with silicic acid, the spot spacing, and the number of print cycles, this highly reactive 2D could serve as the basis for future functionalized surfaces.

Bottom-up synthesis of biologically active multilayer films using biomimetic templates

Currently, the dynamic nature of biocompatible surfaces has yet to be explored in the context of inkjet printing. For this reason, the overall efficacy of confining GO_x to a patterned microenvironment was tested using inkjet printed templates. Combining the versatility of the DMP with a the reactivity associated with our developed biomimetic ink,[159] a platform has been developed for the efficient, bottom-up encapsulation of GO_x. Initially, the impact of the microstructure of a spot interfaced with GO_x and $Si(OH)_4$ was studied from a materials perspective. Because the reaction order and the concentration of reactive species are predicted to affect the physical unity of a spot, two methods of enzyme encapsulation were studied as a function of time and method using SEM analysis. In each method, a 24 mm^2 area of the dendrimer ink (printed 2x with 96 μm spot spacing) was patterned onto gold coated silicon nitride chips. Once printed, the patterns were subjected to multicomposite encapsulation using two independent methods. The first applied method (Method I) incorporated a step-wise approach to encapsulate quantifiable amounts of GO_x. In this approach, the patterns on gold were inverted and lowered into a 0.1 mg mL^{-1} solution of GO_x (in 0.25 mM phosphate buffer pH 7.0) and incubated for 10 minutes. After incubation, 50 μL of 1M monosilicic acid was added to the solution to yield an overall reaction concentration of 0.1 M without directly disturbing the chip. The reaction time of the chip with monosilicic acid was varied, and the subsequent patterns were imaged using SEM (Figure 23a).

Because of the nature of this encapsulation, it is anticipated that the enzyme would first electrostatically adhere to the surface of the printed spot, thus creating a locally high concentration of enzyme before monosilicic acid was added. However, it was quickly

determined that the morphology of a spot was severely disrupted upon addition of monosilicic acid. To determine the cause of this drastic morphology change, control experiments were conducted in which the spots were incubated in a reaction solution without any enzyme. Under the control conditions, spot morphology is maintained throughout the reaction period. Height profiling of the control patterns without enzyme revealed a near constant peak height (3.5 + 0.5 um, Figure 24a), and SEM analysis showed a similar morphology throughout the reaction period (Figure 23b). Compared to these controls, the shape and composition of the enzyme-impacted spots are severely altered after 5 minutes of incubation with monosilicic acid, suggesting that GO_x interacts aggressively with the dendrimer on the spot surface during the pre-incubation period. As a result, the spot surface is disrupted, thus allowing its contents, including the dendrimer-enzyme supraggregate to diffuse into the reaction solution. When monosilicic is then added, observable silica is precipitated along the fragments of the spot, maintaining a similar peak height at 5 min of incubation time (2.6 ± 0.9 μm), before nearly half of original height is lost (1.2 ± 0.5 μm, Figure 24a).

As an alternative to Method I, Method II was introduced, which utilized a one-pot synthesis approach. The enzyme concentration introduced for both methods remained constant; however, the pre-incubation step was not used in Method II. Instead, the printed chip was reacted simultaneously with GO_x and monosilicic acid and monitored by SEM and profiliometry at different time points (Figure 25a).

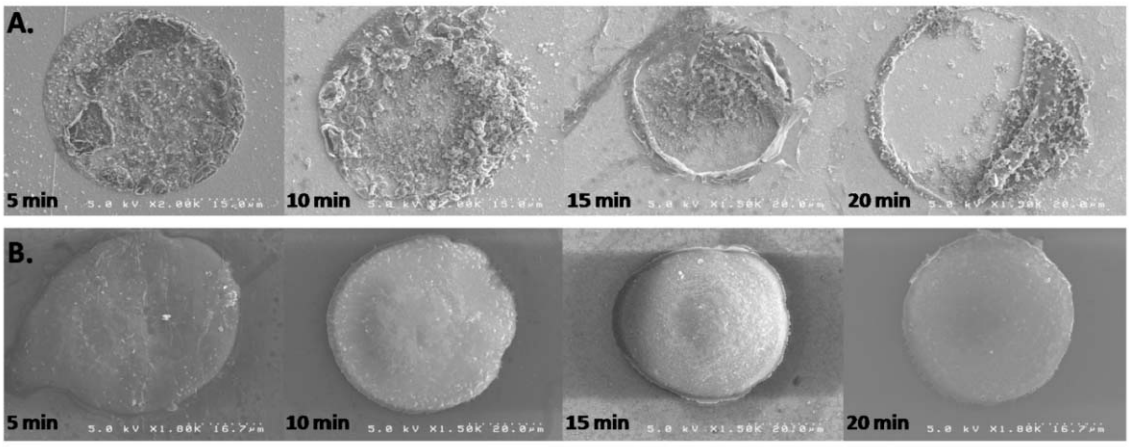

Figure 23. The change in morphology of a printed spot as a function of reaction time with monosilicic acid using Method I. (A) Printed spot reacted first with GO_x (10 min), followed by silica encapsulation. (B) Printed spot in the absence of GO_x as a function of silica formation.

If the theory behind Method I, where the addition of GO_x is responsible for initiating morphological disruption before monosilicic acid is added, then the mere presence of monosilicic acid in the initial reaction solution (Method II) should promote the formation of silica nanoparticles at the spot, rather than in solution. In fact, this is precisely what is observed (Figure 25a). Here, the surface of the spot is still disrupted by the presence of GO_x.

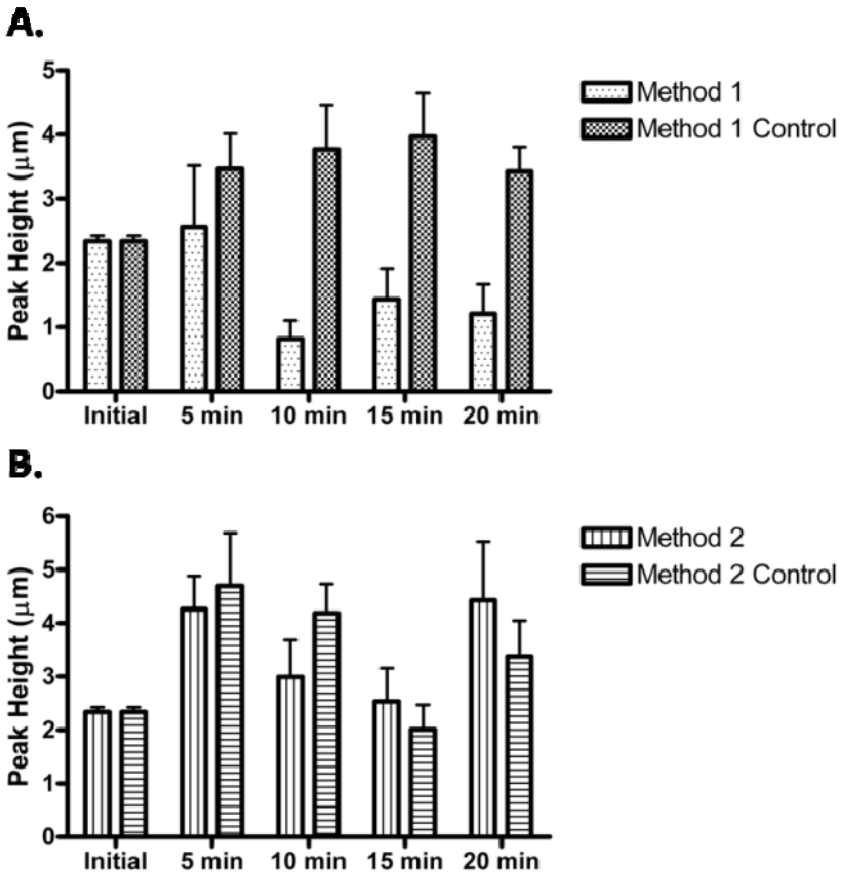

Figure 24. Height profiles of the two methods used in multicomposite formation. (A) Profiles of spot height using Method I with and without GO_x. (B) Profiles of spot height using Method II with and without GO_x. Time points are determined upon addition of monosilicic acid.

Because of the reaction order, however, the dendrimer-GO_x complex is immediately reacted with monosilicic acid, and silica is formed at the spot surface. The spot height initially swells at 5 min (4.3 ± 0.6 μm), much like with Method I. Instead of washing away however, the spot backfills and grows to its highest point at 20 min (4.4 ± 1.1 μm, Figure 24b). Interestingly, the spot height decreases between 5-15 minutes of reaction, as it is being opened (Figure 24b). As a comparison, control patterns were also synthesized under these conditions, again in the absence of enzyme (Figure 25b). Strikingly, the

control patterns behave similarly as those synthesized with GO_x. Profilometry data confirms a similar back-fill behavior as the spot varies in height from 5 min (4.7 ± 1.0 μm), 15 min (2.0 ± 0.5 μm), and 20 min (3.4 ± 0.7 μm, Figure 24b).

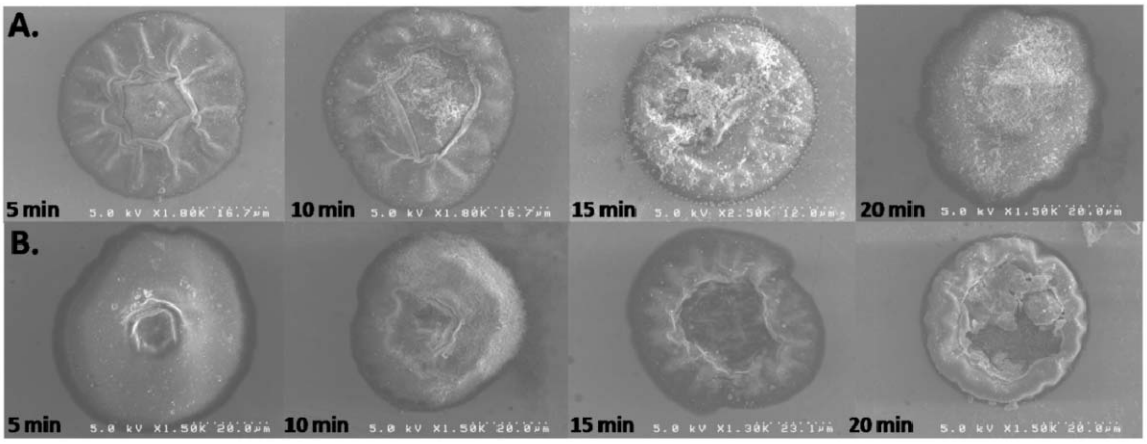

Figure 25. The change in morphology of a printed spot as a function of reaction time with monosilicic acid using Method II. (A) Printed spot reacted with GO_x as a function of silica formation. (B) Printed spot in the absence of GO_x as a function of silica formation.

In order to explain the morphological differences witnessed between the two methods, both the composition of the reaction solution and the ink must be considered. The ink consists of three main components: 113 mM phosphate buffer, 8.6 wt % dendrimer, and 25 wt % PEG. In previous studies, PEG has been shown to be an essential addition to the biomimetic ink, complementing self aggregation and improving overall jettablity.[159] When the jetted patterns are immersed in the reaction solution, the PEG effectively serves as a scaffold to maintain the integrity of the printed spot. During reaction time, the smaller components of the ink, such as the buffer ions and water, are predicted to exchange with the reaction solution until equilibrium is achieved. Since the ink localized in a spot is much more concentrated than the surrounding solution (0.25 mM, pH 7),

water will diffuse into the spot, causing it to swell, as verified by the variation in height profiles determined for control and enzyme reacted spots (Figure 24). The samples from Method I see a much smaller increase in spot height, likely due to the competing mechanism of spot disruption as previously described.

If water diffuses in, the concentrated buffer within the spot is expected to diffuse out into the far more dilute reaction solution. Since high concentrations of buffer (with both anions and cations) are necessary to assist in silica formation of the controls, Method I is predicted to see a significant decrease in silica formation when compared to Method II because the local ionic strength would be much lower. For the samples containing 0.1 mg mL^{-1} GO_x, the enzyme serves as the complementary charge, necessary for the supramolecular aggregation of the dendrimer template. As noted above, the incubation time for Method I allows for the dendrimer and enzyme to interact, disrupting the spot before addition of monosilicic acid, which results in the loss of morphology of the pattern.

In previous studies, the morphology of a printed dendrimer spot was likened to its bio-inspired precursor, the microstructure of a diatom.[159] In these experiments, the formation of a silicified spot was observed in three distinct phases over defined time-points: nucleation, which initiates the phase change on the spot; nanospherical precipitation, which is seen only after the onset of contact pin line effect; and aggregation of the nanoparticles around the exterior of the spot.[159] Interestingly, the change in morphology observed in this study is remarkably different. This is thought to be a direct effect induced by the reduced ionic strength within the reaction solution. Previously, the silica precipitating solution contained a standard buffer concentration that was ~450 x greater

than what is used in this study. Because buffer concentration has an effect on the size and amount of silica formed, lower buffer concentrations induce much smaller particle sized and consequently more uniform spots (Figure 23 and 25) without any distinguishable reaction phases.

Understanding the different effects associated with the two methods of synthesis, Method I was abandoned because of the unfavorable spot morphology associated with the enzyme encapsulated reaction, and Method II was used to probe enzyme activity. In this analysis, 24 mm^2 patterns where printed 2x into a polymer coated 96-well plate. The amount of enzyme included in the reaction mixture was varied to determine the loading capacity and encapsulation efficiency of the spots (Table 1). It was determined that a starting enzyme solution of 0.6 $\mu g\ mL^{-1}$ (200 μL) produced the most robust results. Under these conditions, the overall activity when compared to soluble GO_x was 25 %, which is approximately half of the activity of silica-GO_x composite synthesized in solution previously.[137] Also, it should be noted that the supernatant and subsequent washes yielded minimal activity (~5%), suggesting that most of the enzyme is located within the biocomposite pattern. A loss of activity in this study can most likely be attributed to the restriction of the enzyme onto the 2D surface, which limits access to the substrate more than the 3D nanoparticles. In addition, as the initial enzyme concentration is increased, the encapsulation efficiency drastically lowers, with much of the enzyme is located in the supernatant and subsequent washes. This suggests that the loading capacity of each reaction well for this system is 0.6 $\mu g\ mL^{-1}$, or ~120 ng of total enzyme.

Table 1. The activity of the enzyme as a function of starting enzyme concentration.

Starting Enzyme Concentration (ug/mL)	Reaction Velocity (nmoles/min)	Relative Activity to Soluble GOx (%)
0.6	1.6 ± 0.3	25.9 ± 4.5
3	4.2 ± 0.8	13.4 ± 2.5
6	5.6 ± 0.9	8.9 ± 1.4
12	6.2 ± 1.4	4.9 ± 1.1

To determine how restriction onto a 2D microenvironment affects the functionality of GO_x, kinetic parameters were determined for both the soluble and printed GO_x. When compared to GO_x free in solution, the printed enzyme exhibits a near two-fold decrease in Km (24.47 ± 2.81 for free GO_x and 9.311 ± 1.37 for encapsulated GO_x). Previously, a one-fold decrease in Km was reported for the GO_x-containing silica nanoparticles prepared in solution.[137] In general, a decrease in Km suggests that glucose may have an affinity to the silica, which would create a locally high concentration of substrate near the enzyme. Alternatively, Michaelis-Menten steady state conditions may not be maintained in this system due to the locally high concentration of enzyme within the 2D microenviroment and insufficient diffusion of the substrate to the enzyme. Therefore, the enzyme would be experiencing a lower concentration of substrate than the bulk solution, which would make it turnover slower than expected. It is likely that a combination of factors, including diffusion limitations into the silica framework, as well as enzyme restriction to the surface ultimately result in a decrease in Km and overall activity.

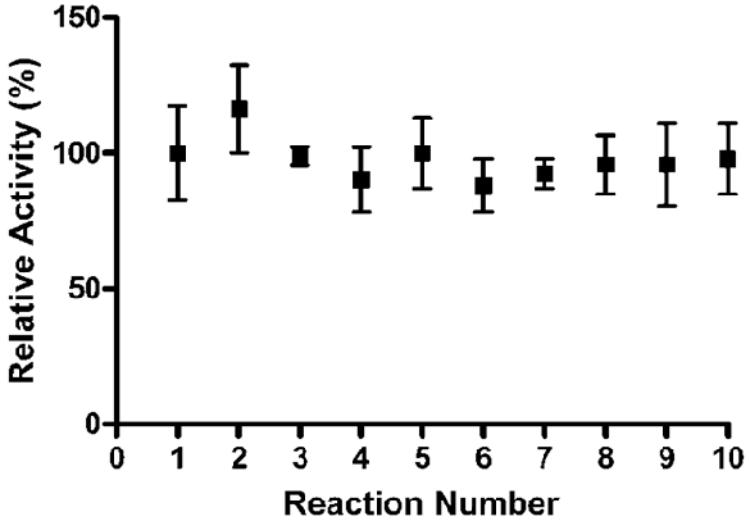

Figure 26. The calculated reusability of the enzyme encapsulated patterns as a function of time. The patterns retained near optimal activity after multiple reactions and washing steps.

To test the applicability of these systems for use as a diagnostic tool, reusability and storage stability of the wells were also assayed to determine whether the enzyme was stable within the printed spot and whether the spot maintained its integrity after multiple uses. After 10 repeated uses, the wells still maintained near optimal activity (Figure 26). This confirms that the spots are not being washed away during the multiple reactions or washing steps. In addition, the wells maintain significant activity even after being stored at 4^{o}C for 12 days (Figure 27). These results show promise in this methodology because it provides a functional biomaterial that can detect small concentrations of substrate, and is also storage stable for extended periods of time without significant loss in activity.

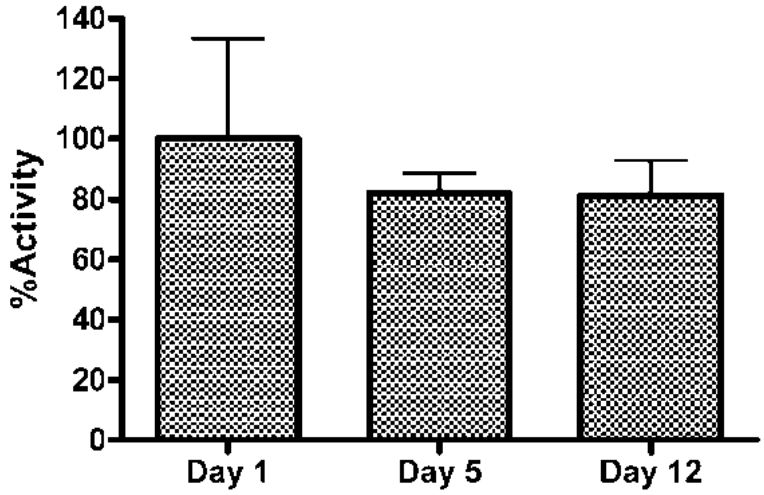

Figure 27. Storage stability of active printed patterns. The patterns were stored at 4°C in 0.1 M phosphate buffer and tested for activity after several days.

Conclusion

In this chapter, the bottom-up synthesis of a GO_x-containing array that maintains significant activity after storage and multiple uses has been presented. As the morphology of the biologically active patterns can vary, as a function of the order in which the reactants are introduced, two methods were investigated. In general, enzyme confinement within the printed pattern reduced the overall reactivity, the reaction rate, and the product yield of the enzyme when compared to solution-phase reactions. Although this may initially appear undesirable, there are several advantages to immobilized biomaterials within active 2D systems, such as minimizing the amount reactants used during a study, reusing the multicomposite templates, and storing the templates until needed. These results suggest that other enzyme systems could be developed to serve a variety of functions, including biosensing and catalysis.

CHAPTER IV

PROGRESS TOWARDS INKJET PRINTED METAL PARTICLE FILMS AS POTENTIAL MEMORY STORAGE DEVICES

Introduction

As a standard in semiconductor devices, Si-based materials have templated a generation of microelectronic devices that are used in almost every aspect of life. From cell phones to MP3 players, the miniaturization of devices has relied on the progress of complementary metal oxide semiconductor (CMOS) technologies, as a function of Moore's Law.[1] Adjusted almost every year for the past 40 years, Moore's Law has predicted that the number of functions per chip will continue to double every 1.5 years until an absolute minimum feature size is reached, eventually exhausting Si-based technologies.[1, 160] In order to circumvent this predicted evolution, new technologies must be investigated, incorporating alternative templates for memory storage.

One such alternative has been directed towards the room temperature synthesis of 2D memory storage devices using functional nanomaterials.[1, 121, 160] Metallic or semiconducting nanocrystals offer an interesting source for technology because their electronic or optoelectronic properties are dependent on the individual core sizes and relative solubility. When an electron is added to small crystals, the response is determined by one of three responses.[161] Quantum confinement may be manifested at discrete energy levels (ΔE). Columb repulsion may occur, increasing the energy cost (E_c) of the system, or the particle may heat up to increase its thermal energy (kT). Only when

ΔE and E_c are less than *kT*, does the nanocrystal exhibit properties similar to the bulk.[161,162]

Semiconducting quantum dots (QDs), for example, are one material, whose properties are dependent on the size of the nanocrystal. If the size is reduced significantly (< 10 nm), the properties of bulk QDs are split into two discrete energy levels, and quantum confinement is observed with two electrons occupying its highest molecular orbital (HOMO).[161 163] Gold monolayer protected clusters (MPCs) have similarly been studied from this aspect. Unlike the QDs, the highest occupied band in the MPC bulk state is unfilled, so electrons have the potential to be excited, yielding an inducible charged state.[161] In the presence of an applied potential, the electrostatic energy (E_c) required to excite the MPC is much greater than its *kT*, enabling discrete electron transfer. This characteristic is known as quantized charging.[161, 162]

At room-temperature, MPCs exhibit a quantized charging effect, where electrons are shuttled into and out of the Au, core once a potential is applied. Because shuttling can be stimulated in the presence of an external stimulus, MPCs have been studied extensively as redox active molecules and have been adapted to a number of electrochemical applications, such as biosensors, solar cells, storage devices, and fuel cells.[26, 160-162, 164-167] In general, these clusters are synthesized in a simple, 2-phase reaction process, where the surface of a zero valent Au is modified, or *protected*, by a monolayer of thiolated ligands. Because of the very nature of their synthesis, the size, shape, and properties of the MPC can be tuned as a function of their capping ligand. For the purposes of our experiments, C6S-Au (hexanethiol-MPCs) will be synthesized and their ability to behave as a viable template for 2D memory storage device will be investigated.

The calculable rate of electron transfer (ET) through chemically assembled MPC films has already shown the great potential of patterning MPCs. [4, 5, 7-11] In fact, Liu and coworkers have calculated the upper limits for electron tunneling through a MPC monolayer using SECM to be ~10^8 s^{-1},[27] and Liljeroth and coworkers have found that compressing an MPC monolayer using LB as a function of ligand size causes different electronic properties of the film. At small interparticles distances along compressed monolayers, C6S-Au particles exhibited higher conductivities than the longer, C12S-Au particles, because electron transport was faster and easier through smaller interparticle distances.[162]

The information obtained from the lateral ET within and along MPC films has demonstrated the capability of a system to be tuned for charge transport. However, one limitation to the aforementioned techniques was that none of the films were spatially resolved. It is understood that the manipulation of a charge localized to a film or a specific area is a critical aspect of device performance.[164] For this reason, we propose the design and development of inkjet printed MPC films as a potential memory storage device. One distinguishing factor of micropatterned surfaces is that a high percentage of molecules are accessible at the surface for reactivity. In a typical printing cycle, one spot has been approximated to be ~10 pL; these pL-volumes correspond to 20-40 μm spots with nano-scale thicknesses on a substrate.[80] Such a thin film allows more components of the ink to be accessible during a reaction. Incorporating this information along with previously established rates of ET along or within MPC films, we will address the room-temperature synthesis of printed MPC films, where ink design, synthesis, and characterization will be studied.

When compared to all other rapid-prototyping instruments, piezoelectric inkjet printing using the DMP enables site-directed deposition of materials with sustainable applications, so that nearly every printed spot printed is interfacial. As previously mentioned, the MPCs used in this experiment are synthesized with hexanethiol capping ligands. During a typical printing cycle, the composite ink that has been developed is loaded into a 10 pL DMP cartridge and printed onto functionalized glass substrates. Once patterned on the substrate, the heterogenous electron transfer at the metal interface will be investigated using SECM.

Established in 1989,[168, 169] scanning electrochemical microscopy (SECM) detects electrical potentials within the diffusion layer of a film.[166, 169] As a non-contact technique, SECM uses the tip of an ultramicroelectrode (UME) as a probe in the presence of a redox mediating solution to scan the surfaces of structures and interfaces with nanoscale resolution. An important advantage of the SECM over all the other electroanalytical techniques is that it uses a piezoelectric, user-controlled inch-worm positioner, so that a scan may have tunable resolution as a function of scan area. During a typical scan, the UME approaches a specified surface, perturbing only the local equilibrium.[170]

As an in situ scanning probe, the SECM rasters the UME tip across an active surface area, while detecting any or all electrochemical gradients. Once the tip is close (< few tip diameters) to a the surface, reversible electron mediators diffuse away from the substrate electrode and are collected at the surface of the tip. A standard SECM instrument uses a four electrode electrochemical cell with a reference electrode (RE), a counter electrode (CE), and two working electrodes (Wes: a conductive substrate and tip (probe)); all of which are controlled by a bipotentiostat (Figure 28). To reduce the noise

associated with the instrument in air, the SECM is mounted onto a vibration-free table inside a Faraday cage.

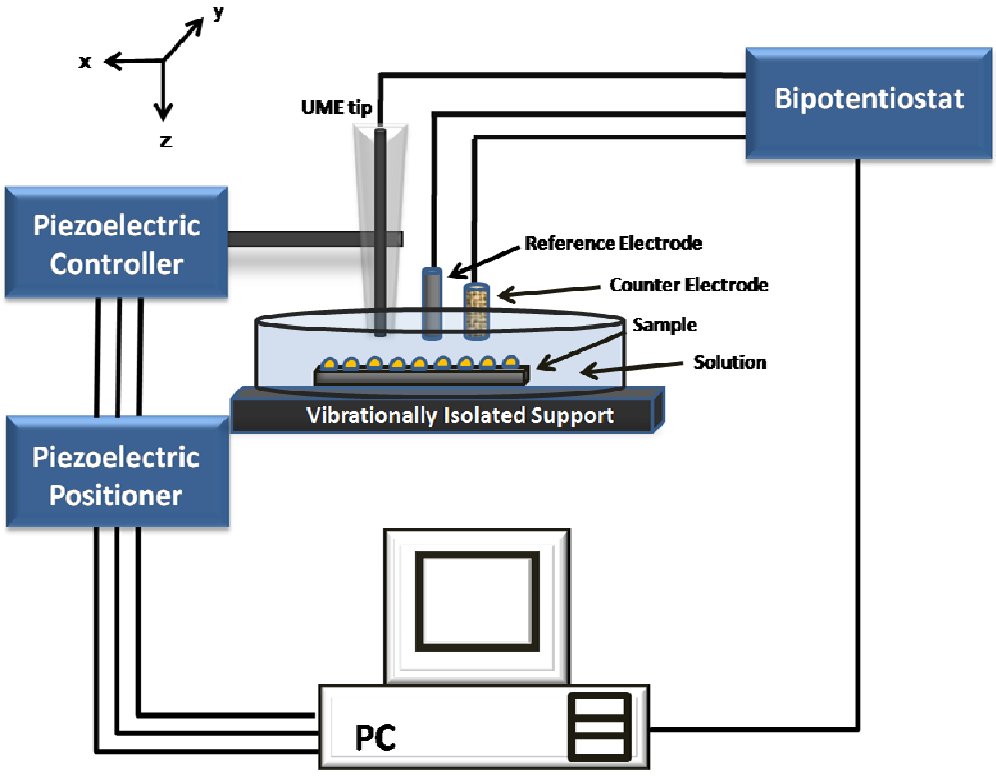

Figure 28. Schematic of SECM.

Experimental

Preparation and Characterization of C6-MPCs

Hexanethiolate-protected gold clusters (C6S-Au) were synthesized according to previously established procedures.[171-174] Briefly, hexanthiol was reduced in auric acid (3:1 molar excess) in the presence of sodium borohydrate at 0°C over 24 h. A series of

isolation and purification steps verified that the clusters were free (NMR) from unbound thiols. was dissolved in DI water and reacted with a tetraoctyl ammoniumbromide (TOABr) and hexanethiol. TOABr was used as a phase transfer reagent for this reaction. The size and polydispersity were quantified using transmission electron microscopy (TEM) and thermal gravimetric analysis (TGA). TEM samples were prepared by dropwise addition of an aqueous suspension of particles onto a carbon coated copper grid (Ted Pell, Inc.). TEM analysis was performed using a Phillips CM20T TEM operating at variable voltages. TGA was performed on an Instrument Specialist TGA-1000. Nuclear magnetic resonance spectroscopy (NMR) samples were prepared by dissolution of the particles in Benzene-*d* and was performed on a 300 MHz Bruker DPX-300 FT-NMR Spectrometer.

Ink

The particles were solubilized in a 50:50 composite solution of toluene and hexane to insure complete wetting of the MPCs. The composite solution was then used to dilute the purified MPCs to a standard concentration of 30 mg mL^{-1}. During every printing cycle, the voltage applied to the printhead nozzles was maintained at 17 V. Cycles varied from 1-4 x printing depending on the application.

Substrates

Substrates were prepared prior to every printing cycle. First, microscope slides were cut into 10-20 cm^2 squares and were cleaned in a solution of piranha (3:1 H_2SO_4: 30% H_2O_2). Once the slides were sufficiently cleaned, they were washed extensively, dried,

and coated with dimethyldichlorosilane (Fluka) for 30 min to create a hydrophobic surface. After silanization, the slides were rinsed in toluene to remove any unreacted silane and air dried. All bright field images were captured using an Axiovert 200 inverted microscope.

Materials

All materials listed in this section were used as supplied unless otherwise specified. Potassium Chloride (KCl, ACS grade) was purchased from Fisher Scientific. Ruthenium (III) hexamine chloride ($Ru(NH_3)_6Cl_3$ or RuHex) was purchased from Acros Organics. Ferrocenylmethyltrimethlammonium hexafluorophosphate (FcTMA PF_6 or FcTMA) was prepared according to literature method.[175] All electrolyte solutions used during imaging were filtered through a syringe-type filter (0.2 μm, Fischer Science) prior to use. All aqueous solutions were prepared using ASTM type I water (18 MΩ cm-1, referred to as DI water) from a solution 2000 (Aqua Solutions, Inc.) reverse osmosis system. The redox couple $FcTMA^{+/2+}$ and $RuHex^{3+/2+}$ were used as aqueous redox mediators in the SECM experiments.

AFM

Tapping mode AFM was used with a Nanoscope II, multimode scanning probe microscope (Digital Instruments). Lateral and vertical resolutions using a 10 nm tip radius were approximately 1-5 nm and 1-2 nm, respectively. For a 60 μm scan, the resolution was 117 nm.

SECM Experiments

The working electrode used in these experiments was a 10 μm platinum (Pt) tip disc-sealed-in-glass ultramicroelectrode (UME) (CH instruments, Inc.). The tips were prepared, so that the final R_G (ratio of the insulating sheath radii (r_g) to the Pt electrode (r_e)) ratio was less than five. To obtain this R_G, all UMEs were polished with 0.05 μm alumina from Beuhler, sonicated in water and ethanol, and imaged using optical micrographs prior to use. After this point, UMEs were electrochemically cleaned for 5 min in 0.5 M H2SO4 using a CHI660a potentiostat.

SECM measurements were conducted on a commercial instrument (CH instruments model 900), controlled by proprietary software. Ru-hex and FeTMA solutions were prepared with a final concentration of 1mM in 0.1M KCl. All imaging was performed in the constant height mode at a 3μm s^{-1} probe speed. All reported potentials were measured against a commercial Ag/AgCl, 3M KCl electrode (RE, model CHI111, CH Instruments) and a Pt mesh counter electrode.

Before every SECM approach curve, a cyclic voltammogram (CV) of the redox mediator was characterized at the UME tip, yielding an expected sigmoidal CV. SECM approach curves were obtained by biasing the tip at the diffusion-limited potential for the oxidation/reduction of the redox mediators (as determined by the CV) and recording the tip current as a function of a distance *l* from the substrate.

All experiments were run in feedback mode, where the tip is immersed in a redox mediating solution, containing oxidizable species, *R*. When a sufficient potential is applied to the tip, the oxidation of R occurs (Eqn 5).

$$R - ne^- \rightarrow O \quad (5)$$

The rate of this reaction is dictated by diffusion of *R* to the UME tip. If the tip is greater than two tip diameters away from the substrate (Figure 29a), the steady state current can be calculated (Eqn 6).

$$i_{T,\infty} = 4nFDca \quad (6)$$

Here, F is the Faraday constant, *n* is the number of transferable electrons in the redox solution (Eqn 2), *D* is the diffusion coefficient for the bulk, *c* is its concentration, and *a* is the tip radius.[166]

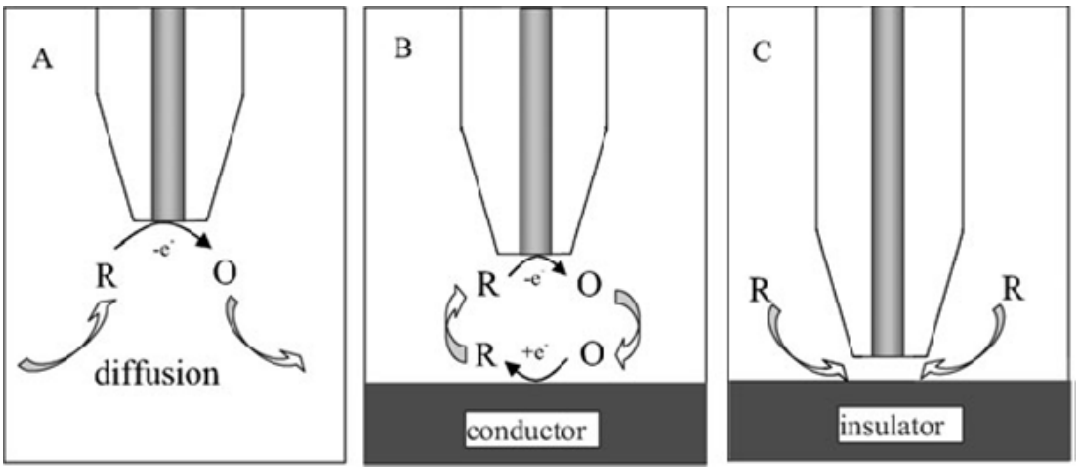

Figure 29. SECM operation in feedback mode. (A) the UME is far from the surface, exhibiting a steady state current, (B) the tip is close to a conducting surface exhibiting positive feedback, and (C) the tip is close to an insulating surface, exhibiting negative feedback.[166]

The magnitude of detectable current at the UME tip is determined by the rate of the regenerated species within the redox solution.[166] For this reason, valuable kinetic data of

the process can be determined by the approach curve (i_T vs d). As the tip approaches the surface of a conducting substrate, the species O (Eqn 5) is formed and diffuses to the substrate where it is regenerated and cycled back into R (Eqn 7).

$$O + ne^- \rightarrow R \tag{7}$$

Because R is being regenerated, this process is known as *positive feedback* (Figure 29b), where the increase in tip current is greater than the steady state current. As the distance (d) between the tip and the substrate decreases, the tip current increases. If the tip approaches an insulating substrate, the generated species, O, does not reach the surface because the insulator inhibits the diffusion of R to the tip. This process is known as *negative feedback* (Figure 29c).

Results and Discussion

C6S-Au synthesis, Characterization, and Printing

Monolayer-protected gold clusters (MPCs) are known to exhibit size-dependent charging.[162] For this reason, once the C6S-Au clusters were synthesized, they were extensively purified and characterized, where the average particle size and the number of coordinated ligands were determined using TEM, TGA, and NMR analysis (Figure 30). While not truly dispersed, cluster analysis does include a considerable portion of a certain size (2.5 ± 0.5 nm), without fractionation. NMR analysis verified that only C6-ligands were bound to the Au surface, and TGA was used to quantify the degree of binding. With

TEM, TGA, and NMR complete, the final composition was determined to be $Au_{397}C6_{117}$ (MW = 91,908 g mol^{-1}).

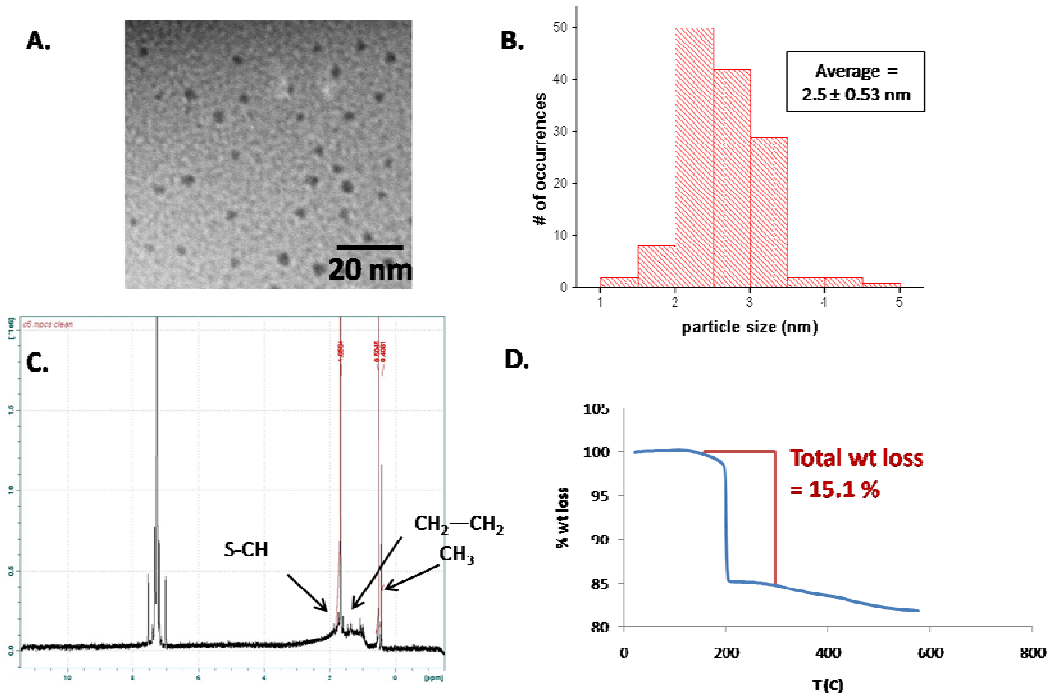

Figure 30. Characterization and analysis of purified C6S-Au clusters. (A) TEM of particles, (B) Distribution of sizes as determined from TEM micrograph, (C) NMR analysis, and (D) TGA.

A calculated weight percent (30 wt %) of particles was then isolated from the stock material and suspended in a composite solution (50:50 Hexane: Toluene) to form an ink that was compatible with the DMP. The ink was loaded into a standard 10 pL cartridge and prepared for printing. Patterns were printed directly onto both silanized glass slides and carbon-coated TEM grids, and their micro/nano-scale properties were characterized (Figure 31b).

Because of the versatility of the DMP, patterns can be tuned according to a specific application. This flexibility is verified through optical microscopy of different patterns (Figure 31a-c). The spot size of the particles on glass was calculated as a function of printing cycle. The average diameters were calculated and varied from 26 ± 3 μm (1x), 29 ± 5 μm (2x), 36 ± 3 μm (3x), and 44 ± 5μm(4x), indicating that the spot size grows as a function of printing cycle. To get a better idea of the nanoscale features within a printed spot, TEM analysis was used. Once printed, the individual MPCs were heterogeneously distributed within the interior and along the exterior of the spot (Figure 31b). Interestingly, this spot heterogeneity included a large percentage of homogenous, nanospherical aggregations that were distributed within the spot interior (Figure 31b, inset). While the nano- and micro-scale features of the printed MPC has provided valuable information regarding the distribution of a printed spot, we were more interested in how these features impact the MPC activity. For this reason, a quantifiable approach was used to investigate the nanoscale activity of a spot.

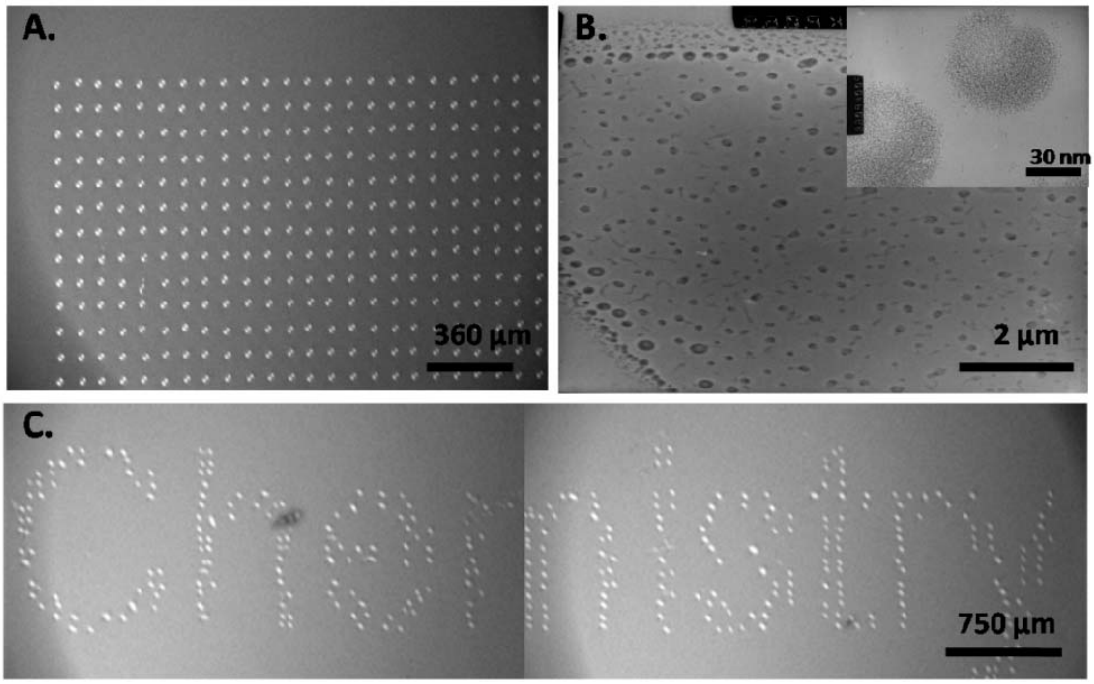

Figure 31. Demonstration of versatility of MPC patterns using DMP. (A) Array of spots printed 1x, spaced 96 µm apart, (B) TEM image of single spot printed on TEM grid, inset is homogeneous nanoparticles distributed within spot interior. (C) Inkjet printed MPCs.

SECM of metal particle films

SECM was used as the ideal analytical instrument for this study because it is a non-invasive and non-destructive method that reports nanoscale output current. As a modified scanning probe, SECM functions according to the faradaic current changes of a scanned surface,[170, 176] yet has never been reported in conjunction with inkjet printed surfaces. For this reason, a series of optimization experiments were necessary before the printed MPCs could be directly analyzed as memory storage devices. Initially, the properties of the patterns were probed as a function of the printing cycle, using a positive redox mediating solution (10 mM FcTMA in 100 mM KCl, Figure 32b).

In the presence of a positive potential (E_{Tip} = +0.65 V), $FcTMA^{2+}$ oxidizes to $FcTMA^{+}$. As the tip approaches the surface of a spot, the local redox solution becomes depleted, and electron transport is initiated. The current generated is then collected at a constant potential and analyzed against multilayer (1-4 x) printing cycles. Using the light microscope coordinated to the SECM, specific spots could be visualized and probed by adjusting the x and y coordinates of the UME. In the preliminary experiments, probe approach curves were too close to the surface, causing the tip to crash and dig straight through the center of the spot (Figure 32c). However undesirable this seemed at the time, the accuracy of tip positioning was verified in these experiments, traveling directly across the center of a spot.

To prevaricate pattern destruction for the remaining experiments, probe approach curves were slowed down (3 μm s^{-1}) for better resolution between the tip and the insulating substrate. When the tip was within 10-20 μm of the surface, a sufficient distance away from the patterns, negative feedback was observed, corresponding to the loss of nearly 70 % of the original current (Figure 32a). At a constant height defined by the probe approach curves, current output associated with the patterns was probed along the x-axis (3.0 μm sec^{-1}, Figure 32d), and the current localized a spot was observed.

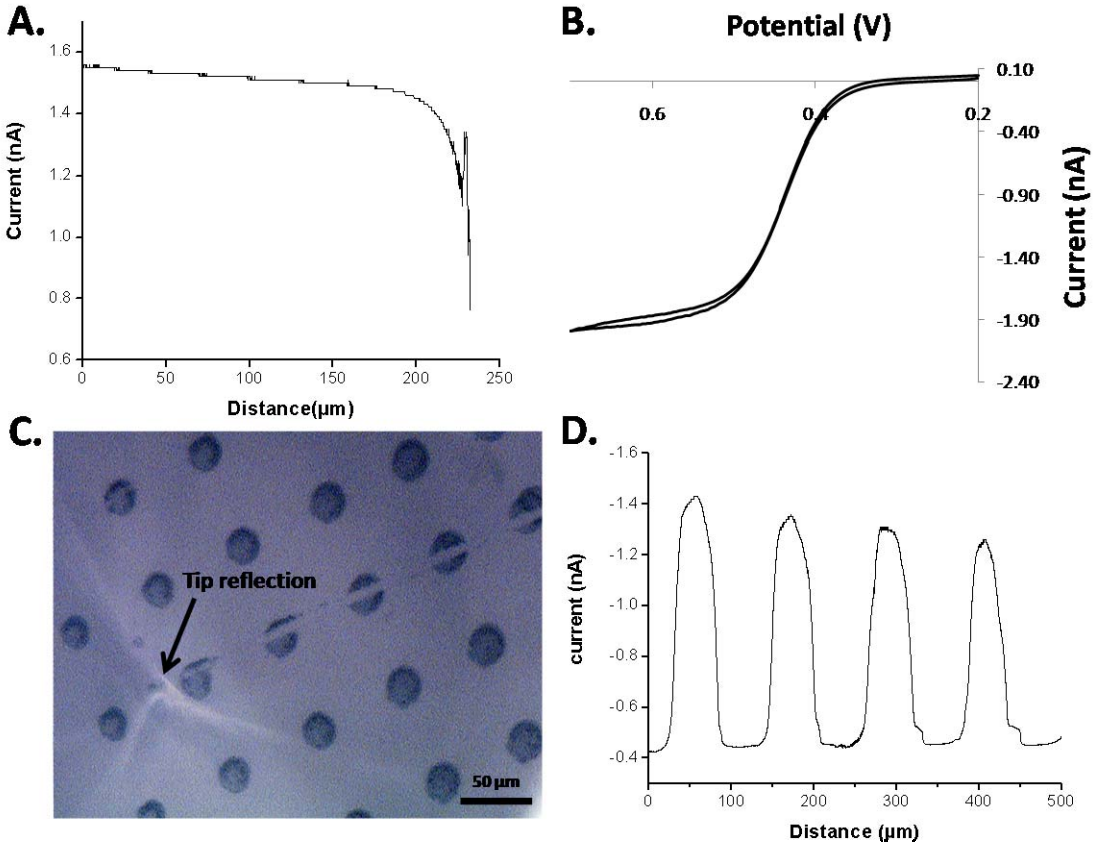

Figure 32. Experimental approach curves of patterns, printed 3x on glass substrate, in FcTMA. (A) Experimental approach curve along the z axis. (B) CV of FcTMA away from the substrate (C) The brightfield image of the UME tip positioned to scan the surface of the printed array. (D) Probe scan curve along the x-axis directly over the array.

As previously mentioned, all of these experiments were run using feedback mode, where both the tip and the substrate were immersed in the FcTMA solution. Because of the nature of SECM, the specificity of the redox process is confined to a thin layer between the tip and the substrate, so that only the positive feedback associated with the conductive spot is observed, and the output current in all scans exhibited a reproducible gaussian distribution over the spots with negligible substrate tilt (Figure 32d).

A map of both the topography and the current uptake was also investigated (Figure 33), where the reduction in current of the oxidized FcTMA (E = +0.65V) was monitored over an array (printed 2x). The appearance of a moderate reduction in current is attributed to the reaction occurring directly at the surface of the spots.

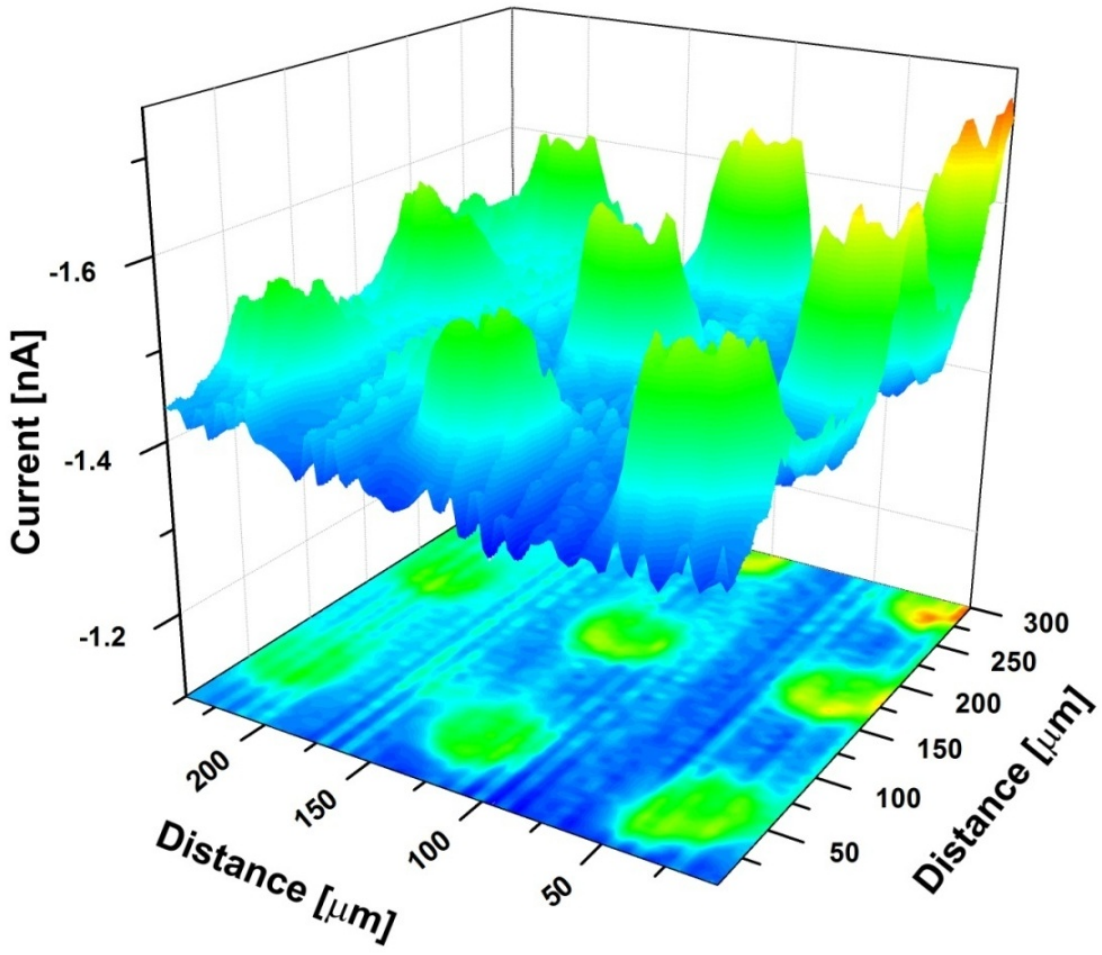

Figure 33. Topographical 3D current profile map (FcTMA, E_{Tip} = +0.65 V) of printed MPC array (patterned 2x).

The difference in current detected between the insulating glass substrate and the inkjet printed spots infers that current is specific to the spots, only. Moreover, SECM profiling has provided valuable information regarding the nanoscale heterogeneity of the spots that is not discernible using TEM, bright field, or AFM analysis. Because the instrument utilizes the fastest possible rate for return of the probe to the y-axis origin after each line scan (the right side of the image), a localized convection in the solution persists for a short time. These appear as pinpoint defects, which disturb the mass transport between the spot and the tip, accounting for fluctuations in current at the surface. In spite of this fluctuation, current uptake was consistent across the array (approximately -0.2 nA), corresponding to the output currents from probe line scans that will be discussed later (Figure 35).

Progress towards memory storage

In its most basic sense, memory storage devices have the capability of injecting or ejecting a charge into a material.[1, 160] To determine the capabilities of our patterns to do so, initial probe line scans were investigated using an alternative, negatively charged redox mediating solution (RuHex). Information of current flow was obtained from the CV curves (Figure 35) and compared against $FcTMA^{2+/+}$ oxidation. In the presence of a negative potential, the reduction of $RuHex^{3+/2+}$ is expected generate a positive charge at the spot surface.

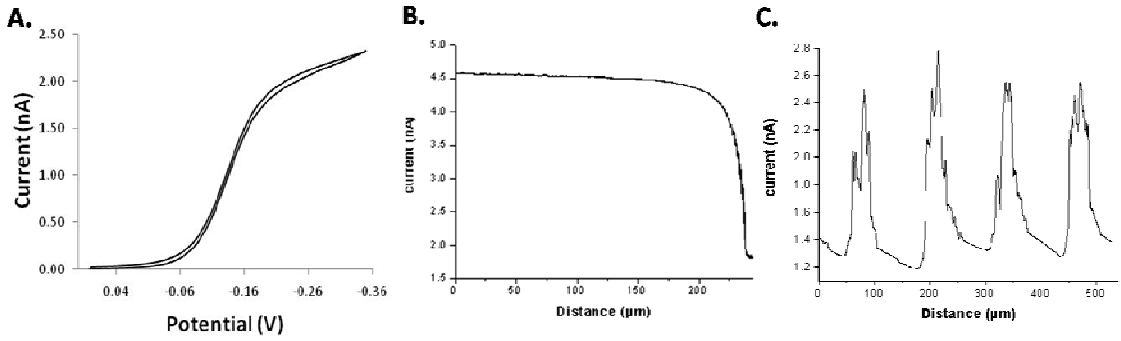

Figure 34. Properties of inkjet printed patterns (patterned 4x) using RuHex mediating solution. (A) CV of RuHex away from substrate, (B) Approach to surface, and (C) Current associated with two printed spots and two satellite spots.

The same printed samples, used in the FcTMA experiments (printed 3x on a surface), were immersed within a RuHex solution. Again, the current generated at the patterns were probed as a function of constant tip height. Initially the tip was immersed in the RuHex mediating solution and submitted to a CV (Figure 34c). During all probe line scans, the potential at the tip was held constant (E_{Tip} = -0.35 V), insuring that the ruthenium complex is reduced at the tip surface. As the tip approached the surface of the insulating glass substrate, negative feedback was detected under this potential (Figure 34b). At this point, the tip was retracted (-10 µm) from the substrate and scanned in the lateral direction generating positive feedback specific to a printed array (Figure 34c).

In its most basic sense, a material capable of memory storage will exhibit two logic levels (*on* or *off*). In the context of our printed arrays, the spots must be capable of storing and maintaining opposite charges.[1] For the purposes of our experiments, a site directed charge has been injected (RuHex) or ejected (FcTMA) into the MPC films. To investigate the flexibility of the patterns to generate variable charges, the current generated at the

spots was collected as a function of the number of printing cycles using both mediating solutions (Figure 35). The absolute values of the output current were shown to increase as a function of multilayer printing; moreover, the current generated using the two mediating solutions were compared and reported to bewithin the same order of magnitude. This additionally infers that the multilayer printing introduces more particles per unit area, thus increasing the overall generated current.

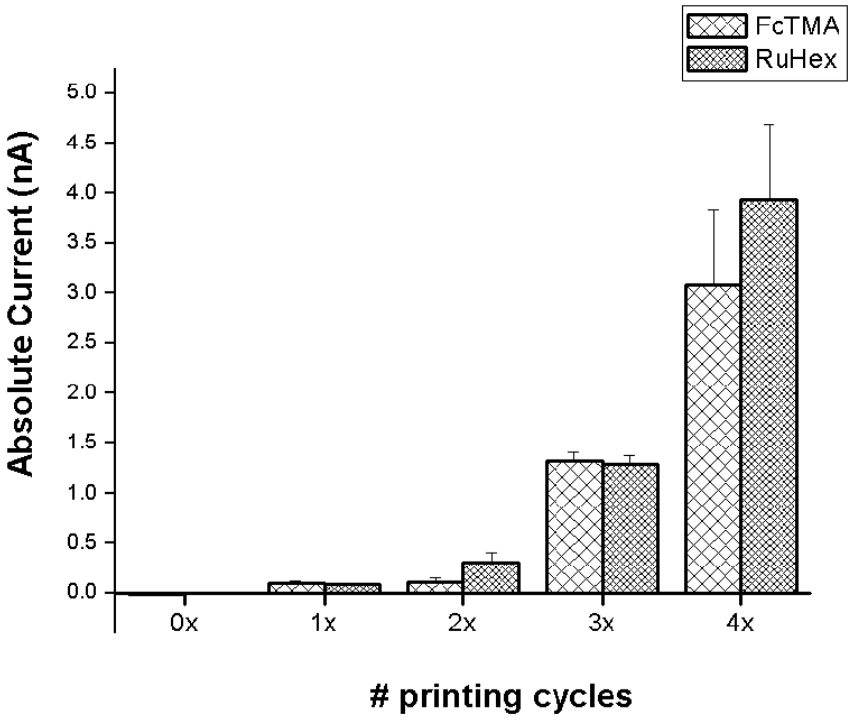

Figure 35. Comparison of absolute values of current generated using two redox mediating solutions.

Assuming that one spot contains approximately 10 pL volume,[80] and that the average C6S-Au cluster within a spot is 2.5 nm, the number of particles can be roughly calculated

as 1.2 x 10^{10} per spot. If a spot is printed 3x, then we may approximate that 3x as many clusters are contained, causing an increase in the overall electroactivity of the surface. To investigate the orientation of a spot with multiple print cycles, the thickness was probed as a function of the number of printing cycles using AFM analysis (Figure 36). These images confirmed that a spot printed 3x (718 nm height, 39 µm width) was in fact taller than a spot printed 1x (319 nm height, 21 µm width) on glass.

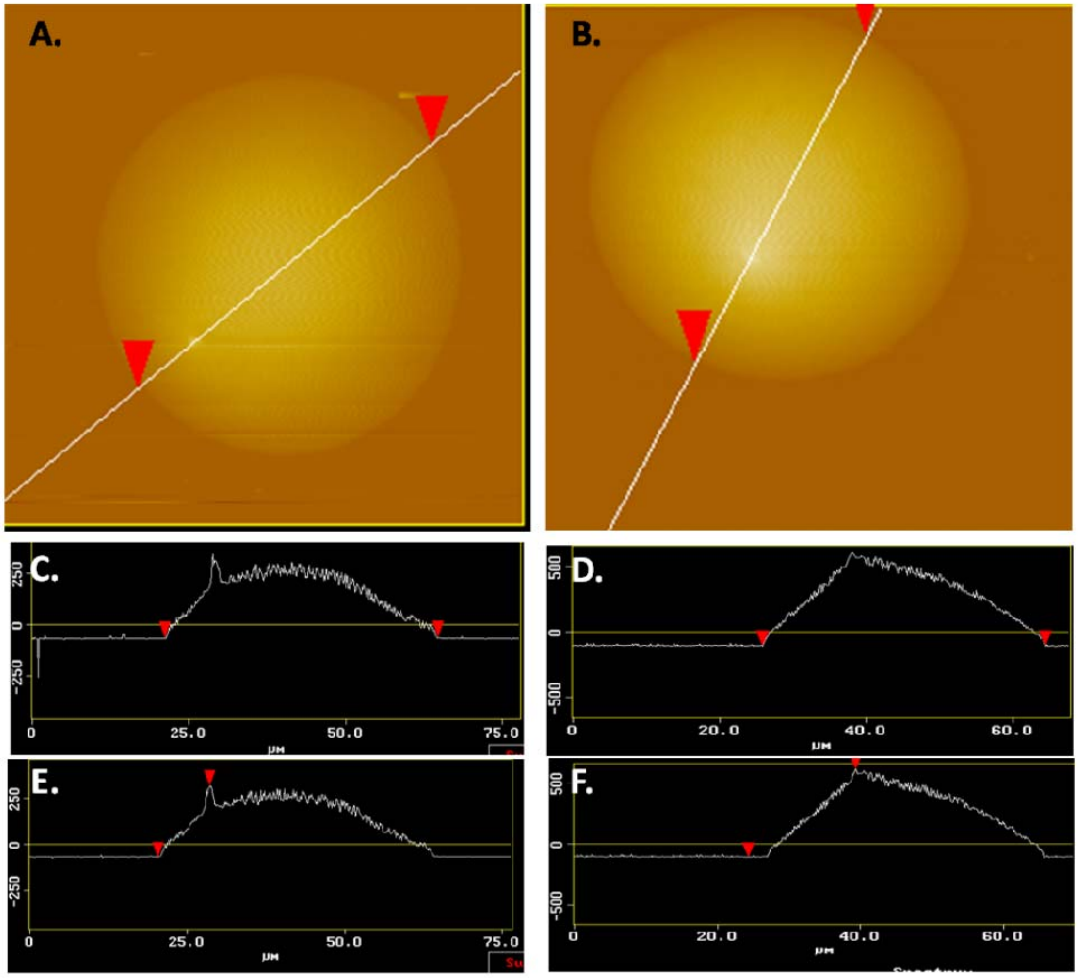

Figure 36. AFM profiling of printed spots. (A, C, E) are the image, width, and height profiles for 1x printed. (B, D, F) are the image, width, and height profiles for 3x printed.

The radii of the two samples were used to calculate relative spot volumes. For a spot printed 1x on a surface, the radius (10.5 μm) was used to determine its experimental volume (Figure 36a). If considered a hemisphere, the calculated spot volume was determined as 2.4 x 10^{-9} cm^3 or 2 pL. For a spot printed 3x on a surface with a 19.5 μm radius, the volume was determined to be 1.5 x 10^{-8} cm^3 or 15 pL. Comparing the two volumes, the spot printed 3x was approximately 6x larger than the volume of a spot printed 1x. Similarly, assuming the spots are hemispherical, the surface area of the two spots was compared. A spot printed 3x (2.4 x 10^3 μm^2) was roughly 3x larger than the spot printed 1x (6.9 x 10^2 μm^2).

To determine whether these experimental values could be compared to the current detected using SECM, the average current of a spot printed 3x (1.29 nA) and 1x (0.082 nA) on a surface was evaluated. These values indicate nearly a 14x difference in current between the multilayered spots. Unfortunately, no direct correlation could be made, comparing the calculated surface area, spot volumes, and the change in current because of the complexities associated with particle spreading along a printed spot. Incorporating the equations for volume and surface area infers that the spot is uniformly distributed along the substrate; however, this is not likely. To investigate the nanoscale distribution of the printed spots, future experiments will be aimed toward quantifying the degree of mass loaded onto a substrate as a function of printing cycle using the modified version of the QCM discussed in Chapter II. It is believed that real-time mass measurements will eliminate the error involved with experimental calculations based off of the AFM data, alone, and with actual mass measurements verified, they can then be directly compared against the average generated currents.

Conclusion

The electrochemical properties of printed MPCs have been investigated using SECM analyses, in constant height mode. While AFM and TEM analysis provided useful information on determining the flexibility and reproducibility of the patterns, they provide only limited analytical information on the overall integrity of the activated spots. With useful preliminary data, we have demonstrated the viability of MPCs as potential memory storage devices, where the patterns were independently shown to successful store opposite charges. Future experiments will be aimed at incorporating a mixed-redox solution, containing both FcTMA and RuHex, to observe the capability of the printed arrays to store and maintain an injected charge.

Synopsis and Future Directions

In the preceeding chapters, piezoelectric inkjet printing using the DMP has been explored for patterning multicomposite biomaterials. From a materials engineering point of view, the research presented here has involved ink development and pattern characterization, where the final aim of every printing cycle was the successful assembly of a functional material. The properties of the printed materials were typically characterized using a number of analytical techniques, including SEM, TEM, ellipsometry, profilometry, SECM, fluorescence microscopy, and UV-vis spectrophotometry.

Initially, experimental aims included quantifying the reproducibility of the DMP using a modified version of the quartz crystal microbalance (QCM). In these experiments, the QCM was customized, from its traditional flow-cell apparatus to a real time nanoscale

balance and was used to quantify the amount of printed material. I found that drop volumes remained constant (< 12 pL/drop), regardless of the composition of the ink. These results were reported in Applied Physics Letters (2007, 91, 113114), placing inkjet printing on the same level as other established deposition techniques such as micro-contact printing or dip-pen nanolithography. After the reproducibility of the DMP was verified, focus then shifted to developing applications for the inkjet printed materials. Among others, a biologically inspired composite dendrimer ink was developed to template the growth of SiO_2 (Small, 2008, 4, 2127) and gold monolayer protected clusters were modified as potential memory storage devices. In addition to the applications presented here, the DMP has also been presented as a viable technique that offers unique approaches for immobilizing biomaterials. These properties not only elucidate unique interfacial interactions inherent in 2D systems, but also aid in developing strategies to disrupt them. Such approaches will lead to discoveries, ranging from new materials to new therapeutic advances for the treatment of disease.

REFERENCES

1. Wolf, S., *Microchip Manufacturing*. Lattice Press: Sunset Beach, 2004.

2. Kumar, U.; Shete, A.; Harle, A. S.; Kasyutich, O.; Schwarzacher, W.; Pundle, A.; Poddar, P., Extracellular Bacterial Synthesis of Protein Functionalized Ferromagnetic Co3O4 Nanocrystals and Imaging of Self-Organization of Bacterial Cells under Stress after Exposure to Metal Ions. *Chemistry of Materials* **2008,** 20, 1484.

3. Weiner, S.; Dove, P. M., *An overview of Biomineralization Processes and the Problem of the Vital Effect*. The Mineralogical Society of America: Washington D.C., 2003; Vol. 54, p 1.

4. Bar-Cohen, Y., Biomimetics--using nature to inspire human innovation. *Bioinspired Biommimcry* **2006,** 1, 1.

5. Carney, C. K.; Harry, S. R.; Sewell, S. L., Detoxification Biominerals. *Topics in Current Chemistry* **2007,** 270, 155.

6. Gorna, K.; Munoz-Espi, R.; Grohn, F.; Wegner, G., Bioinspired mineralization of inorganics from aqueous media controlled by synthetic polymers. *Macromolecular Biosciences* **2007,** 7, 163.

7. Perry, C. C., *Biomaterials*. Wiley-VCH: New York, 1998; p 499.

8. Fratzl, P., Biomimetic materials research: what can we really learn from nature's structural materials. *Journal of the Royal Society Interface* **2007,** 4, 637.

9. Douglas, T.; Young, M., Viruses: Making Friends with Old Foes. *Science* **2006,** 312, 873.

10. Douglas, T.; Young, M., Virus Particles as Templates for Mateials Synthesis. *Advanced Materials* **1999,** 11, 679.

11. Lakshminarayanan, R.; Vivekanandan, S.; Samy, R. P.; Banerjee, Y.; Chi-Jin, E. O.; Teo, K. W.; Jois, S. D. S.; Kini, M.; Valiyaveettil, S., Structure, Self-Assembly, and Dual Role of a B-Defensin-like Peptide from the Chinese Soft-Shell Turtle Eggshell Matrix. *Journal of American Chemical Society* **2008,** 130, 4660.

12. Lee, H.; Dellatore, S. M.; Miller, W. M.; Messersmith, P. B., Mussel-Inspired Surface Chemistry for Multifunctional Coatings. *Science* **2007,** 318, 426.

13. Kroger, N.; Deutzmann, R.; Sumper, M., Polycationic Peptides from Diatom Biosilica That Direct Silica Nanosphere Formation. *Science* **1999,** 286, (5442), 1129.

14. Sumper, M., A Phase Separation for the Nanopatterning of Diatom Biosilica. *Science* **2002,** 295, 2430.

15. Zurcher, S.; Wackerlin, D.; Bethuel, Y.; Malisova, B.; Textor, M.; Tosatti, S.; Gademann, K., Biomimetic surface modifications based on the cyanobacterial iron chelator anachelin. *Journal of American Chemical Society* **2006,** 128, 1064.

16. Henrich, V. E.; Cox, P. A., *TheSurface Science of Metal Oxides*. Cambridge University Press: Boston, 1994.

17. Lang, C.; Schuler, D.; Faivre, D., Synthesis of Magnetite Nanoparticles for Bio- and Nanotechnology: Genetic Engineering and Biomimetics of Bacterial Magnetosomes. *Macromolecular Biosciences* **2007,** 7, 144.

18. Jun, Y.-W.; Seo, J.-W.; Cheon, J., Nanoscaling Laws of Magnetic Nanoparticles and Their Applicabilities in Biomedical Sciences. *Accounts of Chemical Research* **2008,** 41, 170.

19. Lippard, S. J. B., J. M. , *Principles of Bioinorganic Chemistry*. University Science Books: Mill Valley, 1994.

20. Whaley, S. R.; English, D. S.; Hu, E. L.; Barbara, P. F.; Belcher, A. M., Selection of peptides with semiconductor binding specificity for directed nanocrystal assembly. *Nature* **2000,** 405, 665.

21. Nakanishi, H.; Kahn, M., *Peptide Mimetics*. Oxford University Press: New York, 1998; p 395.

22. Brown, S., Metal-recognition by repeating polypeptides. *Nature Biotechnology* **1997,** 15, 269.

23. Chen, W.; Georgiou, G., Cell-Surface Display of Heterologous Proteins: From High-Throughput Screening to Environmental Applications. *Biotechnology and Bioengineering* **2002,** 79, 496.

24. Wittrup, K. D., Protein Engineering by Cell-Surface Display. *Current Opinion in Biotechnology* **2001,** 12, 395.

25. Tomczak, M. M.; Slocik, J. M.; Stone, M. O.; Naik, R. R., Bio-inspired approaches to inorganic material synthesis. *Biochemical Society Transactions* **2007,** 35, 512.

26. Poole, C. P.; Owens, F. J., *Introduction to Nanotechnology*. John Wiley & Sons, Inc.: Hoboken, 2003.

27. Liu, W.-T., Nanoparticles and Their Biological Applications. *Journal of Bioscience and Bioengineering* **2006,** 102, 1.

28. Klem, M. T.; Resnick, D. A.; Gilmore, K.; Young, M.; Idzerda, Y. U.; Douglas, T., Synthetic Control Over Magnetic Moment and Exchange Bias in All-Oxide Materials Encapsulated within a Spherical Protien Cage. *Journal of American Chemical Society* **2007,** 129, 197.

29. Oaki, Y.; Imai, H., The hierarchical architecture of Nacre and its mimetic material. *Angewandte Chemie* **2005,** 117, 6729.

30. Oaki, Y.; Imai, H., Nanoengineering in Echinoderms: The Emergence of Morphology from Nanobricks. *Small* **2006,** 2, 66.

31. Bansal, V.; Poddar, P.; Ahmad, A.; Sastry, M., Room-Temperature Biosynthesis of Ferroelectric Barium Titanate Nanoparticles. *Journal of American Chemical Society* **2006,** 128, 11958.

32. Theil, E. C.; Sayers, D. E.; Brown, M. A., Similarity of the Structure of Ferritin and Iron Dextran (Imferon) Determined by Extended X-ray Absorption Fine Structure Analysis. *The Journal of Biological Chemistry* **1970,** 17, 8132.

33. Klem, M. T.; Mosolf, J.; Young, M.; Douglas, T., Photochemical Mineralization of Europium, Titanium, and Iron Oxyhydroxide Nanoparticles in the Ferritin Protein Cage. *Inorganic Chemistry* **2008,** 47, 2237.

34. Uchida, M.; Klem, M. T.; Allen, M.; Suci, P.; Flenniken, M.; Gillitzer, E.; Varpness, Z.; Liepold, L. O.; Young, M.; Douglas, T., Biological Containers: Protein Cages as Multifunctional Nanoplatforms. *Advanced Materials* **2007,** 19, 1025.

35. Loste, E.; Park, R. J.; Warren, J.; Meldrum, F. C., Precipitation of Calcium Carbonate in Confinement. *Advanced Functional Materials* **2004,** 14, 1211.

36. Lee, S.-Y.; Gao, X.; Matsui, H., Biomimetic and Aggregation-Driven Crystallization Route for Room-Temperature Material Synthesis: Growht of beta-Ga2O3 Nanoparticles on Peptide Assemblies as Nanoreactors. *Journal of American Chemical Society* **2007,** 129, 2954.

37. Nuraje, N.; Su, K.; Haboosheh, A.; Samson, J.; Manning, E. P.; Yang, N.-l.; Matsui, H., Room Temperature Synthesis of Ferroelectric Barium Titanate Nanoparticles Using Peptide Nanorings as Templates. *Advanced Materials* **2006,** 18, 807.

38. Zhang, W.; Zhang, D.; Fan, T.; Ding, J.; Guo, Q.; Ogawa, H., Fabrication of ZnO microtubes with adjustable nanopores on the walls by the templating of butterfly wing scales. *Nanotechnology* **2006,** 17, 840.

39. Biro, L. P.; Balint, Z.; Kertesz, K.; Vertesy, Z.; Mark, G. I.; Tapaszto, L.; Vigneron, J.-P.; Lousse, V.; Biro, L. P., Photonoic Crystal Structures of Biologic Origin: Butterfly Wing Scales. *Materials Research Society Symposium Procedures* **2007,** 1014, AA07.

40. Zhang, W.; Zhang, D.; Fan, T.; Ding, J.; Gu, J.; Guo, Q.; Ogawa, H., Biomimetic zinc oxide replica with structural color using butterfly (Ideopsis similis) wings as templates. *Bioinspired Biommimcry* **2006,** 1, 89.

41. Kröger, N., Prescribing diatom morphology: toward genetic engineering of biological nanomaterials. *Current Opinion in Chemical Biology* **2007,** 11, (6), 662.

42. Aizenberg, J.; Hanson, J.; Koetzle, T. F.; Weiner, S.; Addadi, L., *Journal of American Chemical Society* **1997,** 119, 881.

43. Oaki, Y.; Imai, H., Biomimetic morphological design for manganese oxide and cobalt hydroxide nanoflakes with a mosaic interior. *Journal of Materials Chemistry* **2007,** 17, 316.

44. Yahiro, J.; Oaki, Y.; Imai, H., Biomimetic Synthesis of Wurtzite ZnO Nanowires Possessing a Mosiac Structure. *Small* **2006,** 2, 1183.

45. Gröger, C.; Lutz, K.; Brunner, E., Biomolecular Self-assembly and its Relevance in Silica Biomineralization. *Cell Biochemistry and Biophysics* **2008,** 50, (1), 23.

46. Sumper, M., A Phase Separation Model for the Nanopatterning of Diatom Biosilica. *Science* **2002,** 295, (5564), 2430.

47. Halas, N. J., Nanoscience under Glass: The Versatile Chemistry of Silica Nanostructures. *ACS Nano* **2008,** 2, (2), 179.

48. Noll, F.; Sumper, M.; Hampp, N., Nanostructure of Diatom Silica Surfaces and of Biomimetic Analogues. *Nano Lett.* **2002,** 2, (2), 91.

49. Brunner, E.; Lutz, K., *Handbook of biomineralization: biomimetic and bioinspired chemistry*. Weinheim: Wiley-VCH: 2007; Vol. 2, p 19.

50. Christiansen, S. C.; Hedin, N.; Epping, J. D.; Janicke, M. T.; del Amo, Y.; Demarest, M.; Brzezinski, M.; Chmelka, B. F., Sensitivity considerations in polarization transfer and filtering using dipole-dipole couplings: Implications for

biomineral systems. *Solid State Nuclear Magnetic Resonance* **2006,** 29, (1-3), 170.

51. M. Sumper, E. B., Learning from Diatoms: Nature's Tools for the Production of Nanostructured Silica. *Advanced Functional Materials* **2006,** 16, (1), 17.

52. Poulsen, N.; Kroger, N., Silica Morphogenesis by Alternative Processing of Silaffins in the Diatom Thalassiosira pseudonana. *J. Biol. Chem.* **2004,** 279, (41), 42993.

53. Poulsen, N.; Sumper, M.; Kroger, N., Biosilica formation in diatoms: Characterization of native silaffin-2 and its role in silica morphogenesis. *Proceedings of the National Academy of Sciences* **2003,** 100, (21), 12075.

54. Stephan Wenzl, R. H. P. R. M. S., Silacidins: Highly Acidic Phosphopeptides from Diatom Shells Assist in Silica Precipitation In Vitro. *Angewandte Chemie International Edition* **2008,** 47, (9), 1729.

55. Kroger, N.; Deutzmann, R.; Bergsdorf, C.; Sumper, M., Species-specific polyamines from diatoms control silica morphology. *Proceedings of the National Academy of Sciences* **2000,** 97, (26), 14133.

56. Sumper, M.; Kroger, N., Silica formation in diatoms: the function of long-chain polyamines and silaffins. *Journal of Materials Chemistry* **2004,** 14, (14), 2059.

57. Naik, R. R.; Tomczak, M. M.; Luckarift, H. R.; Spain, J. C.; Stone, M. O., Entrapment of enzymes and nanoparticles using biomimetically synthesized silica. *Chemical Communications* **2004**, (15), 1684.

58. Scott A. Miller, E. D. H. D. W., Rapid and Efficient Enzyme Encapsulation in a Dendrimer Silica Nanocomposite. *Macromolecular Bioscience* **2006,** 6, (10), 839.

59. Pouget, E.; Dujardin, E.; Cavalier, A.; Moreac, A.; Valery, C.; Marchi-Artzner, V.; Weiss, T.; Renault, A.; Paternostre, M.; Artzner, F., Hierarchical architectures by synergy between dynamical template self-assembly and biomineralization. *Nat Mater* **2007,** 6, (6), 434.

60. Wong Po Foo, C.; Patwardhan, S. V.; Belton, D. J.; Kitchel, B.; Anastasiades, D.; Huang, J.; Naik, R. R.; Perry, C. C.; Kaplan, D. L., Novel nanocomposites from spider silk-silica fusion (chimeric) proteins. *Proceedings of the National Academy of Sciences* **2006,** 103, (25), 9428.

61. Zhang, Y.; Wu, H.; Li, J.; Li, L.; Jiang, Y.; Jiang, Y.; Jiang, Z., Protamine-Templated Biomimetic Hybrid Capsules: Efficient and Stable Carrier for Enzyme Encapsulation. *Chem. Mater.* **2008,** 20, (3), 1041.

62. Luckarift, H. R.; Spain, J. C.; Naik, R. R.; Stone, M. O., Enzyme immobilization in a biomimetic silica support. *Nat Biotech* **2004,** 22, (2), 211.

63. Marner, W. D.; Shaikh, A. S.; Muller, S. J.; Keasling, J. D., Morphology of Artificial Silica Matrices Formed via Autosilification of a Silaffin/Protein Polymer Chimera. *Biomacromolecules* **2008,** 9, (1), 1.

64. Knecht, M. R.; Wright, D. W., Amine-Terminated Dendrimers as Biomimetic Templates for Silica Nanosphere Formation. *Langmuir* **2004,** 20, (11), 4728.

65. Knecht, M. R.; Wright, D. W., Dendrimer-Mediated Formation of Multicomponent Nanospheres. *Chem. Mater.* **2004,** 16, (24), 4890.

66. Knecht, M. R.; Sewell, S. L.; Wright, D. W., Size Control of Dendrimer-Templated Silica. *Langmuir* **2005,** 21, (5), 2058.

67. Jan, J. S.; Lee, S.; Carr, C. S.; Shantz, D. F., Biomimetic Synthesis of Inorganic Nanospheres. *Chem. Mater.* **2005,** 17, (17), 4310.

68. J.-S. Jan, D. F. S., Biomimetic Silica Formation: Effect of Block Copolypeptide Chemistry and Solution Conditions on Silica Nanostructure. *Advanced Materials* **2007,** 19, (19), 2951.

69. Christina A. Bauer, D. B. R. Blake A. S., Silica Particle Formation in Confined Environments via Bioinspired Polyamine Catalysis at Near-Neutral pH. *Small* **2007,** 3, (1), 58.

70. C. Zollfrank, H. S. P. G., Regioselectively Ordered Silica Nanotubes by Molecular Templating. *Advanced Materials* **2007,** 19, (7), 984.

71. Cha, J. N.; Stucky, G. D.; Morse, D. E.; Deming, T. J., Biomimetic synthesis of ordered silica structures mediated by block copolypeptides. *Nature* **2000,** 403, (6767), 289.

72. Annenkov, V. V.; Patwardhan, S. V.; Belton, D.; Danilovtseva, E. N.; Perry, C. C., A new stepwise synthesis of a family of propylamines derived from diatom silaffins and their activity in silicification. *Chemical Communications* **2006**, (14), 1521.

73. Belton, D. J.; Patwardhan, S. V.; Annenkov, V. V.; Danilovtseva, E. N.; Perry, C. C., From biosilicification to tailored materials: Optimizing hydrophobic domains and resistance to protonation of polyamines. *Proceedings of the National Academy of Sciences* **2008,** 105, (16), 5963.

74. Chang, J. S.; Kong, Z. L.; Hwang, D. F.; Chang, K. L. B., Chitosan-Catalyzed Aggregation during the Biomimetic Synthesis of Silica Nanoparticles. *Chem. Mater.* **2006,** 18, (3), 702.

75. Lutz, K.; Groger, C.; Sumper, M.; Brunner, E., Biomimetic silica formation: Analysis of the phosphate-induced self-assembly of polyamines. *Physical Chemistry Chemical Physics* **2005,** 7, (14), 2812.

76. Wong, M. S.; Cha, J. N.; Choi, K. S.; Deming, T. J.; Stucky, G. D., Assembly of Nanoparticles into Hollow Spheres Using Block Copolypeptides. *Nano Lett.* **2002,** 2, (6), 583.

77. Coffman, E. A.; Melechko, A. V.; Allison, D. P.; Simpson, M. L.; Doktycz, M. J., Surface Patterning of Silica Nanostructures Using Bio-Inspired Templates and Directed Synthesis. *Langmuir* **2004,** 20, 8431.

78. Xu, M.; Gratson, G. M.; Duoss, E. B.; Shepherd, R. F.; Lewis, J. A., Biomimetic silicification of 3D polyamine-rich scaffolds assembled by direct ink writing. *Soft Matter* **2006,** 2, 205.

79. Kisailus, D.; Truong, Q.; Amemiya, Y.; Weaver, J. C.; Morse, D. E., Self-assembled bifunctional surface mimics an enzymatic and templating protein for synthesis of a metal oxide semiconductor. *PNAS* **2006,** 103, 5652.

80. Deravi, L. F.; Sumerel, J. L.; Gerdon, A. E.; Cliffel, D. E.; Wright, D. W., Output Analysis of Materials Inkjet Printer. *Applied Physics Letters* **2007,** 91, 113114.

81. Mirksich, M.; Whitesides, G. M., Patterning self-assembled monolayers using microcontact printing: a new technology for biosensors? *TIBTECH* **1995,** 13, 228.

82. Synder, P. W.; Johannes, M. S.; Vogen, B. N.; Clark, R. L.; Toone, E. J., Biocatalytic Microcontact Printing. *Journal of Organic Chemistry* **2007,** 72, 7459.

83. Zhao, Y.; J., F., Direct Printing of Self-Assembled Lipid Tubules on Substrates. *Langmuir* **2008,** 24, 5113.

84. Nakanishi, J.; Takarada, T.; Yamaguchi, K.; Maeda, M., Recent Advances in Cell Micropatterning Techniques for Bioanalytical and Biomedical Sciences. *Analytical Sciences* **2008,** 24, 67.

85. Tsuda, Y.; Kikuchi, A.; Yamato, M.; Nakao, A.; Sakurai, Y.; Umezu, M.; Okano, T., *Biomaterials* **2005,** 26, 1885.

86. Yamato, M.; Konno, C.; Utsumi, M.; Kikuchi, A.; Okano, T., *Biomaterials* **2002,** 23, 561.

87. Xia, Y.; Rogers, J. A.; Paul, K. E.; Whitesides, G. M., Unconventional methods for fabricating and patterning nanostructures. *Chemical Reviews* **1999,** 99, 1823.

88. Nelson, C. M.; Raghavan, S.; Tan, J. L.; Chen, C. S., Degradation of micropatterned surfaces by cell dependent and independent process. *Langmuir* **2002,** 19, 1493.

89. Boland, T.; Xu, T.; Damon, B. J.; Cui, X., Application of inkjet printing to tissue engineering *Biotechnology Journal* **2006,** 1, 910.

90. Lewis, J. A.; Gratson, G. M., Direct Writing in Three Dimensions. *Materials Today* **2004,** July/August, 32.

91. Espina, V.; Mehta, A. I.; Winters, M. E.; Calvert, V.; Wulfkuhle, J.; Petricoin III, E. F.; Liotta, L. A., Protein microarrays: Molecular profiling technologies for clincal specimens. *Proteomics* **2003,** 3, 2091.

92. Boland, T.; Tao, X.; Damon, B. J.; Manley, B.; Kesari, P.; Jalota, S.; Bhaduri, S., Drop-on-demand printing of cells and materials for designer tissue constructs. *Materials Science &Engineering C* **2007,** 27, 372.

93. Park, J.-U.; Hardy, M.; Kang, S. J.; Barton, K.; Adair, K.; Mukhopadhay, D. K.; Lee, C. Y.; Strano, M. S.; Alleyne, A. G.; Georgiadis, J. G.; Ferreira, P. M.; Rogers, J. A., High-resolution electrohydrodynamic jet printing. *Nature Materials* **2007,** 6, 782.

94. Mironov, V.; Prestwich, G.; Forgacs, G., Bioprinting Living Structures. *Journal of Materials Chemistry* **2007,** 17, 2054.

95. Sumerel, J.; Lewis, J.; Doraiswamy, A.; Deravi, L. F.; Sewell, S. L.; Gerdon, A. E.; Wright, D. W.; Narayan, R. J., Piezoelectric Ink Jet Processing of Materials for Medical and Biological Applications. *Biotechnology Journal* **2006**.

96. Pudas, M.; Hagberg, J.; Leppavuori, S., Printing parameters and ink components affecting ultra-fine-gravure-offset printing for electronics applications. *Journal of European Ceramic Society* **2004,** 24, 2943.

97. Ye, Y.; Ju, H., *Biosenors and Bioelectronics* **2005,** 21, 735.

98. Coe, S.; Woo, W. K.; Bawendi, M.; Bulovi, V., *Nature* **2002,** 420, 800.

99. Radsak, M. P.; Hilf, N.; Singh-Jasuja, H.; Braedel, S.; Brossart, P.; Rammensee, H.-G.; Schild, H., *Blood* **2003,** 101, (7), 2810.

100. Coleman, J. N.; Khan, K.; Blau, W. J.; Gun'ko, Y. K., *Carbon* **2006,** 44, 1624.

101. Ryu, B.-H.; Choi, Y.; Park, H.-S.; Byun, J.-H.; Kong, K.; Lee, J.-O.; Chang, H., Synthesis of highly concentrated silver nanosol and its application to inkjet printing. *Colloids Surfaces A: Physicochem. Eng.* **2005,** 270-271, 345.

102. Dong, H.; Carr, W. W., An experimental study of drop-on-demand drop formation. *Phys. Fluids* **2006,** 18.

103. Sirringhoaus, H., High-resolution inkjet printing of all-polymer transistor circuits. *Science* **2000,** 290, 2123.

104. Calvert, P., Inkjet printing for materials and devices. *Chemical Materials* **2001,** 13, 3299.

105. Haber, C.; Boillat, M.; van der Schoot, B., Precise nanoliter fluid handling system with integrated high-speed flow sensor. *Assay Drug Development Technology* **205,** 3, 203.

106. Song, J. H.; Nur, H. M., Defects and prevention in ceramic components fabricated by inkjet printing. *Mater. Proc. Technol.* **2004,** 155, 1286.

107. Xu, T., Inkjet printing of viable mammalian cells. *Biomaterials* **2005,** 26, 93.

108. Dutronc, P.; Carbonne, B.; Menil, F.; Lucat, C., Influence of the nature of the screen-printed electrode metal on the transport and detection properties of thick-film semiconductor gas. *Sensors and Actuators B* **1992,** 8, 279.

109. Brunahl, J.; Grishij, Piezoelectric shear mode drop-on-demand inkjet actuator. *Sensors and Actuators A* **2002,** 101, 371.

110. Reis, N.; Ainsley, C.; Derby, B., Ink-Jet Delivery of particle suspensions by piezoelectric droplet ejectors. *Journal of Applied Physics* **2005,** 97.

111. Teng, K. F.; Vest, R. W., Metallization of solar cells with inkjet printing and silver metallo-organic inks. *IEEE Trans. Compon. Hyb. Manuf. Tech.* **1988,** 11, 291.

112. Kim, D.; Jeong, S.; Kyun, B.; Moon, J., *Applied Physics Letters* **2006,** 89, 264101.

113. Karabasheva, S.; Balushev, S., *Applied Physics Letters* **2006,** 89, 31110.

114. Tekin, E.; Gans, B.-J.; Schubert, U. S., Ink-Jet printing of polymers- from single dots to thin film libraries. *Journal Materials Chemistry* **2004,** 14, 2627.

115. Reiss, N.; Ainsley, C.; Derby, B., Ink-Jet Delivery of particle suspensions by piezoelectric droplet ejectors. *Journal of Applied Physics* **2005,** 97.

116. Mei, J.; Lovell, M. R.; Mickle, M. H., Formulation and processing of novel conductive solution inks in continuous inkjet printing of 3-D electric circuits. *IEEE Trans. Electron. Packag. Manuf.* **2005,** 28, 265.

117. Janshoff, A.; Galla, H.-J.; Steinem, C., Piezoelectric Mass-Sensing Devices as Biosensors-An Alternative to Optical Biosensors? *Angewandte Chemie* **2000,** 39, (4004- 4032).

118. O'Sullivan, C. K.; Guilbault, G. G., Commercial quartz crystal microbalances-theory and applications. *Biosens. Bioelectron.* **1999,** 14, 663.

119. Gerdon, A. E.; Wright, D. W.; Cliffel, D. W., *Anal. Chem.* **2005,** 77, 304.

120. Hillier, A. C.; Ward, M. D., *Anal. Chem.* **1992,** 64, 2539.

121. Hornyak, G. L.; Dutta, J.; Tibbals, H. F.; Roa, A. K., *Introduction to Nanoscience*. Taylor & Fracis Group: Boca Raton, 2008; Vol. 1

122. Sperling, L. H., *Introduction to Physical Polymer Science*. 4th ed.; John Wiley & Sons Inc.: Hoboken, 2006.

123. Sawhney, A. In *Piezoresistive sensors on textiles by inkjet printing and electroless plating*, Materials Research Symposium Proceedings, San Francisco, 2006; San Francisco, 2006; pp 4.

124. Kroger, N.; Deutzmann, R.; Bergsdorf, C.; Sumper, M., *Proceedings of the National Academy of Sciences U.S.A.* **2000,** 97, 14133.

125. Kroger, N.; Deutzmann, R.; Sumper, M., *Science* **1999,** 286, 1129.

126. Butler, R. T.; Ferrell, N. J.; Hansford, D. J., *Applied Surface Science* **2006,** 252, 7337.

127. Patwardhan, S. V.; Mukherjee, N.; Steinitz-Kannan, M.; Clarson, S. J., Bioinspired synthesis of new silica structures. *Chemical Communication* **2003**, 1122.

128. Vazquez-Olmos, A.; Redon, R.; Rodriguez-Gattorno, G.; Mata-Zamora, M. E.; Morales-Leal, F.; Fernandez-Osrio, A. L.; Saniger, J. M., *Journal of Colloid Interface Science* **2005,** 291, 175.

129. Yuan, J.-J.; Jin, R.-H., *Advanced Materials* **2005,** 2005, 885.

130. Xu, M.; Gratson, G. M.; Duoss, E. B.; Shepherd, R. F.; Lewis, J. A., *Soft Matter* **2006,** 2, 205.

131. Lee, S.; Lee, B.; Kim, B. J.; Park, J.; Yoo, M.; Bae, W. K.; Char, K.; Hawker, C. J.; Bang, J.; Cho, J., Free-standing nanocomposite multilayers wit various length scales, adjustable internal structures, and functionalities. *Journal of American Chemical Society* **2009,** 131, 2579.

132. Hasenbank, M. S.; Edwards, T.; Fu, E.; Garzon, R.; Kosar, F.; Look, M.; Mashadi-Hossein, A.; Yager, P., Demonstration of multi-analyte patterning using piezoelectric inkjet printing of multiple layers. *Analytica Chimica Acta* **2008,** 611, 80.

133. Sanders, W.; Vargas, R., Characterization of carboxylic acid-terminated self assemble monolayers by electrochemical impedance spectroscopy and scanning electrochemical microscopy. *Langmuir* **2008,** 24, 6133.

134. Berne, C.; Betancor, L.; Luckarift, H. R.; Spain, J. C., Application of a microfluidic reactor for screening cancer prodrug activation using silica-immobilized nitrobenzene nitroreducase. *Biomacromolecules* **2006,** 7, 2631.

135. Crowe-Willoughby, J. A.; Genzer, J., Formation and properties of responsive siloxane-based polymeric surfaces with tunable surface reconstruction kinetics. *Advanced Functional Materials* **2009,** 19, 460.

136. Laurent, N.; Haddoub, R.; Flitsch, S. L., Enzyme catalysis on solid surfaces. *Trends in Biotechnology* **2008,** 26, 328.

137. Miller, S. A.; Hong, E. A.; Wright, D. W., Rapid and efficient enzyme encapsulation in a dendrimer silica nanocomposite. *Macromolecular Bioscience* **2006,** 6, 839.

138. Martin, G. L.; Minteer, S. D.; Cooney, M. J., Spatial distribution of malate dehydrogenase in chitosan scaffolds. *ACS Materials and Interfaces* **2009,** 1, 367.

139. Betancor, L.; Luckarift, H. R., Bioinspired enzyme encapsulation for biocatalysis. *Trends in Biotechnology* **2008,** 26, 566.

140. Luckarift, H. R., Silica-immobilized enzyme reactors. *Journal of Liquid Chromatography & Related Technologies* **2008,** 21, 1568.

141. He, P.; Greenway, G.; Haswell, S. J., The on-line synthesis of enzyme functionalized silica nanoparticles in a microfluidic reactor using polyethylenimine polymer and R5 peptide. *Nanotechnology* **2008,** 19, 315603.

142. Luckarift, H. R.; Johnson, G. R.; Spain, J. C., Silica-immobilized enzyme reactors; application to cholinesterase-inhibition studies. *Journal of Chromatography B* **2006,** 843, 310.

143. Dunker, A. K.; Fernandez, A., Engineering productive enzyme confinement. *Trends in Biotechnology* **2007,** 25, 189.

144. Kunzelmann, U.; Bottcher, H., Biosensor properties of glucose oxidase immobilized within SiO2 gels. *Sensors and Actuators B* **1997,** 38-39, 222.

145. Kroger, N.; Lorenz, S.; Brunner, E.; Sumper, M., *Science* **2002,** 298, 584.

146. Iller, R. K., *The Chemistry of Silica*. Wiley: New York, 1979.

147. Knecht, M. R.; Wright, D. W., *Langmuir* **2004,** 20, 4728.
148. Knecht, M. R.; Wright, D. W., *Chemistry of Materials* **2004,** 16, 4890.

149. Miller, S. A.; Hong, E. D.; Wright, D. W., *Macromolecular Biosciences* **2006,** 6, 839.

150. Visak, Z. P.; Canongia Lopez, J. N.; Rebelo, L. P., *Monatshefte fur Chemie* **2007,** 138, 1153.

151. Arrington, D.; Curry, M.; Street, S. C., *Langmuir* **2002,** 18, 7788.

152. Brousseau, L. C. I.; Aurentz, D. J.; Benesi, A. J.; Mallouk, T. E., *Anaytical Chemistry* **1997,** 69, 688.

153. Knecht, M. R.; Wright, D. W., *Chemical Communications* **2003,** 24, 3038.

154. Blanchette, F.; Bigioni, T. P., *Nature Physics* **2006,** 2, 254.

155. Shimizu, K.; Del Amo, Y.; Brezinski, M. A.; Stucky, G. D.; Morse, D. E., *Chemistry and Biology* **2001,** 8, 1051.

156. Sharma, A.; Mittal, J.; Verma, R., Instability and Dewetting of Thin Film Induced by Density Variations. *Langmuir* **2002,** 18, 10213.

157. Wang, C.; Krausch, G.; Geoghegan, M., *Langmuir* **2001,** 17, 6269.

158. Deegan, R. D.; Bakajin, O.; Dupont, T. F.; Huber, G.; Nagel, S. R.; Witten, T. A., *Nature* **1997,** 389, 827.

159. Deravi, L. F.; Sumerel, J. L.; Sewell, S. L.; Wright, D. W., Piezoelectric inkjet printing of biomimetic inks for reactive surfaces. *Small* **2008**.

160. Paul, S.; Pearson, C.; Molloy, A.; Cousins, M. A.; Green, M.; Kolliopoulou, S.; Dimitrakis, P.; Normand, P.; Tsoukalas, D.; Petty, M. C., Langmuir-blodgett film deposition of metallic nanoparticles and their application to electronic memory structures. *Nano Letters* **2003,** 3, 533.

161. Laaksonen, T.; Ruiz, V.; Liljeroth, P.; Quinn, B. M., Quantised charging of monolayer-protected nanoparticles. *Chemical Society Reviews* **2008,** 37, 1836.

162. Liljeroth, P.; Vanmaekelbergh, D.; Ruiz, V.; Kontturi, K.; Jiang, H.; Kauppinen, E.; Quinn, B. M., Electron transport in two-dimensional arrays of gold nanocrystals investigated by scanning electrochemical microscopy. *Journal of American Chemical Society* **2004,** 126, 7126.

163. Kouwenhoven, L. P.; Austing, D. G.; Tarucha, S., *Rep. Prog. Phys.* **2001,** 64, 701.

164. Laaksonen, T.; Ruiz, V.; Murtomaki, L.; Quinn, B. M., Nanoparticle film charging --ion rectified or ion limited? *Journal of American Chemical Society* **2007,** 129, 7732.

165. Pietron, J. J.; Hicks, J. F.; Murray, R. W., Using electrons stored on quantitized capacitors in electron transfer reactions. *Journal of American Chemical Society* **1999,** 121, 5565.

166. Sun, P.; Laforge, F. O.; Mirkin, M. V., Scanning electrochemical microscopy in the 21st century. *Physical Chemistry Chemical Physics* **2007,** 9, 802.

167. Ahonen, P.; Ruiz, V.; Kontturi, K.; Liljeroth, P.; Quinn, B. M., Electrochemical gating in scanning electrochemical microscopy. *J. Phys. Chem. C* **2008,** 112, 2724.

168. Bard, A. J.; Denuault, G.; Friesner, R. A.; Dornblaser, B. C.; Tuckerman, L. S., *Analytical Chemistry* **1991,** 63, 1282.

169. Bard, A. J.; Fan, F. R.; Pierce, D. T.; Unwin, P. R.; Wipf, D. O.; Zhou, F., *Science* **1991,** 254, 68.

170. Bard, A. J., *Introduction and Principles*. Marcel Dekker, Inc.: New York, 2001.

171. Hicks, J. F.; Miles, D. T.; Murray, R. W., *Journal of American Chemical Society* **2002,** 124, 13322.

172. Hicks, J. F.; Templeton, A. C.; Chen, C. S.; Sharan, K. M.; Jasti, R.; Murray, R. W.; Debord, J.; Schaaff, T. G.; Whetten, R. L., *Analytical Chemistry* **1999,** 71, 3703.

173. Brust, M.; Fink, J.; Bethell, D.; Schriffin, D. J.; Kiely, C., Synthesis and reactions of functionalized gold nanoparticles. *Journal of the Chemical Society, Chemical Communications* **1995,** 16, 1655.

174. Brust, M.; Walker, M.; Bethell, D.; Schriffin, D. J.; Whyman, R., *Chemical Communications* **1994,** 801.

175. Forouzan, F.; Bard, A. J.; Mirkin, M. V., *Israeli Journal of Chemistry* **1997,** 37, 155.

176. Lu, X.; Wang, Q.; Liu, X., Review: recent applications of scanning electrochemical microscopy to the study of charge transfer kinetics. *Analytica Chimica Acta* **2007,** 601, 10.

CURRICULUM VITAE

Research Interest

For decades, researchers have been searching for alternative methods to ameliorate the rate of waste production and the cost of spending commonly associated with nanofabrication facilities across the world. Estimated to reach an outstanding $100 billion per facility by the year 2020, the mounting cost associated with supporting technicians and maintaining instrumentation, alone, has motivated researchers to develop alternative approaches, utilizing less expensive, water soluble biological materials, or *biomaterials*, for new types of devices. From manual stamping to computer-based printing, the availability of current materials deposition techniques has offered unique approaches for immobilizing biomaterials that not only elucidate unique interfacial interactions inherent in 2D systems, but also aid in developing strategies to disrupt them. Such approaches will lead to the development of a range novel, sustainable materials with applications ranging from memory storage to therapeutic devices.

Education

August 2005-Present	**Vanderbilt University** **Nashville, TN** Advanced to Candidacy August 2007 Expected graduation June 2009
August 2001- May 2005	**University of Alabama** **Tuscaloosa, AL** Bachelor of Science in Chemistry Minor, English

Research Experience

Graduate Research Assistant	August 2005-Present	Vanderbilt University
Undergraduate Research Assistant under Professor R. Kumar Pandey, Electrical Engineering.	September 2004-July 2005	University of Alabama
Undergraduate Research Fellow under Robert Metzger, Chemistry.	June 2003-August 2004	University of Alabama

Fellowships and Awards

NSF funded Travel Grant, 5th Annual Scanning Electrochemical Microscopy Conference	2008
Selection of "Output Analysis of Materials Inkjet Printer" as feature article in the *Nanowerk* Spotlight Section	2007
Selection of "Output Analysis of Materials Inkjet Printer" into the American Institute of Physics and the American Physical Society's addition of the Virtual Journal of Nanoscience and Technology	2007
Recipient NSF grant for Undergraduate Research Summer Program (UA)	2004
Dean's List (UA)	2001-2005
June Noland Crowder Scholarship Recipient in Chemistry	2001

Professional Societies and Activities

American Chemical Society (member) 2008-current
Materials Research Society (member) 2005-current

Teaching

Vanderbilt University

- Private Tutoring, General Chemistry Fall 07-Present
- General Chemistry Lab (Chem102a/b) Fall 05-Fall 06.

Selected Service Activities

Vanderbilt University

- Chair Graduate Chemistry Steering Committee (2007-2008).
- Member of Vanderbilt Institute of Nanoscale Science and Engineering (2006-Present).

Publications

1. Leila F. Deravi, David W. Wright, Jan L. Sumerel, "Printing Bioinks with Technologically Relevant Applications," The Chemistry of Inkjet Inks, Ed. Shlomo Magdassi: World Scientific Inc. 2009, *in press*.

2. Leila F. Deravi, Joshua D. Swartz, David W. Wright, "The Biomimetic Synthesis of Metal Oxide Nanomaterials," Nanomaterials for the Life Sciences: Vol 2. Ed. Challa Kumar: Wiley-VCH Verlag GmbH & Co. KgaA, **2009**, *in press.*

3. Leila F. Deravi; Jan L. Sumerel; Sarah L. Sewell; David W. Wright. "Piezoelectric Inkjet Printing of Biomimetic Inks for Reactive Surfaces" *Small* **2008**, DOI: 10.1002/smll.200800536.

4. Leila F. Deravi, Joshua D. Swartz, Jan L. Sumerel, David W. Wright, "Piezoelectric Inkjet Printing of Biomimetic Surfaces for Enzyme Encapsulation," *NIP24 and Digital Fabrication Proceedings* **2008**, 504-507.

5. Leila F. Deravi; Jan L. Sumerel; Aren E. Gerdon; David E. Cliffel; David W. Wright. "Output analysis of materials ink-jet printer." *Appl. Phys. Letts*. **2007**, 91(11), 113114/1-113114/3.

6. Jan L. Sumerel, John Staton, Leila F. Deravi, David W. Wright, "Displays are Here to Stay: Method Development for High Throughput Process Manufacturing Methods Employing R&D Scale Ink Jet Printing,"*NIP24 and Digital Fabrication Proceedings* **2007**, 435-439.

7. J. L. Sumerel; J. Lewis; A. Doraiswamy; L. F. Deravi; S.L. Sewell; A.E. Gerdon; D. W. Wright and R. J. Narayan. "Piezoelektrisher Druck medizinischer und biologischer Mataerialien." *BioSpekrtum* **2006**, 7, 756-757.

8. J. L. Sumerel; J. Lewis; A. Doraiswamy; L. F. Deravi; S. L. Sewell; A. E. Gerdon; D. W. Wright and R. J. Narayan. "Piezoelectric Ink Jet Processing of Materials for Medical and Biological Applications." *Biotechnology* **2006**. 1(9), 976-87.

Below is the publication which stemmed from work associated with my undergraduate research.

1. R. K. Pandey, P. Padmini, L.F. Deravi, N.N. Patil, J. Zhong, J. Dou, L. Navarrate, R. Schad, M. Shamsuzzoha, "Magnetic-Semiconductors in Fe-Ti-Oxide Series and Their Potential Applications,"

International Conference on Solid State and Integrated Circuit Technology Proceedings (ICSICT) **2006**, 2, 992-997

Invited Seminars

1. "Piezoelectric Inkjet Printing of Biomimetic Surfaces for Enzyme Encapsulation," The Society for Imaging Science and Technology's (IS&T) 24th International Conference on Digital Printing Technologies in Pittsburg, PA. September 6-11, 2008.
2. 5th Annual Scanning Electrochemical Microscopy Conference in Blue Mountain Lake, NY, August 24-28, 2008.

Presentations

1. "Probing the Surface Reactivity of Printed Metal Particle Films using Scanning Electrochemical Microscopy," 60th Southeastern Regional Meeting of the American Chemical Society in Nashville, TN, November 12-16, 2008.
2. "Printing Diatoms," Science and Technology Institute (NSTI) Conference, Boston, MA, June 2-5, 2008.
3. "Piezoelectric Inkjet Printing of Biomaterial Templates," Poster session, Materials Research Society Meeting, San Francisco, CA, April 10-13, 2007.